

Development of coherent mid-infrared source using chalcogenide photonic crystal fibers

Thèse N° 9352

Présentée le 21 février 2019

**à la Faculté des sciences et techniques de l'ingénieur
Laboratoire de systèmes photoniques
Programme doctoral en photonique**

pour l'obtention du grade de Docteur ès Sciences

par

Sida XING

Acceptée sur proposition du jury

**Prof. L. Thévenaz, président du jury
Prof. C. S. Brès, directrice de thèse
Dr T. Sylvestre, rapporteur
Prof. C. Finot, rapporteur
Prof. C. Moser, rapporteur**

2019

Acknowledgements

To start, I would like to express my deepest gratitude to my PhD supervisor, Professor Camille-Sophie Brès. Since I joined the lab in March 2015, she always put full trust in my project and give me great freedom to experiment with different ideas.

I would also like to thank my colleagues who helped me through my PhD project. I really enjoyed and benefited a lot from the discussions and collaborations with my great colleagues: Dr. Amin Shoaie, Dr. Armand Vedadi, Mr. Jianqi Hu, Dr. Svyatoslav Kharitonov, Mr. Tianyi Liu, and Dr. Thibault North (in alphabet order). Out of our own lab, I would also like to thank my friendly and knowledgeable colleagues from Fiber Optics lab. Beyond EPFL, my special thanks go to my former colleagues in McGill University, Dr. Lizhu Li and Dr. Nurmamet Abdukerim, for all the experiment advices during my project.

In addition, I really enjoyed my 2 months collaboration in Ultrafast optics lab at Tianjin University. The experience in building mode locked fiber laser, handling of free space optics and construction of an auto-correlator will be a great asset in my future career. I would like to thank Prof. Minglie Hu, Prof. Youjian Song and Prof. Bowen Liu for teaching me all the experiment and theoretical knowledge.

I want to express my thanks to the jury committee, Prof. Christophe Finot, Prof. Christophe Moser, Prof. Luc Thévenaz, and Prof. Thibaut Sylvestre, for reviewing my paper and improving its quality.

Finally, I thank my father to teach me how true scientist works. I thank my mother for teaching me the skills in daily life. All my achievements could not be possible without their continuous and unconditional support.

Abstract

Many molecule bonds have vibration frequencies in the mid-infrared band. Thus, this band is of great interest to molecular spectroscopy, material processing and medical applications. However, many optical materials typically used for laser sources experience high losses due to the presence of such vibration bonds making the design of mid-infrared coherent sources challenging. Such task is even more difficult when considering designing all-fiber sources which offer additional compactness and robustness. The goal of this project is to address such challenge by designing all-fiber mid-infrared sources based on chalcogenide fibers and nonlinear effects. Using degenerated parametric conversion of a 2 μm pump and a telecom band signal laser, one can generate an idler in the mid-infrared band.

As a first step, the linear and nonlinear performances of several chalcogenide fibers were compared. The results prove the chalcogenide photonic crystal fiber design to be the ideal platform for this project as it offers high nonlinearity and low loss. Numerical simulations provide further improvement of photonic crystal geometry. Our improved designs allow for an extreme shaping of the dispersion to optimize the four-wave-mixing process within the thulium /holmium fiber laser band.

In the meantime, several cavity configurations were tested to boost the thulium/holmium laser performance, that are required for pumping of our chalcogenide fibers. Polarizer-free cavity designs result more compact laser footprint, which moreover enables a higher slope efficiency. Such lasers enable precise measurements of sample fiber optical parameters.

The combined efforts on fiber and laser optimization leads to efficient continuous-wave parametric conversion. Thanks to the excellent mid-infrared transmittance of chalcogenide glass, this high efficiency can be extended to longer pumps in mid-infrared. However, fiber fuse, a result of heat dissipative solitons, is the main constrain for reaching better conversion efficiency.

For ultrafast applications, a sub-cm length chalcogenide photonic crystal fiber generates flat-top, linearly chirped supercontinuum in the normal dispersion region. This pulse length could be compressed to two optical cycles by linear compression. Once again, the experimental results match perfectly with the simulations.

Overall, we show in this thesis that chalcogenide PCFs are promising for highly efficient and low threshold nonlinear optics in the middle infrared, offering new options for light generation in this critical wavelength band

Résumé

e nombreuses liaisons moléculaires ont des fréquences de vibration dans la bande infrarouge moyenne. Cette bande présente donc un grand intérêt pour la spectroscopie moléculaire, le traitement de matériaux et les applications médicales. Cependant, de nombreux matériaux optiques généralement utilisés pour les sources laser subissent des pertes élevées dues à la présence de telles liaisons de vibration, ce qui complique la conception de sources cohérentes dans l'infrarouge moyen. Une telle tâche est encore plus difficile lorsque l'on envisage de concevoir des sources toutes fibres qui offrent une compacité et une robustesse supplémentaires. Ce projet a pour objectif de relever ce défi en concevant des sources infrarouges moyennes entièrement en fibres, basées sur des fibres de chalcogénure et des effets non linéaires. En utilisant la conversion paramétrique dégénérée d'une pompe de $2\text{ }\mu\text{m}$ et d'un laser de signal de bande télécom, il est possible de générer un oisif dans la bande infrarouge moyenne.

Dans un premier temps, les performances linéaires et non linéaires de plusieurs fibres de chalcogénure ont été comparées. Les résultats démontrent que la conception de la fibre à cristaux photoniques de chalcogénure est la plate-forme idéale pour ce projet, car elle offre une grande non-linéarité et de faibles pertes. Les simulations numériques améliorent encore la géométrie des cristaux photoniques. Nos conceptions améliorées permettent une mise en forme extrême de la dispersion afin d'optimiser le processus de mélange à quatre ondes dans la bande laser à fibres de thulium / holmium.

Dans l'intervalle, plusieurs configurations de cavités ont été testées pour améliorer les performances du laser thulium / holmium, nécessaires au pompage de nos fibres de chalcogénure. La conception des cavités sans polariseur produit une empreinte laser plus compacte, ce qui permet en outre une plus grande efficacité de la pente. De tels lasers permettent des mesures précises des paramètres de fibre optique de l'échantillon. Les efforts conjugués d'optimisation de la fibre et du laser conduisent à une conversion paramétrique efficace en onde continue. Grâce à l'excellent facteur de transmission dans l'infrarouge moyen du verre de chalcogénure, ce rendement élevé peut être étendu à des pompes plus longues dans l'infrarouge moyen. Cependant, la fusion des fibres, résultat des solitons dissipant la chaleur, est la principale contrainte pour atteindre un meilleur rendement de conversion.

Pour les applications ultra-rapides, une fibre à cristaux photoniques à base de chalcogénure d'un centimètre de long génère un supercontinuum à sommet plat et chirpé linéairement dans la zone de dispersion normale. Cette durée d'impulsion pourrait être comprimée à deux cycles optiques par compression linéaire. Une fois encore, les résultats expérimentaux correspondent parfaitement aux simulations.

Globalement, nous montrons dans cette thèse que les PCF de chalcogénure sont

prometteurs pour une optique non linéaire très efficace et à seuil bas dans l'infrarouge moyen, offrant de nouvelles options pour la génération de lumière dans cette bande de longueur d'onde critique.

Keyword: chalcogenide fibers, microstructured fibers, photonic crystal fibers, fiber laser, nonlinear fiber optics, supercontinuum generation, four-wave-mixing, mid-infrared, nonlinear Schrodinger equation, fiber fuse

Table of Contents

Acknowledgements.....	i
Abstract.....	ii
Résumé.....	iii
List of Acronyms.....	viii
Chapter 1 Introduction	1
1.1 Thesis motivation	1
1.1.1 Applications of MIR photonics.....	1
1.1.2 Coherent MIR light source	3
1.2 Main contributions	7
1.3 Thesis structure	9
Chapter 2 Light propagation in an optical fiber.....	11
2.1 Introduction	11
2.2 Linear propagation in optical fibers	12
2.2.1 Propagation loss of ChG optical fiber	12
2.2.2 Chromatic dispersion.....	14
2.3 Nonlinear propagation in optical fibers.....	16
2.3.1 Definition of parameters	16
2.3.2 CW four wave mixing	17
2.3.3 Nonlinear propagation of a pulse in fibers	21
Conclusion.....	24
Chapter 3 Fiber lasers at 2 μm	25
3.1 Introduction	25
3.2 Experimental setup for FWM.....	26
3.3 Basics of Tm^{3+} and Ho^{3+} -doped fiber laser	27
3.4 Tm-doped fiber lasers.....	28
3.4.1 Pump lasers.....	29
3.4.2 Signal laser	32
3.5 Ho-doped fiber lasers	36
3.5.1 Background of 2.1 μm fiber lasers	36

3.5.2 Linear cavity design for 2.1 μm fiber laser	38
Conclusion.....	45
Chapter 4 Selection of fiber material and geometry	46
4.1 Introduction	46
4.2 Material selection	49
4.2.1 Comparison of MIR fiber material options	49
4.2.2 Selection of ChG glasses	51
4.3 Geometry and preparation of ChG fiber facet.....	53
4.3.1 ChG fiber geometries.....	53
4.3.2 ChG facet preparation for coupling	55
4.4 Experimental results.....	57
4.4.1 AsSe Photonic crystal fibers	57
4.4.2 AsS Suspended core fibers	60
4.5 Design of tapered GeAsSe PCF	64
Conclusion.....	66
Chapter 5 Amplified parametric conversion	67
5.1 Introduction	67
5.2 Experimental setup and fiber parameters	68
5.2.1 Fiber geometry and fabrication.....	68
5.2.2 Experimental setup	70
5.3 T-PCF characterization at low and medium power	72
5.3.1 FWM characterization of T-PCFs at low pump power.....	73
5.3.2 Impact of transition un-tapered fiber	77
5.3.3 Temperature dependence	78
5.3.4 Summary of the test results	79
5.4 Amplified parametric conversion	81
5.4.1 Impact of laser linewidth	81
5.4.1 Experimental results	82
5.4.2 Data analysis.....	85
5.4.3 Repeatability.....	88
5.4.4. Summery of all test results	90
Conclusion.....	90

Chapter 6 Fiber fuse in chalcogenide Photonic crystal fibers.....	91
6.1 Introduction	91
6.2 Observation of fiber fuse.....	93
6.3 Impact beyond fiber fused region.....	98
Conclusion.....	99
Chapter 7 Linearly chirped supercontinuum generation.....	100
7.1 Introduction	100
7.2 Experimental setup and fiber parameters	102
7.3 Results and analysis	105
7.3.1 Preliminary tests at 2070nm with cm-long PCFs	105
7.3.2 Study of SCG stability and environment sensitivity	107
7.3.3 SCG evolution and pulse properties	109
7.4 Potential improvements.....	113
7.4.1 Simulation of linear pulse compression.....	113
7.4.2 Reaching for octave spanning.....	114
7.4.3 Impact of pump pulse duration.....	115
Conclusion.....	116
Chapter 8 Conclusion and further developments.....	118
List of References	120

List of figures

Figure 1.1. The absorption of multiple molecules in MIR..	1
Figure 1.2. Atmosphere transmission as a function of wavelength	2
Figure 2.1. Facet geometry of two microstructured fiber geometry	13
Figure 2.2. Linear loss of $\text{As}_{40}\text{S}_{60}$ and $\text{Ge}_{10}\text{As}_{22}\text{Se}_{68}$ microstructured fibers after fabrication	13
Figure 2.3. Material dispersion of As_2S_3 , As_2Se_3 and $\text{Ge}_{11.5}\text{As}_{24}\text{Se}_{61.5}$ chalcogenide glasses	15
Figure 2.4 Schematic of FWM process.	17
Figure 2.5. Comparison of Gaussian and sech^2 pulses	23
Figure 3. 1. A generalized setup for this project	26
Figure 3.2. The energy level transitions for multiple rare earth ions	27
Figure 3.3. The emission and absorption cross-sections of Tm^{3+} (a) and Ho^{3+} (b).	28
Figure 3.4. Pump laser configurations utilizing backward (a) and forward (b) ASE	29
Figure 3.5. The slope efficiency and laser linewidth of multiple pump wavelengths	30
Figure 3.6. The 1950 nm pump laser cavity and output properties	32
Figure 3.7. Signal laser cavity and ASE for various active fiber lengths	33
Figure 3.8. The wavelength dependent response of free space grating and fiber loop mirror	34
Figure 3.9. Cavity configuration for the new signal laser.	35
Figure 3.10. The OSA spectrum of improved signal laser using 25 m of Tm-doped fiber	36
Figure 3.11. The reflection of PM-FBG and laser cavity design	38
Figure 3.12 Laser property of the 2100 nm pump laser.	39
Figure 3.13 Test setup for FLM operation at 2100 nm	40
Figure 3.14. The tunable reflection from FLM at 2100 nm	40
Figure 3.15 Experimental setup of the laser cavity and characterization setup	41
Figure 3.16 ASE spectrum recorded with multiple configurations.	41
Figure 3.17. OSA record of the laser line spectrum and ASE suppression.	42
Figure 3.18. The 2100.9 nm output power with respect to 1950nm pump laser	43
Figure 3.19. The laser line stability over time for all three operation categories	44
Figure 3.20. The laser stability when operating in single wavelength mode and dual wavelength mode	45
Figure 4.1. An overview of various MIR fibers.	47
Figure 4.2. Transmission of a 0.1 mm thick CYTOP in the MIR band	53
Figure 4.3. Comparison of facets from different cleaving methods.	56
Figure 4.4. Dispersion parameter as a function of the wavelength.	58

Figure 4.5. Superimposed FWM spectra of different signal laser positions with constant pump power	58
Figure 4.6. FWM results with the AsSe PCF	59
Figure 4.7. AsS SCF geometry and light leakage	60
Figure 4.8. FWM result with the AsS SCF	61
Figure 4.9. Dispersion parameter as a function of the wavelength.....	62
Figure 4.10. Experimental points superimposed to theoretical fits of the CE as a function of the idler wavelength for pump wavelength	63
Figure 4.11. The dispersion of designed fiber and tested fibers	65
Figure 4.12 The simulated CE plot with two pump wavelengths at normal and anomalous region	65
Figure 5.1 Dispersion engineered GeAsSe tapered PCF	68
Figure 5.2 Experimental setup for GeAsSe T-PCF characterization	70
Figure 5.3 Dispersion simulation for different hole-period ratios	72
Figure 5.4. FWM spectrum together with theoretical fitting	73
Figure 5.5. Spectrum indicating birefringence of T-PCF1	74
Figure 5.6. Retrieved CE data and simulation on the fast (blueish color) and slow (reddish color) axes.....	75
Figure 5.7. The retrieved dispersion from T-PCF1 and simulations at several wavelengths.....	76
Figure 5.8. The retrieved dispersion with 2.1 μm pump from T-PCF5	77
Figure 5.9. The retrieved data from T-PCF4 using 1950 nm pump laser	78
Figure 5.10. Test of fiber dispersion at different temperature.....	79
Figure 5.11. The summarized data from various T-PCFs	80
Figure 5.12. Broadening of pump laser linewidth due to strong nonlinearity of T-PCF	82
Figure 5.13. The amplification of laser ASE at various pump power.....	83
Figure 5.14. The ON/OFF signal amplification recorded on OSA.....	83
Figure 5.15. The retrieved data points with 125 mW coupled pump power.....	84
Figure 5.16. Parametric amplification of T-PCF4 with various signal laser positions	85
Figure 5.17. The simulation and experimental position of first dip.....	86
Figure 5.18. Low pump power characterizations before and after sending 125 mW of coupled power into T-PCF4	87
Figure 5.19. The CE and coupled pump power result in a slope of 2 linear fitting in log scale	87
Figure 5.20. The relation between signal gain (Gs) and idler CE.....	88
Figure 5.21. The spectrum recorded on OSA for T-PCF1	88
Figure 5.22. The CE normalized to fiber length for T-PCF1, 3 and 4	89
Figure 6.1. FWM power evolution before the onset of fiber fuse	93
Figure 6.2. The top-view of T-PCF3 input after fiber fuse	94
Figure 6.3. Optical images of damaged PCF facets.....	95

Figure 6.4. SEM images of T-PCF3 at various locations.....	96
Figure 6.5. The setup for “opening” T-PCF3 and the images from fused region	97
Figure 6.6. Top-view of the input side from T-PCF4.....	97
Figure 6.7. FWM characterization of the leftover part from T-PCF4.....	99
Figure 7.1. The experimental setup and pump laser spectrum	102
Figure 7.2. PCF facet and dispersion	104
Figure 7.3. SCG at different peak powers for FUT 1 (solid line), and the corresponding simulations (dashed line)	105
Figure 7.4. The experiment recorded SCG spectrum with simulations under multiple approximations.....	106
Figure 7.5. SCG at different peak powers for FUT2 (solid line), and the corresponding simulations (dashed line)	107
Figure 7.6. Superimposed SCG spectrum for FUT2.....	108
Figure 7.7. Simulated pulse evolution in wavelength (a) and time domain (b), at 2kW peak power.....	109
Figure 7.8. Experimental and simulated results of ANDi SCG at different power levels for FUT3.	110
Figure 7.9. ANDi SCG coherence and 3 dB bandwidth evolution	110
Figure 7.10. SCG at different pump powers for FUT4, FUT5 and FUT6	111
Figure 7.11. The simulated chirp properties of the ANDi SCG pulse	112
Figure 7.12. Simulation of compressed output power	113
Figure 7.13. Simulation of dispersion and SCG of designed taper PCF.....	114
Figure 7.14. Simulation of ANDi SCG using 200fs pump pulse.....	116

List of Acronyms

ANDi – All-normal dispersion

ASE – Amplified spontaneous emission

ChG – Chalcogenide glass

CE – Conversion efficiency

CW – Continuous-wave

CYTOP – Cyclized Transparent Optical Polymer

DCS – Dual-comb spectroscopy

DFWM – Degenerated four wave mixing

DM – Dichroic mirror

DOP – Degree of polarization

EDFA – Erbium-doped fiber amplifier

FBG – Fiber Bragg grating

FLM – Fiber loop mirror

FOM – Figure of merit

FWHM – Full width half maximum

FUT – Fiber under test

FEL – free electron laser

FWM – Four wave mixing

GNLSE – Generalized nonlinear Schrodinger equation

HR – Higher reflection

KDP - Deuterated potassium dihydrogen phosphate (KD_2PO_4)

GVD – Group velocity dispersion

LIDAR - Light detection and ranging

LR – Low reflection

MI – Modulation instability

MIR – Mid-infrared
OBW – Optical wave breaking
OPO – Optical parametric oscillator
OSA – Optical spectrum analyzer
PBS – Polarization beam splitter
PCF – Photonic crystal fiber
PC – Polarization controller
PD - Photodetector
PM – Polarization maintaining
PMMA – Polymethyl methacrylate
PPLN – Periodically poled lithium niobate
QCL – Quantum cascade laser
SCF – Suspended-core fiber
SCG – Supercontinuum generation
SP – Selective photothermolysis
SPM – Self-phase modulation
TDFA – Thulium-doped fiber amplifier
TPA – Two photon absorption
T-PCF – Tapered photonic crystal fiber
WDM – Wavelength division multiplexer
XPM – Cross-phase modulation
ZBLAN - $\text{ZrF}_4\text{-BaF}_2\text{-LaF}_3\text{-AlF}_3\text{-NaF}$
ZDW – Zero dispersion wavelength

Chapter 1

Introduction

1.1 Thesis motivation

1.1.1 Applications of MIR photonics

Most molecule bonds have vibration frequencies in the mid-infrared (MIR) band. Thus, this band is of great interest to molecular spectroscopy [1-4], food industry [5] and medical applications [6-8]. The research and development of MIR components is a highly active research area. In the MIR band, the wavelength range of 2 to 20 μm is typically referred as the “molecular fingerprint region”. This term comes from the fact that many molecular bonds have fundamental vibration frequency lying in this window. As shown in Fig. 1.1, the vibration frequencies of greenhouse gas, toxic chemicals and explosives lie in this wavelength range.

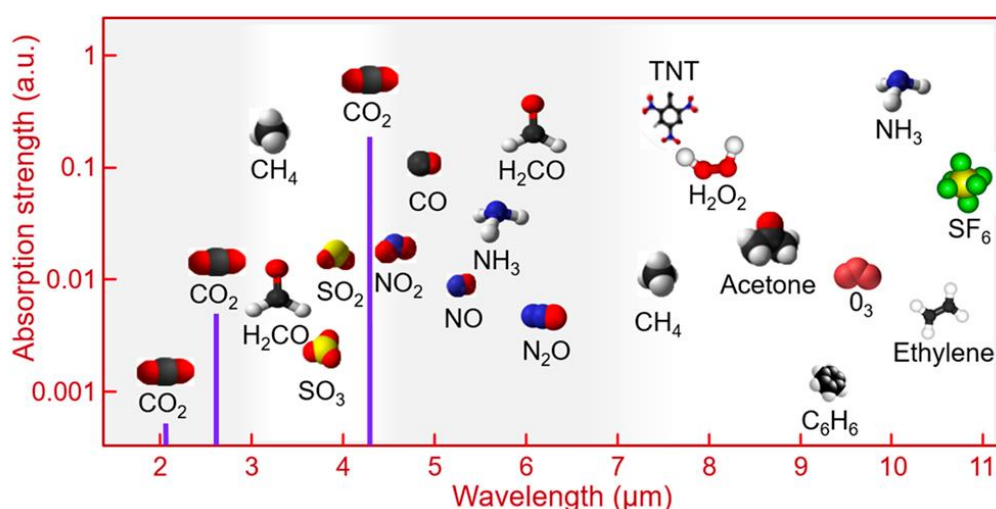


Figure 1.1. The absorption of multiple molecules in MIR. These molecules are of great interest for industrial, security or medical applications [9].

The strong absorption of incident light allows for highly sensitive spectroscopy, such as for atmosphere pollutant monitoring [10] and explosive detection [11]. Notably, a sensitivity down to ppm level of greenhouse gas was recently demonstrated using air-born system at telecommunication wavelengths [12] – an even higher sensitivity can be expected with MIR band source due to better absorption. From a purely scientific point of view, this band also opens opportunities to study water molecules, who have fundamental vibration band about 2800 nm, in different physical states. These applications require a coherent, stable and narrow linewidth optical source covering the band of interest in MIR.

In medical application, selective photothermolysis (SP) applies the preferential heating of target tissue leading to less denatured neighboring tissues and was studied using medical free electron laser (FEL) [7]. It has been found that laser surgery at wavelength of 6.45 μm is more effective in cleaving of protein bonds and has less scattering to surrounding tissues [7]. The O-H bond in water also has a fundamental vibration frequency at 2.8 μm (or 3950 cm^{-1}), which is another targeted spectral window for surgery.

On the other hand, the atmosphere has multiple transmission windows in the MIR band (Fig. 1.2). The atmospheric transparency in the 2 – 2.5 μm window enables secure optical free-space optical communication systems, remote sensing and LIDAR techniques [13-16]. Two other atmospheric windows lie in 3-5 μm and 8-13 μm wavelength band. In an early research, it was proven that the performance of 8.1 μm free space communication system is superior to 850 nm under dense fog [17].

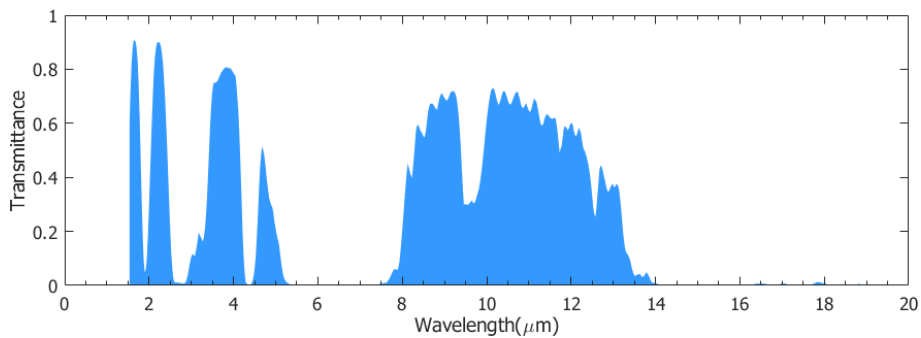


Figure 1.2. Atmosphere transmission as a function of wavelength. In this model, the sensor is at 50 km altitude. Atmospheric visibility is 23 km. The temperature is 294.2 Kelvin. The data is generated using online data base of [18]

1.1.2 Coherent MIR light source

Due to the presence of vibration bonds in the MIR, many optical materials for coherent light sources experience high losses. This is a more severe issue for optical waveguides which have a long interaction length and small mode area. For gain medium, the phonon energy of the host material must be much lower than the photon energy of the designed wavelength, to avoid non-radiative transition [19, 20]. As such, most MIR components consist of low-phonon energy materials. In this section, we briefly review multiple types of coherent MIR sources. The scope of this part is limited to solid-state sources, who have the highest density of states.

Like a laser, one can place a nonlinear gain medium into a resonator to create an optical parametric oscillator (OPO). Thanks to the broad gain bandwidth, OPOs have wide emission range. In 1972, Swedish scientists demonstrated the first optical parametric amplification and optical parametric oscillator using a KDP crystal [21]. OPOs are among the earliest coherent light sources and have experience more than 40 years of continuous development [22]. Till today, they are still one of the most reliable and widely used optical source in laboratories around the world. OPOs are known for achieving great tunability, high peak power, short pulse duration and high pulse quality. In the near infrared and MIR bands, the periodically poled lithium niobate (PPLN) allows for a tuning range from 975 nm to 4.55 μm thanks to the large gain bandwidth and high transparency [23]. Due to the long wavelength absorption of PPLN, the maximum emitting wavelength limit is about 5 μm [24]. To reach further in the MIR, different crystals, such as CdSiP_2 [25], orientational-patterned GaP (OP-GaP) [26] and OP-GaAs [27] are under exploration and in various application stages. As a free space optical resonator, OPOs are highly sensitive to mechanical vibration. In addition, perturbation of air path length can lead to cavity length change, hence a shift of idler wavelength [28]. Therefore, despite their impressive performances, OPOs require precise alignments and careful maintaining. Recently, people started leveraging the high conversion efficiency (CE) of nonlinear crystals as single path wavelength converters for generation of MIR optical frequency combs. PPLN [29] and OP-GaP [30] are two noticeable examples.

In the 1994, researchers from Bell lab proposed and demonstrated quantum cascade laser (QCL) operating as MIR band solid-state lasers [31]. The cascaded energy level gives QCL a good tunability in principle. Researches have also demonstrated the self-mode-locking operation of a QCL [32]. However, since the excited electron has many ways to lose energy without emitting a photon, the efficiency of QCLs is low and

requires proper diode material to achieve lasing at different wavelength range [33]. Thus, a single QCL material can typically support only about 1 μm tunability [33], which is even smaller if converted into the frequency domain. Besides, when operating at long wavelengths, non-radiative processes, such as multi-phonon decay, have a much higher probability to happen. Thus, a MIR QCL requires external temperature control. On the other hand, the operation of a QCL below 3 μm is still challenging [34]. As a rectangular waveguide, further beam shaping is required for QCL to reach a Gaussian spatial distribution [35].

Doping a host glass or crystal with active ions is another way to build a laser in the MIR region. An Er^{3+} doped YAG crystal can lase at 2900 nm and can accommodate a broad pump wavelength range [36, 37]. For better operation in the MIR, people exploited the transition metal II-VI laser crystal – ZnSe/S crystals with Cr^{2+} or Fe^{2+} dopants. The Cr:ZnSe/S crystal covers from 1.8 to 3.4 μm [38, 39] and Fe:ZnSe/S covers the range of 3.4 to 5.2 μm [39, 40]. Recently, lasers utilizing such crystals have already entered the market with both ultrafast pulsed and continuous wave (CW) options [41]. A few month ago, researchers have demonstrated 4.24 μm laser using Fe:ZnSe micro-crystal [42]. Like other lasers utilizing laser crystals, the main part of the laser remains in free-space. To build more robust and compact lasers, one option is to consider fully fiberized architectures.

With their prolonged interaction length and large surface area, optical fiber sources enable distributed heat dissipation and high output efficiency. By fusion splicing cavity components, fiber lasers are generally more robust and compact than their free-space counterparts. Due to the silica-oxygen bond vibration, silica fibers are excessively lossy in the MIR region. Until today, the longer CW silica fiber laser can only reach 2198.4 nm [43]. Soft glasses have lower phonon energy, hence allowing for lasing at longer wavelengths. The most common examples are doped fluoride fibers, such as $\text{ZrF}_4\text{-BaF}_2\text{-LaF}_3\text{-AlF}_3\text{-NaF}$ (ZBLAN). With a low phonon energy of approximately 500 cm^{-1} [44], depending on the exact ratio of each fluoride compound, more phonons are required to cross the energy gap and thus a maximum emission of about 3.1 μm can be expected. The operation of a femtosecond Er-doped ZBLAN was demonstrated at 2.8 μm in 2015 [45]. Because of the limitations on dopant selection, multi-phonon decay (~ 3.2 μm for 6 phonons) and increasing linear losses beyond 3.5 μm [46], ZBLAN fiber lasers are not likely to be able to reach more than 3.5 μm . On the other hand, ZrF_3 and InF_3 fluoride fibers show good transmission beyond the ZBLAN window [46]. In 2017, Maes et al. demonstrated 5.6 W laser operation at 3.55 μm using Er-doped ZrF_4 fiber

[47]. Laser operation beyond 4 μm is feasible by doping InF_3 with Dy^{3+} or Ho^{3+} – the host InF_3 fiber can transmit up to 5 μm . In 2018, an Australian group demonstrated 4 μm fluorescence using a Dy-doped InF_3 fiber [46]. Later in the same year, they showed a CW 4 μm laser using Ho-doped InF_3 fiber laser operating at room temperature [48].

To operate at longer wavelength, Chalcogenide glasses (ChGs) are very good candidates. The transmission window of ChGs can slightly vary depending on the composition. Typically, sulfide-based ChG has a transparent window from 0.8 to 7 μm , selenide-based ChG is transparent from 1 to 10 μm and tellurite-based ChG can transmit from 2 to 12 μm [49]. However, due to the increase of phonon energy induced by oxides in gallium lanthanum sulfide (GLS), the first and currently the only rare earth doped ChG laser emits at 1.08 μm [50]. To avoid adding the oxides, people have changed direction to Ge-Sb-S, Ge-As-Se and Ge-As-Se-Te hosted glasses. In 2014, photoluminescence was observed inside a Pr-doped GeAsGaSe fiber in wavelength range of 3.5 to 5.5 μm [50]. There are other groups working on this topic and in different research stages, such as [51-53]. Although it is known that Er^{3+} dopants lead to clusters inside ChG, internal gain around L-band region was recently observed inside Er-doped As_2S_3 waveguide [54]. It should be noted that great progress has been made since the work on doped GaLaS in the late 90's, but the research on doped ChG fiber lasers is still at the very basic stage. Until now, no MIR fiber lasers are built from doped ChG fibers. Research groups are currently in early stages of doped fiber development, such as numerical modeling [55, 56], material loss optimization [57, 58], and emission spectrum characterization [52, 53, 59]. In addition, the lack in MIR fiber-based optical components (particularly beyond 4 μm) and material aging of ChG induce further challenges.

Another way to develop MIR coherent light source is to utilize nonlinear optical effects inside optical fibers. Thanks to the small mode area and long interaction length, multiple coherent nonlinear processes can be utilized for coherent MIR sources. As nonlinear parametric process involves virtual energy levels with femtosecond lifetime, they support a large bandwidth in the frequency domain. Degenerated four-wave-mixing (DFWM), all-normal dispersion supercontinuum generation (ANDi SCG) and dispersive wave (DW) generation are the most widely used methods. The excessive loss of silica in the MIR region excludes it from the potential host fiber for MIR coherent sources. The generation of MIR coherent light based on nonlinear effects in non-silica glasses has seen many advances during the years 2016 to 2018. A far-detuned FWM is demonstrated in 2018 using a suspended core fiber (SCF) [60]. In 2017, Canadian researchers showed a DFWM using tapered ChG fiber and confirmed well-defined

phase matching condition follow perfectly with simulation [61]. With ChG tapers, it is possible to generate a multi-octave spanning MIR SCG with only 4.2 kW peak power [62]. Very recently, researchers have demonstrated DW generation until 7 μm using a suspended silicon waveguide and performed preliminary tests with dual-comb spectroscopy (DCS) [63]. However, all the above-mentioned experiments were carried out using a femtosecond or picosecond pump source.

The purpose of this thesis is to exploit the possibility of efficient MIR light generation using ChG fibers. The good transparency of ChG in MIR is already known from 1950s [64]. A tapered ChG fiber possesses a 1000 times larger nonlinear parameter than a silica highly nonlinear fiber (HNLF) [65, 66], making it an ideal platform for MIR nonlinear applications. Using DFWM with a CW pump, the properties of the idler wave is almost entirely dependent on the signal laser, which could be in the telecommunication band, thus allowing for multiple applications. Strong nonlinearity and high MIR transparency also make ChG fiber a promising platform for ANDi SCG. On the other hand, as ChG fiber is still a less developed platform, there are still many concerns about this material, especially for CW applications. Thus, the project also aims to check the power handling, CW operation stability and damage mechanism of these fibers, which are all critical for out-of-lab application.

1.2 Main contributions

The followings are the main contributions of my thesis:

Characterization and design of ChG PCFs for efficient FWM in MIR

A good starting point of this project is to study and characterize fibers with different materials and geometries. For efficient far-detuned FWM, the nonlinear fiber not only needs a proper zero dispersion wavelength (ZDW), but also must have a good uniformity [67]. In the first few characterizations, I have performed low power FWM with AsSe, GeAsSe and AsS fiber. The experimental results show that ChG photonic crystal fiber (PCF) geometry is a better platform than the ChG SCF. More importantly, it confirms the high quality of the GeAsSe PCF which is available from the market. Using the initial test results, a proper fiber geometry is designed for better CE, larger conversion bandwidth and a blue-shifted ZDW.

Demonstration of amplified parametric conversion using CW pumping scheme

It was long believed ChG fibers can only sustain kW/cm^2 level of CW power [68, 69]. Inspired by a report in 2015 from US naval lab [70], we believe ChG fibers should have better power handling abilities. With improved fabrication and proper preparation of test samples, I managed to send more than $6 \text{ MW}/\text{cm}^2$ intra-core power intensity at 1950 nm. Using the tapered GeAsSe PCF, I have achieved the first amplified parametric conversion in the MIR region in any $\chi^{(3)}$ waveguide platform under CW laser pumping. Detailed linear and nonlinear characterizations showed no degradation of ChG fiber. Multiple tapers drawn from the same ChG fiber spool showed that such results are repeatable.

Demonstration and optimization of fiber lasers for operation at 2.1 μm

The fabricated ChG PCF has a smaller hole-pitch ratio than our targeted design, hence exhibits a longer ZDW than aimed for. From our experimental test and simulations, the fabricated PCF has a ZDW at beyond 2.1 μm . To reach longer operational wavelength, the active fiber is changed from Tm-doped silica to Ho-doped silica fiber. For a more efficient lasing and less cavity loss, I have designed and characterized a new cavity featuring a polarization-maintaining fiber Bragg grating (PM FBG) as the wavelength selection element. This configuration allows a polarization extinction ratio of more than 99.997% at 2.1 μm lasing wavelength with truly all-fiber cavity.

Observation and study of fiber fuse in ChG PCF

In our experiment with MW/cm^2 intra-core intensity experiments, I noticed a fast and backward propagating damage in some of the tapered ChG PCFs. After inspection of fiber facet and polishing the fiber longitudinally, I confirmed the first observation of backward propagating optical discharge in non-silica glass fiber – fiber fuse. For almost twenty years [71, 72], people believed the damage in ChG fiber is purely thermal and distinct from fiber fuse (or optical discharge) in silica fiber. In this investigation, I proved this point is wrong. In addition, I have conducted the first ever study on the impact of fiber fuse beyond the fused region in PCF. The results showed clear dispersion change due to deposition of ChG gas onto the walls of air holes. Because of the extended damage, fiber fuse poses greater threat to PCF systems than conventional fibers.

Demonstration of a linearly chirped SCG using ChG PCF

Without tapering, our GeAsSe PCF has a highly linear normal group velocity dispersion (GVD) until $2.95\text{ }\mu\text{m}$. With its high nonlinear parameter of $1.7\text{ (W}\cdot\text{m)}^{-1}$, it is possible to pump the fiber at Tm-Ho laser band and output a wide-spanning SCG. In this experiment, I demonstrated an ANDi SCG with 3 dB bandwidth of 27.6 THz centered at $2.08\text{ }\mu\text{m}$ using sub-cm length of ChG PCF at 2.9 kW of peak power. In addition, the evolution of the SCG in terms of both power and fiber length fit perfectly with my simulations. By simulating the spectrogram of the output pulse, I proved that the output pulse has a linear chirp.

1.3 Thesis structure

In the beginning of this thesis, I will cover the theories behind all the experiments. In **chapter 2**, as a starting point, I summarize and explain the theories and numerical methods behind all my experiment. Chapter 2 starts with the basic pulse propagation theory inside an optical fiber, including both linear and nonlinear optical effects. Then I show the famous generalized nonlinear Schrodinger equation (GNLSE) governing the linear and nonlinear processes in optical fibers, which can be solved numerically using the split-step Fourier method (SSFM). For CW pumped parametric conversion, I go through the development of coupled-wave equation. With proper assumptions and simplifications, I show the analytical solution of these equations. Using these analytic solutions, I develop the figure-of-merit (FOM) as the reference for selection fiber geometry and material.

Experimental investigations of the designed fibers start with building the pump laser. Thus, in **chapter 3**, I describe the available dopants, Thulium and Holmium, in silica fibers for lasing at 2 μm . Following a brief introduction of the experimental setup, I show the laser performance of different tested cavities with Tm-doped and/or Ho-doped laser. For the signal Tm-doped fiber laser, I show a new cavity allowing for lasing until 2.107 μm with only 1.7 W L-band pump power. The 2.1 μm pump laser linewidth and polarization stability, slope efficiency and output power stability are detailed described. At last, I show the importance of using a narrow linewidth laser for this project.

Once the pump is fixed, we can move on to the selection of right fiber material and fiber geometry combination. In **chapter 4**, I review the current state-of-art MIR fiber platforms, including glass, crystal and hollow core fibers. I then explain the reasons for the choice of ChG fiber based on its optical properties and fabrication maturity. For more freedom in dispersion engineering, microstructured fiber is preferred. I then show the good uniformity of the GeAsSe PCF which has the possibility to be tapered. With these preliminary experimental results from ChG PCFs and SCFs, I explain the reasons for selection of the PCF structure.

After the pump laser configuration and sample fiber structure is set, the thesis moves to the main results on CW pumped FWM in **chapter 5**. Based on the characterization results from GeAsSe PCF, I show the designed tapered PCF geometry and dispersion characteristics. Using the tapered GeAsSe PCF, CW pumped amplified parametric conversion is recorded at MIR region. A full characterization, signal sweep

and CE-pump relation is then stated in detail. Unfortunately, the fabricated PCF taper is off from the designed value, which is confirmed by simulation and experiment.

In **chapter 6**, I describe the observation and confirmation of fiber fuse in ChG PCF. At last, I show the modified dispersion of PCF due to the deposition of ChG vapor on the PCF air holes.

At last, I show the fiber a good platform for generation of linearly chirped ANDi SCG. In **chapter 7**, I first explain the experimental setup and components' properties. Then, the preliminary results using long fiber length proves the feasibility of experiment and accuracy of simulation. After that, the thesis covers the pump pulse evolution in different fiber length and at different pump power levels. A calculated spectrogram follows and show the linear property of the pump pulse. Next part illustrates a simulation of pulse compression by purely removing the GDD. At last, the impact of water absorption and SCG stability is studied.

In the end, the **chapter 8** makes a conclusion and suggest future works on improved ideas of coherent MIR source based on ChG fibers.

Chapter 2

Light propagation in an optical fiber

2.1 Introduction

Similar to the electromagnetic wave in radio frequency (RF), optical waves can only interact with each other indirectly through an optical medium. Inevitably, the study of nonlinear optical effects in this thesis starts by the treatment of light-matter interaction. Naturally, the frequencies of all evolved light must lie beyond the resonance frequency of the nonlinear material, if one intends to build an optical source. Therefore, this chapter only focuses on the non-resonant nonlinear optical responses.

With this assumption, the polarization $\mathbf{P}(\mathbf{r}, t)$, or unit dipole, induced by an incident light can be written as [73]:

$$\mathbf{P}(\mathbf{r}, t) = \epsilon_0 [\chi^{(1)} : \mathbf{E}(\mathbf{r}, t) + \chi^{(2)} : \mathbf{E}^2(\mathbf{r}, t) + \chi^{(3)} : \mathbf{E}^3(\mathbf{r}, t) + \dots] \quad (2.1)$$

where ϵ_0 is the electric permittivity of the material, $\mathbf{E}(\mathbf{r}, t)$ is the incident electric field. In Eq. (2.1), $\chi^{(n)}$ is the n-th order optical susceptibility tensor. Optical fibers studied in this thesis are all made from amorphous glass material. Thus, the tensor product simplifies to scalar product due to the material symmetry. Since amorphous materials are macroscopically centrosymmetric, the even terms of optical susceptibility will vanish. Thus, the very first nonlinear term for glass fiber is the $\chi^{(3)}$ term, referred as third order nonlinearity. The very next nonlinear term, $\chi^{(5)}$, is roughly 10^{-24} times that of the third order nonlinearity term [74], hence can be safely neglected in this thesis.

Apart from nonlinear effects, light propagation in an optical fiber also experiences linear changes from material dispersion, waveguide dispersion and linear loss. In addition, the linear and nonlinear optical phenomenon are coupled effects on optical pulse evolution in the waveguide. The generalized nonlinear Schrödinger equation (GNLSE) is an accurate and proven tool to study optical pulse evolution. Based on the input light properties, some terms can be neglected and could even lead to an analytical solution.

This chapter will start with the linear propagation of light inside an optical fiber. Before going into any nonlinear effects, we first define some terms that are generally used in nonlinear fiber optics. Then, using coupled wave equations, we find the parameters governing FWM in optical fibers. At last, we explain the femtosecond pulse evolution inside an optical fiber and the simplification of GNLSE for this thesis.

2.2 Linear propagation in optical fibers

The term “linear” could have slightly different definition depending on the discipline. In this thesis, and widely accepted in fiber optics, we would consider the optical effects that are independent from input light average and peak power as “linear effects”. Following this definition, both linear propagation loss and chromatic dispersion fall within this category.

2.2.1 Propagation loss of ChG optical fiber

Inside an optical fiber, the linear propagation losses mainly come from the bending loss scattering and material absorption. When an optical fiber is bent, the outer side of the guided mode needs to travel faster than the inner side to keep the wavefront. If the bending curvature is large enough, the wavefront can no longer be kept, hence leaking out some portion of the energy. The bending loss becomes trivial if one straightens the fiber or keeps large enough bending curvature. In the ChG microstructured fibers, the linear propagation loss mainly originates from interface scattering and material absorption.

Using highly purified ChG glass preforms and proper fiber drawing parameters, the linear propagation loss can be greatly suppressed. Unlike conventional step index fibers, the microstructured fibers also have scattering at interface between fiber material and air. In Fig. 2.1(a) and (b), we sketch the geometry of ChG SCF and PCF tested in this project, respectively. Here, the scattering on the interface due to imperfect smoothness is the main source of scattering loss. For most of ChG fibers, such interfaces are the main reason of aging and loss increase during storage, no matter SCF

[75], PCF [76] or step indexed tapers [77, 78]. To avoid such problems, our ChG fibers are stored in dry atmosphere (below 30% relative humidity). Due to a smaller exposure with air, we expect a slower degradation speed of PCF than SCF. To lower the scattering loss, another way is to operate at longer wavelength, since Rayleigh scattering is inversely proportional to λ^4 .

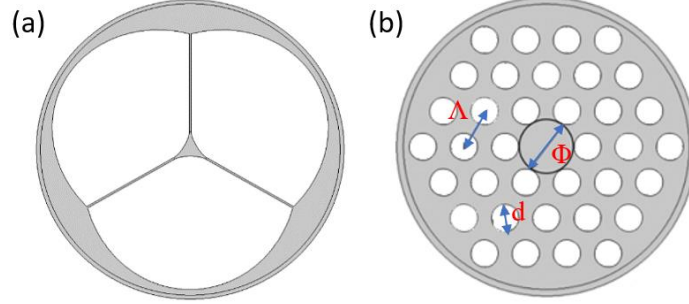


Figure 2.1. Facet geometry of two microstructured fiber geometry. (a) Geometry of a suspended core fiber; (b) geometry of a 3-ring photonic crystal fiber. Λ and d is the hole period and diameter, respectively. Φ is the effective core diameter. We have simulated and experimented with both fiber geometries in this project.

Another source of linear loss results from the material absorption. Generally, it comes from absorption of both fiber material and impurities from either glass or atmosphere. Both -S and -Se based ChGs transmit well into the MIR band. Fig. 2.2 is the transmission of “grape fruit” microstructured GeAsSe and AsS fibers [79]. Both fibers show good transmission after 2 μm wavelength. The several absorption peaks are due to pollution of the fiber preform. While the 2 μm wavelength is not at the minimum loss point, it represents a good compromise between accessibility with fiber lasers and ChG fibers transmission windows.

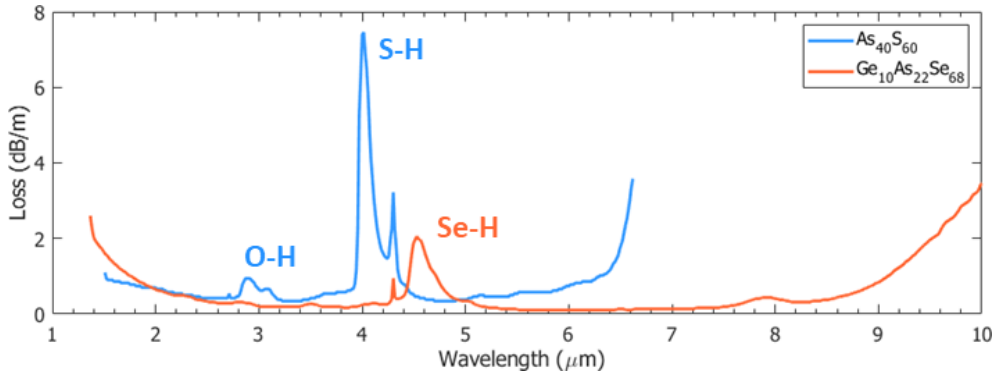


Figure 2.2. Linear loss of $\text{As}_{40}\text{S}_{60}$ and $\text{Ge}_{10}\text{As}_{22}\text{Se}_{68}$ microstructured fibers after fabrication. Data comes from [79].

Experimentally, we estimate the linear loss α using cutback measurements. Since the linear loss leads to an exponential decrease of pump laser power along the fiber, it is directly related with the strength of nonlinear optical effect. The impact of linear loss becomes less significant for propagation length L much less than the effective length

L_{eff} which will be covered in chapter 2.3. For our project, the typical linear loss is measured to be less than 1 dB/m in the 2 μm band. Thanks to the strong nonlinearity of ChG fibers, only meters of fiber are needed for efficient nonlinear process, satisfying $L < L_{eff}$.

2.2.2 Chromatic dispersion

In this section, all the discussions will assume non-resonant operation. The response of a dielectric medium to an incident electromagnetic wave is frequency dependent, leading to different refractive index. Thus, the phase velocity inside a medium will be frequency dependent. One can describe a medium's refractive index using the Lorentz modal. Far from the resonant frequencies, one can calculate the refractive index of a material using Sellmeier equation [80]:

$$n(\lambda)^2 - 1 = \sum_i^n \frac{A_i \lambda^2}{\lambda^2 - \lambda_i^2} \quad (2.2)$$

where λ_i and A_i are the i^{th} resonance wavelength and its strength, respectively. In most cases, three terms will be enough to provide an accurate estimation. The Sellmeier equation terms of AsS, AsSe and GeAsSe comes from previous literatures [1, 64, 81]. It should be noted that Sellmeier equation is not the only fitting function nor necessarily the best fitting. We are using this equation due to its availability.

Unlike conventional step-index fibers, the PCF features a modified total internal reflection guiding, where the air hole filled region serves as an effective cladding. Apart from material, waveguide structure also has frequency dependent propagation constant. The waveguide dispersion is a result of the distribution of mode profile variation at different wavelengths, which determines the mode overlapping in fiber core and cladding. Thus, it is possible to tune the waveguide dispersion by varying the fiber geometry. Tapering the fiber is one way to change fiber core size, hence the waveguide dispersion. Unique to the PCF geometry, the hole-period ratio, ρ , of the cladding will alter the fiber dispersion. The design parameter is defined as:

$$\rho = \frac{d}{\Lambda} \quad (2.3)$$

As illustrated in Fig. 2.1(b), d is the diameter of air hole and Λ is its period.

The chromatic dispersion comes from the combination of material dispersion and waveguide dispersion. For simplicity, the effective refractive index n_{eff} is used to represent their combined effect. In this case, the propagation constant β is:

$$\beta = n_{eff} \frac{2\pi}{\lambda_0} \quad (2.4)$$

The term $\frac{2\pi}{\lambda_0}$ is the vacuum wavenumber. Normally, the chromatic dispersion is expanded using Taylor expansion.

$$\beta = \beta_0 + \beta_1(\omega - \omega_0) + \frac{1}{2}\beta_2(\omega - \omega_0)^2 + \frac{1}{6}\beta_3(\omega - \omega_0)^3 + \dots (2.5)$$

The expansion is made around a central frequency ω_0 . The term β_0 is the propagation constant at this frequency. β_1 corresponds to the inverse of the group velocity and β_2 is typically referred as group velocity dispersion (GVD). The sign of β_2 term tells if blue or red wavelengths travel faster. The higher order terms become important when one studies supercontinuum generation, operation near ZDW or evolution of femtosecond pulses.

Previous researches have shown that third order nonlinear susceptibility is proportional to the first order or linear susceptibility [82]. Naturally, one can expect ChG has the highest nonlinear refractive index among all fiber glasses (typical refractive index from 2.4 to 2.9 at 1.5 μm). However, with a bandgap around 2 eV [83, 84], ChG also has the strongest material dispersion among all fiber glasses. Using their corresponding Sellmeier equation, one can estimate that the ZDW (Fig. 2.3) for AsS is approximately at 5 μm and beyond 7 μm for -Se based glass. One needs to induce strong dispersion engineering on the fiber geometry to counterbalance the material dispersion and shift ZDW close to 2 μm if fiber laser pumping is to be used, which will be a central point of the thesis

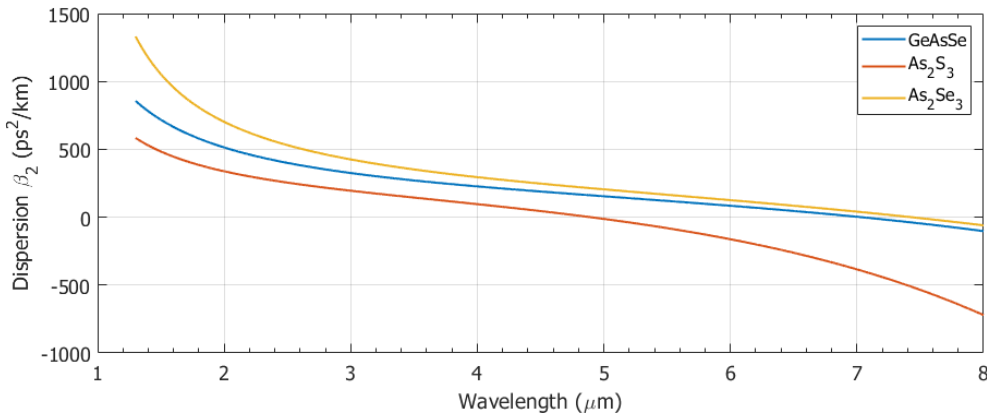


Figure 2.3. Material dispersion of As_2S_3 , As_2Se_3 and $\text{Ge}_{11.5}\text{As}_{24}\text{Se}_{61.5}$ chalcogenide glasses. All of them can be used as platform for suspended core fibers and photonic crystal fibers.

However, dispersion engineering also leads to more fabrication challenges. Thus, we need to consider the available technology and work with multiple degrees of freedoms. Detailed dispersion engineering will be discussed in chapter 5, based on initial experimental results.

2.3 Nonlinear propagation in optical fibers

2.3.1 Definition of parameters

In nonlinear fiber optics, it is common to use the nonlinear refractive index n_2 during the theoretical derivations. The third order susceptibility χ^3 and n_2 have the following relation:

$$n_2 \cong \left(\frac{3\chi^{(3)}}{4c\epsilon_0 n^2} \right) \quad (2.6)$$

The real part of the nonlinear refractive index is responsible for the Kerr effect. The imaginary part of the refractive index is the two-photon absorption (TPA). They are normally written as [73]:

$$n(\omega) = n_0(\omega) + n_2(\omega)I \quad (2.7)$$

$$\alpha(\omega) = \alpha_0(\omega) + \alpha_2(\omega)I \quad (2.8)$$

$n_0(\omega)$ and $\alpha_0(\omega)$ are the linear refractive index and absorption, respectively. $n_2(\omega)$ is the nonlinear refractive index and $\alpha_2(\omega)$ is the nonlinear absorption coefficient. I is the irradiance of incident light. In guided wave optics, it is always more convenient to convert the Kerr nonlinearity into the following equation:

$$\gamma = (n_2\omega_0)/(A_{eff}c) \quad (2.9)$$

The term γ , which has the unit of $(W \cdot m)^{-1}$, is the nonlinear parameter of a waveguide with an effective area of, A_{eff} [85]:

$$A_{eff} = \frac{(\iint_{-\infty}^{\infty} |F(x, y)|^2 dx dy)^2}{\iint_{-\infty}^{\infty} |F(x, y)|^4 dx dy} \quad (2.10)$$

where $F(x, y)$ is the transverse field dispersion of the mode under study.

The Kerr nonlinearity term is responsible for self-phase modulation (SPM), cross-phase modulation (XPM) and four-wave-mixing (FWM). Those effects are termed as elastic nonlinear processes, where the total optical energy remains constant. When light interact with optical (Raman scattering) or acoustic phonons (Brillouin scattering), a small portion of the optical energy converts into the phonon energy. These effects are termed as inelastic nonlinear effects. In this thesis, we mainly focus on the theories and applications with elastic processes.

2.3.2 CW four wave mixing

In a DFWM process, two pump photons excite the electron into a virtual energy level. When electron returns to the ground level, the transition emits one signal photon and one idler photon. When a signal photon is sent together with the pump photon, as shown in Fig. 2.4, the spontaneous process becomes stimulated FWM, hence with a much higher efficiency. In this thesis, we use the DFWM process to transfer a signal at L-band to the MIR band.

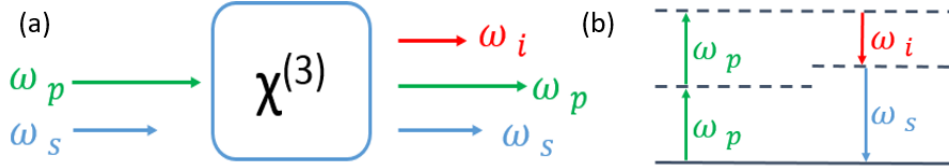


Figure 2.4 Schematic of FWM process. (a) Demonstration of a degenerated four-wave-mixing process, (b) where two pump photons from the same frequency generated two new photons at different frequencies. The newly generated frequency depends on the phase matching condition of the medium.

For a sustained interaction among the four photons, the system must conserve both its momentum and energy. In addition, the nonlinear change on the material refractive index would also impact the system's momentum. Since the relation of momentum and energy of photons can be treated as propagation constant and angular frequency, respectively, the momentum and energy conservation can be expressed mathematically, as:

$$\kappa = \Delta k + 2\gamma P_0 = 2\beta_p - \beta_s - \beta_i + 2\gamma P_0 = 2\gamma P + \frac{1}{2}\beta_2\Delta\omega^2 + \frac{1}{12}\beta_4\Delta\omega^4 \quad (2.11)$$

$$2\omega_p = \omega_s + \omega_i \quad (2.12)$$

where ω_p , ω_s and ω_i are the pump, signal and idler angular velocities respectively; β_p , β_s and β_i are the propagation constants of pump, signal and idler respectively. $\Delta\omega$ is the angular velocity difference between signal and pump which is the same as the difference between pump and idler. κ is normally referred to as the phase mismatch. P_0 is the pump peak power. The term Δk is the linear phase mismatch. The term $2\gamma P_0$ in Eqn. (2.11) is the nonlinear phase mismatch.

For this section, we only consider the FWM under the CW or pseudo-CW (defined as [86]) case. In this case, the evolution of optical field amplitude can be expressed as [85]:

$$\frac{\partial A_1}{\partial z} = jn_2k_1 \left[\left(f_{11}|A_1|^2 + 2 \sum_{k \neq 1} f_{1k}|A_k|^2 \right) A_1 + 2f_{1234}A_2^*A_3A_4e^{j\Delta kz} \right] - \frac{\alpha_1}{2}A_1 \quad (2.13)$$

$$\frac{\partial A_2}{\partial z} = jn_2k_2 \left[\left(f_{22}|A_1|^2 + 2 \sum_{k \neq 2} f_{2k}|A_k|^2 \right) A_2 + 2f_{2134}A_1^*A_3A_4e^{j\Delta kz} \right] - \frac{\alpha_2}{2}A_2 \quad (2.14)$$

$$\frac{\partial A_3}{\partial z} = jn_2k_3 \left[\left(f_{33}|A_3|^2 + 2 \sum_{k \neq 3} f_{3k}|A_k|^2 \right) A_3 + 2f_{3412}A_1A_2A_4^*e^{j\Delta kz} \right] - \frac{\alpha_3}{2}A_3 \quad (2.15)$$

$$\frac{\partial A_4}{\partial z} = jn_2k_4 \left[\left(f_{44}|A_1|^2 + 2 \sum_{k \neq 4} f_{4k}|A_k|^2 \right) A_4 + 2f_{4321}A_1A_2A_3^*e^{j\Delta kz} \right] - \frac{\alpha_4}{2}A_4 \quad (2.16)$$

Here, the term $A_i(z, t)$ is the amplitude of the incident field. We define $A_{1,2}$ to be the pump wave. A_3 and A_4 then become the signal and idler wave, respectively. The term f_{ik} is the mode overlap integral. This integral determines the overlap of energy between different waves, which is critical for XPM and FWM efficiency. Normally, this term is defined as:

$$f_{ik} = \frac{\iint_{-\infty}^{\infty} |F_i(x, y)|^2 |F_k(x, y)|^2 dx dy}{\iint_{-\infty}^{\infty} |F_i(x, y)|^2 dx dy \iint_{-\infty}^{\infty} |F_j(x, y)|^2 dx dy} \quad (2.17)$$

The other term, f_{ijkl} is the transverse overlap integral given by

$$f_{ijkl} = \frac{\langle F_i^* F_j^* F_k F_l \rangle}{\left[\langle |F_i|^2 \rangle \langle |F_j|^2 \rangle \langle |F_k|^2 \rangle \langle |F_l|^2 \rangle \right]^{\frac{1}{2}}} \quad (2.18)$$

In order to solve these equations analytically, a few assumptions are necessary. First, we assume the pump power is much higher than both signal and idler waves. In this case, we can assume an un-depleted pump for wave A_2 and A_1 over the entire interaction. Then, we assume the transverse mode of all the four waves are the same. In this case, the overlapping integral can be reduced to $f_{ijkl} \cong \frac{1}{A_{eff}}$. We assume the involved waves are CW. Also, the nonlinear refractive index is independent of optical frequency/wavelength. With these simplifications, we can assume a constant nonlinear parameter γ . For a more straightforward solution, we also assume the fiber is lossless. The lossless model has very high accuracy when our ChG fiber has less than 1 dB/m loss and short fiber length around 1 m. In the end of this chapter, we show the

simulation methodology for lossy fiber using a simplified nonlinear Schrodinger equation.

For DFWM close to the pump wavelength, i.e. $\omega_s \sim \omega_p \sim \omega_i$, the converted power from pump to signal is identical to the converted power from pump to idler. With these assumptions, the signal gain (G_s) and CE can be deduced by solving Eqn. (2.13) to (2.16), and is given by [85] as the signal gain G_s :

$$G_s = \frac{P_3(L)}{P_3(0)} = 1 + \frac{(\gamma P_0 r)^2}{4g^2} \sinh^2(gL) \quad (2.19)$$

$$CE = G_s - 1 \quad (2.20)$$

L is the fiber length. The parameter r is defined as:

$$r = \frac{2\sqrt{(P_1 P_2)}}{P_0}, P_0 = P_1 + P_2 \quad (2.21)$$

The total pump power is P_0 . Clearly, $r = 1$ for the single pump configuration. The parameter g is the parametric gain:

$$g = \sqrt{(\gamma P_0 r)^2 - (\kappa/2)^2} \quad (2.22)$$

From Eqn. (2.22), we can find two interesting regimes. First, we study the regime when linear phase mismatch dominates the nonlinear phase shift, that is when $\Delta k \gg \gamma P_0 r$. In this case, Eqn. (2.22) becomes an imaginary term and the \sinh term becomes imaginary. The original Eqn. (2.19) can be reduced into a sinc function.

$$G_s \cong \frac{(\gamma P_0 L r)^2}{4g^2} \text{sinc}^2(\kappa L/2) + 1 \quad (2.23)$$

When pump wavelength resides in the region of high group velocity dispersion (typically with pump wavelength far from ZDW), the signal gain follows Eqn. (2.23). By sweeping the signal wavelength, one should record a clear *sinc* shape of the CE. The sharpness of the dips serves as an indication of fiber loss and uniformity. From the Eqn. (2.23), one can find that the signal gain and idler CE both increase quadratically with the pump power and fiber length. In such case, when linear dispersion dominates, we can deduce the fiber GVD at the pump wavelength using Eqn. (2.11).

If one has perfect linear phase matching, the term Δk vanishes to zero. Under strong parametric gain $\gamma P_0 r \gg 1$, Eqn. (2.19) can be approximate to

$$G_s \cong \frac{1}{4} \exp(\gamma P_0 L r) \quad (2.24)$$

Here, the signal gain (or CE of idler) increases exponentially with the pump power and fiber length. However, the maximum gain peak does not happen at $\Delta k(\omega) = 0$. Due to the nonlinear phase mismatch, the gain peak always appears at $\Omega_{max} = \pm\sqrt{2\gamma P_0/|\beta_2|}$.

As we can see, under the phase mismatched case, the DFWM (single pump) can produce a CE with *sinc* function shape. By sweeping the signal, one can record the CE trace at different pump power levels and monitor the fiber structural variations. From Eqn. (2.23), the first dip (first minima of the sinc function) appears when:

$$\sqrt{\left[\frac{\beta_{2,pump}\Delta\omega^2 + 2\gamma P_0}{2}\right]^2 - (\gamma P_0)^2} \cdot L = \pi \quad (2.25)$$

Solving this equation and taking the only physical solution, the frequency difference from the first dip and the pump wavelength is therefore:

$$|\Delta\omega| = \sqrt{\frac{-4\gamma P_0 + \sqrt{(4\gamma P_0)^2 + 4(2\pi/L)}}{2\beta_2}} \quad (2.26)$$

In terms of wavelength, one can expect the first dip at

$$\lambda_{dip} = 2\pi c_0/(\omega_{pump} + |\Delta\omega|) \quad (2.27)$$

When designing the nonlinear platform, it is always more convenient to have a figure-of-merit (FOM) to estimate the platform's performance. In this case, we assume all potential waveguides can be fabricated to their corresponding effective length. The effective length is defined as the propagation length inside a lossy medium to the propagation of the length of lossless medium with equivalent nonlinear phase shift. As a result, the nonlinear phase shift inside a lossy medium of length L becomes equivalent to that of a lossless medium of length L_{eff} . The effective length is derived to be:

$$L_{eff} = \frac{1 - e^{-\alpha L}}{\alpha} \quad (2.28)$$

For a rough estimation of parametric amplification/conversion performance, we can consider the two extremes:

1. Not phase matched, $\Delta k + 2\gamma P_0 \gg \gamma P_0$

$$Gs(L) \approx 1 + (\gamma P_0 L_{eff})^2 \cdot \text{sinc}^2\left((\Delta k + 2\gamma P_0)L_{eff}/2\right) \propto \gamma P_0 \cdot \frac{1 - e^{-\alpha L}}{\alpha} \propto \frac{\gamma}{\alpha} \quad (2.29)$$

2. Perfectly phase matched, $gL \gg 1$

$$Gs(L)|_{dB} \approx 2\gamma P_0 L_{eff} \cdot (\log_{10}(e) - \log_{10}(4)) \propto \gamma P_0 \cdot \frac{1 - e^{-\alpha L}}{\alpha} \propto \frac{\gamma}{\alpha} \quad (2.30)$$

In both cases, the parametric amplification/conversion performance is proportional to γ/α . If any necessary waveguide length can be fabricated, we can therefore use the term γ/α as a FOM for the platform selection reference. The same FOM definition is also used for silica HNLFs for quick estimation of their performance [87].

By fitting the experimental result with simulation, one can deduce the fiber linear loss under the same un-depleted pump assumption. In the lossy case, the solution to the coupled-wave equation is way more complex and cannot provide straightforward insight to the physical conditions behind [86]. If the pump laser lies far from ZDW, one can also use a simplified nonlinear Schrodinger equation as

$$j \frac{\partial}{\partial z} A(z, t) + j \frac{\alpha}{2} A - \frac{\beta_2}{2} \frac{\partial^2 A^2}{\partial t^2} + \gamma A |A|^2 = 0 \quad (2.31)$$

To simulate the conversion efficiency at various signal wavelength, one can set the pump and signal as two points on the frequency domain. By sweeping the signal in every loop, the CE can be built in a large wavelength region.

2.3.3 Nonlinear propagation of a pulse in fibers

Since the linear and nonlinear optical effects are coupled, the generalized nonlinear Schrodinger equation (GNLSE) is used to simulate short pulse propagation inside an optical waveguide. As light is an electromagnetic wave, the propagation of an optical pulse can be well described by Maxwell's equations. By taking the nonlinear polarization into the wave function, one can include the nonlinear effect as:

$$\nabla^2 \mathbf{E} - \frac{1}{c^2} \frac{\partial^2 \mathbf{E}}{\partial t^2} = \mu_0 \frac{\partial}{\partial t^2} (\mathbf{P}_{NL} + \mathbf{P}_L) \quad (2.32)$$

The polarization is now decomposed into the linear P_L and nonlinear P_{NL} terms. Starting with this equation, one can derive the GNLSE to simulate the propagation of a slowly varying envelope A [88].

$$\frac{\partial A}{\partial z} - \underbrace{\sum_{k \geq 2}^N \frac{i^{k+1}}{k!} \beta_k \frac{\partial^k A}{\partial T^k}}_{\text{Dispersion}} + \underbrace{\frac{\alpha}{2} A}_{\text{Linear loss}} =$$

$$i\gamma \underbrace{\left(1 + \tau_{shock} \frac{\partial}{\partial T}\right)}_{\text{Kerr Self-steepening}} \times \left[A(z, t) \left(\underbrace{\int_{-\infty}^{+\infty} R(T') |A(T - T')|^2 dT'}_{\text{Raman}} + \underbrace{i\Gamma_R(z, T)}_{\text{Spontaneous Raman noise}} \right) \right] \quad (2.33)$$

Here, T is the new reference frame moving at the pulse group velocity:

$$T = t - \beta_1 z \quad (2.34)$$

The term $R(T)$ and $\Gamma_R(z, T)$ are the Raman contribution and spontaneous Raman scattering. A more detailed discussion on the $R(T)$ is in the end of this chapter.

In Eqn. (2.33), we put the linear terms on the left-hand side and the nonlinear terms on the right-hand side. Each term is labeled with their physical representation. Note that the group velocity term vanishes by changing the reference frame to the same speed of the pulse envelope. The term $\tau_{shock} = \frac{1}{\omega_{pump}}$ is the shock term, which characterizes the self-steepening effect – an effect originated from intensity dependent refractive index. In order to simulate of ANDi SCG, only the terms above red brackets need to be considered. Due to the short length and low loss of the ChG PCF, we can also ignore the loss term. The pump laser is a sub-100 fs laser, whose spectrum content can cover the 1st Raman stoke of GeAsSe glass. Thus, the spontaneous Raman noise can be neglected. In addition, we have omitted the TPA term. Since we are focussing on a pumping wavelength at 2 μm which is far from the bandgap of ChG, the contribution of TPA is trivial.

The Kerr effect term includes FWM, XPM and SPM. For ANDi SCG, the spectral broadening is dominated by the SPM and optical wave breaking (OWB) effect. The SPM effect was first observed as early as 1967 [89]. When propagating inside an optical fiber, the pulse experiences an intensity dependent nonlinear phase shift. This effect leads to a decrease of the pulse peak power and a broadening of pulse spectrum. Normally, the nonlinear phase shift, $\phi_{NL}(z, T)$, and its induced chirp, $\delta\omega(T)$, which depend on the propagation distance z and time t , are expressed as

$$\phi_{NL}(z, t) = -\gamma P(z, t)L \quad (2.35)$$

$$\delta\omega(t) = -\gamma L \frac{\partial P(z, t)}{\partial t} \quad (2.36)$$

For the simulation of input pump pulse, it is important to use proper fitting by considering the nature of the pump source. In Fig. 2.5, we show a simulation of SPM

for Gaussian and sech^2 pulses. As a result, for a fundamental soliton pulse pump, the use of Gaussian model would degrade matching between simulation and experiment. For the location with the same amount of induced nonlinear chirp, the resulting interferences lead to the well-known oscillations in the frequency domain.

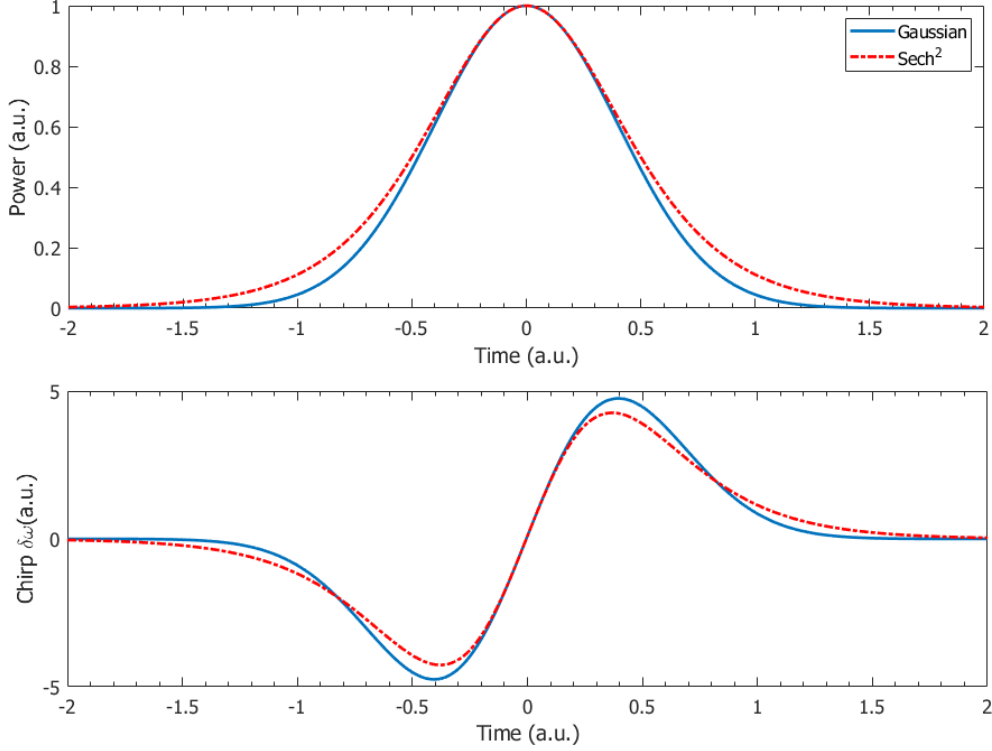


Figure 2.5. Comparison of Gaussian and sech^2 pulses. (a) The temporal profile of a Gaussian pulse (blue) and a sech^2 pulse; (b) The corresponding chirp, where only nonlinear phase shift is included in the simulation. Here we simulate a SPM phase shift of π radians

When interacting with dispersion, the pulse behavior can be very different in normal and anomalous dispersion regions. In the normal dispersion region, the chirp induced by SPM and chirp induced by dispersion have the same direction. The GVD and SPM will increase the temporal domain broadening and lead to a rectangular shaped temporal signal [90]. Such effect is advantageous for generating ultra-flat top SC and pulse re-compression [91, 92]. On the other hand, the anomalous domain will lead to formation of solitons, if the SPM and GVD properly cancel each other. Together with Raman effect, the fundamental soliton can self-shift to longer wavelengths while losing part of its energy [93]. The fundamental soliton is a solution of sech form to the NLSE. Thus, the sech pulse fitting will be used for laser sources utilizing soliton self-frequency shift.

The self-steepening term comes from the result of intensity dependent refractive index. This effect results in a pulse distortion which leads to an increase sharpness in the trailing edge of the wave.

The last term is the Raman effect. The stimulated Raman effect comes from the photon-phonon interaction in the optical medium, when the incident photons interact with the molecular vibrational modes. During this interaction, the photon converts part of its energy to an optical phonon resulting in a red-shifted wavelength. The Raman scattering is typically modelled as a damped oscillator [88]:

$$R(t) = (1 - f_R)\delta(t) + f_R h_R(t) \quad (2.37)$$

On the right-hand side of Eqn. (2.37), the first term corresponds to the instantaneous Raman response and the second term is the delayed response. The factor f_R corresponds to the contribution fraction of the delayed Raman response. The Raman response function $h_R(t)$ is normally described as:

$$h_R(t) = \frac{\tau_1^2 + \tau_2^2}{\tau_1 \tau_2^2} \exp\left(-\frac{t}{\tau_2}\right) \sin\left(\frac{t}{\tau_1}\right) \quad (2.38)$$

For AsSe ChG, the parameters are measured to be [94]

- $f_R = 0.148$ - delayed Raman contribution
- $\tau_1 = 23fs$ - inverse phonon frequency
- $\tau_2 = 164.5fs$ - phonon lifetime

Conclusion

The theories in this chapter are the fundamental guidelines for fiber design and experimental data processing. In the low power FWM experiments, we retrieve the fiber parameters by fitting simulation with experimental data. These precisely measured fiber parameters then allow us to predict ANDi SCG in frequency and temporal domain accurately. With these proven data and simulation, we can bring out reliable new fiber designs for broadband and distant wavelength conversion.

Chapter 3

Fiber lasers at 2 μm

3.1 Introduction

In chapter 2, we described that all ChGs have very strong material dispersion while efficient FWM requires pumping around the fiber ZDW. On the one hand, strong dispersion engineering can be performed on fiber geometry in order to blue shift the ZDW. On the other hand, we can approach the ZDW from the red side by building fiber lasers operating at longer wavelength. As silica fibers are the most widely used and most fiber optical components are based on such fibers, we decided to rely on this technology for the design of our fiber lasers. Indeed, as ChG fibers are still a relatively new platform, it is more reasonable to build their pump lasers using available and mature technology. In silica fibers, the maximum phonon energy is 1000 cm^{-1} [95]. Due to the multi-phonon relaxation process, efficient silica fiber lasers are limited at 2200 nm [43, 96]. Given this constrain, we cannot use any transitions beyond 2.2 μm , where 5 phonons can effectively bridge the bandgap. Due to this reason, the only two active dopants available to use are thulium (Tm) and holmium (Ho) ions.

Both Tm- and Ho- doped silica fibers are available on the market from multiple vendors. For efficient lasing and high ASE suppression, we will try to operate the fiber lasers around the ASE peak. Therefore, we use multiple fiber lengths to blue or red shift the ASE center. Due to re-absorption of the photons, the ASE peak experiences redshift in longer active fiber, similar to what is observed in erbium doped fibers. By proper design of the laser cavity and careful selection of cavity components, it is possible to build a signal laser and a pump laser for FWM measurements covering the range from 1880 to 2100 nm.

In this chapter, we will start with the introduction of the pumping schemes for both dopants. Then we will show the experimental setup for the FWM test. For easier operation and construction, we use the C- or L-band erbium doped fiber amplifier (EDFA) as the pump source. Based on this pump, we will show several cavity schemes and compare their performance on Tm-doped fiber lasers. Then we move to the 2.1 μm pump laser based on Ho-doped fibers. Due to the fast-increasing loss of silica fiber beyond 2 μm , it is more challenging to build an efficient laser. In this section, we introduce the polarizer-free all-fiber Ho-doped fiber laser, which can provide more than 99.997% polarization extinction ratio with high stability. In the end, we will show the importance of having a narrow linewidth laser, based on some of our experimental results.

3.2 Experimental setup for FWM

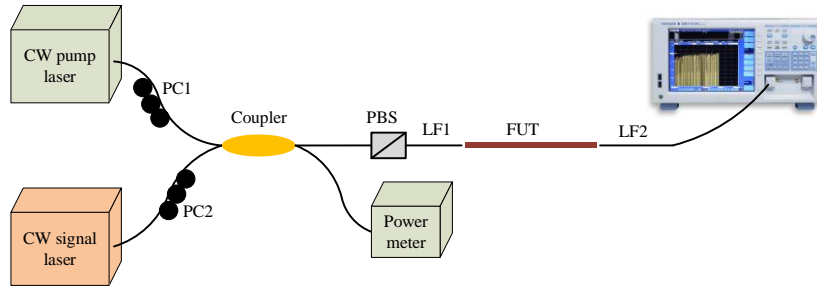


Figure 3. 1. A generalized setup for this project. The pump laser is a fixed wavelength CW laser while the signal laser features a continuous wavelength sweep by using a tunable filter. An optical spectrum analyzer records the data. PC: polarization controller; PBS: polarization beam splitter, to ensure same pump and signal laser polarization. LF: lensed fiber, for in and out coupling; FUT: fiber under test.

In Fig. 3.1, we show the concept of a generalized FWM test setup. Before building the lasers, it is important to design the complete experimental setup. The experimental setup can provide the requirements for the fiber lasers in terms of laser power, linewidth, tunability and polarization extinction ratio. Most importantly, we will here focus on estimating the required powers for the pump and signal lasers. For an efficient FWM process, the polarization of pump and signal lasers should be the same. A commercial polarization beam splitter (PBS) maintains a low insertion loss for wavelength range of 2000 ± 50 nm. For longer pump wavelength, it is preferable to avoid the PBS, which can result in significant additional losses, and align the polarization of pump and signal laser directly, based on the idler power on the optical spectrum analyzer (OSA). In this case, the polarization of pump and signal are adjusted manually in order to maximize the idler power. The signal and pump lasers are combined using an optical coupler before going into the fiber-under-test (FUT). A typical coupling ratio is 90/10, where

90% of pump and 10% of signal power is sent into the FUT. However, depending on the operation wavelength and the efficiency of both lasers, the coupling ratio can be varied to guarantee a detectable idler. More details of the setup will be explained in chapter 4, with specific FUT and laser designs.

For the ChG fibers, the insertion loss ranges from 5 to 10 dB, depending on the fiber mode field mismatch between ChG fiber and input lensed fiber. In the case of 90/10 coupling ratio, we expect an extra 3 dB loss and 13 dB loss for the pump and signal laser, respectively. Under the “High/Chop”, mode, the OSA noise floor appears at -70 dBm. If we set the coupled signal power to 0 dBm, a minimum conversion efficiency of -70 dB can be detected. As we will see, the ChG FUTs typically have a nonlinear parameter γ higher than 1 (W·m)⁻¹ and a length longer than 30 cm. With 100 mW coupled pump power, a CE higher than -30 dB can be expected [67]. In this case, one can clearly distinguish the idler from the OSA noise floor. Therefore, the aimed maximum pump power for pump and signal lasers are 1 W and 20 mW, respectively. Such back of the envelope approximation, allows for significant operation margins and will allow changing the coupling ratio in case either pump or signal laser fail to provide enough power.

3.3 Basics of Tm³⁺ and Ho³⁺-doped fiber laser

In Fig. 3.2, we show the excited energy level transitions for Tm³⁺ and Ho³⁺ ions. Note that some of the transitions will not be accessible inside a host material, due to either multi-phonon relaxation or material photo-darkening. For our Tm- or Ho-doped fiber lasers, we will be utilizing the $^3F_4 \rightarrow ^3H_6$ transition of Tm³⁺ and $^5I_7 \rightarrow ^5I_8$ transition of Ho³⁺ ions, as illustrated in Fig. 3.2. As a result, a C- or L-band laser and a homemade 1950 nm laser work as pump laser for the Tm-doped fiber laser and Ho-doped fiber laser, respectively.

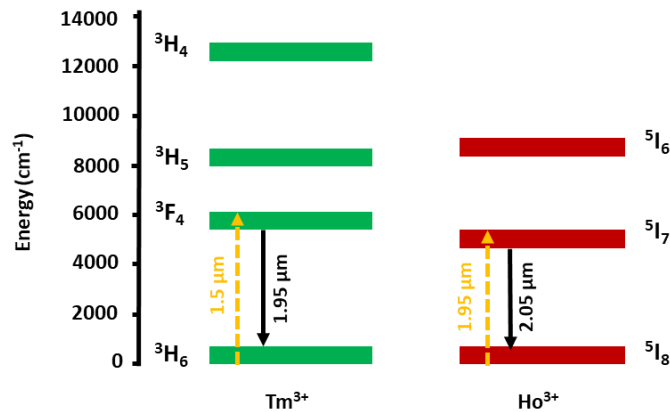


Figure 3.2. The energy level transitions for multiple rare earth ions. In this project, we utilize the in-band pumping scheme for both Tm³⁺ and Ho³⁺ ions.

From Fig. 3.3(a), to excite the ground energy level to the desired excited levels, we can simply use an L-band laser for Tm-doped silica fiber. Experimentally, our L-band EDFA can work efficiently even at 1620nm, where pump can be absorbed more efficiently. For Ho^{3+} , however, the in-band pumping configuration requires to pump at approximately 1950 nm for best pump absorption (Fig. 3.3(b)). Therefore, we would also need to build an efficient 1950 nm laser as a pump for Ho^{3+} . There are several potential configurations, which will be covered in chapter 3.5

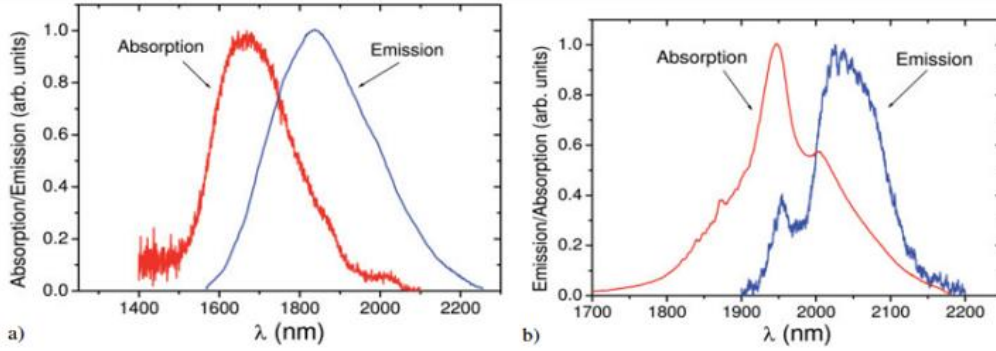


Figure 3.3. The emission and absorption cross-sections of Tm^{3+} (a) and Ho^{3+} (b) [97]. Note that the emission and absorption can experience red shift when doping concentration or active fiber length increases.

Also, from Fig. 3.3, it is clear that Tm^{3+} dopant has a broader emission cross section than Ho^{3+} dopant. For pump laser below 2039 nm, we will use the Tm-doped silica fiber as gain medium. For pump laser of 2100 nm, the gain medium then switches to Ho-doped silica fiber. For the signal laser, we will always utilize the Tm-doped silica fiber since tunability is the most important factor for the signal laser.

3.4 Tm-doped fiber lasers

The FWM experiment requires very little or no tunability for pump laser. For the signal laser, a sweep range of roughly more than 100 nm is desirable for better FWM wavelength coverage. Thus, the wavelength selection of pump laser can be done with fiber Bragg grating (FBG) while the signal laser requires a tunable filter. Both linear and ring cavity configurations have been tested for the two lasers. Initial FWM tests with ChG fibers were performed with, both pump and signal lasers utilized ring cavity configurations. Further FWM tests were then performed using improved linear cavity for pump laser, as the quality of the pump source is critical for improving the precision of the characterization.

3.4.1 Pump lasers

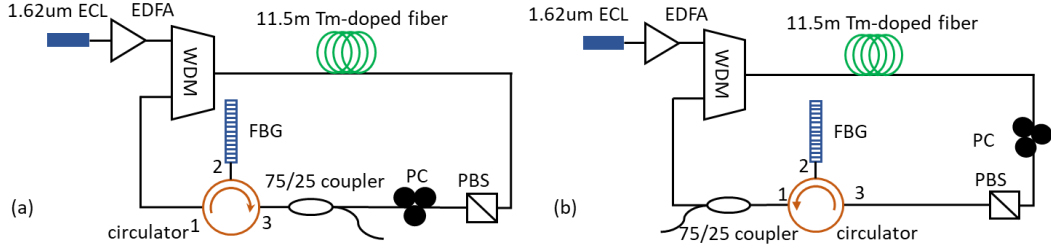


Figure 3.4. Pump laser configurations utilizing backward (a) and forward (b) ASE. We use the forward pump scheme to exploit the red-shifted emission wavelength from Tm^{3+} . ECL: external cavity laser; EDFA: erbium-doped fiber amplifier; WDM: wavelength division multiplexer; FBG: fiber Bragg grating; PC: polarization controller; PBS: polarization beam splitter.

With limited L-band pump power (5W maximum), we need to decrease the component loss inside the cavity and put larger out-coupling ratio. We have used the OFS Tm-doped fiber, TmDF200, as the gain medium. The fiber is a single clad, core pumped, single mode (cut-off at 1350 nm) active fiber. The 11.5 m length is selected for better laser slope efficiency since its ASE peak resides close to 1950 nm. In Fig. 3.4, we illustrate the pump laser cavities utilizing forward and backward pumping scheme. The pump laser wavelength is selected by changing the FBG. For these lasers, FBG for 1980, 2007 and 2039 nm operation were available (with more than 95% reflectivity for all). The insertion loss of the circulator is approximately 2.3 dB per port measured at 2004 nm. The PBS gives an extra loss of 2 dB and the polarization controller has an insertion loss of about 1.5 dB, both measured at 2004 nm. For operation at wavelength up to 2008 nm, the backward amplified spontaneous emission (ASE) is used for better efficiency. For lasing at 2039 nm, we use the forward ASE to benefit from the red-shifted central wavelength. Such implementation can lead to a maximum output power of around 1 W.

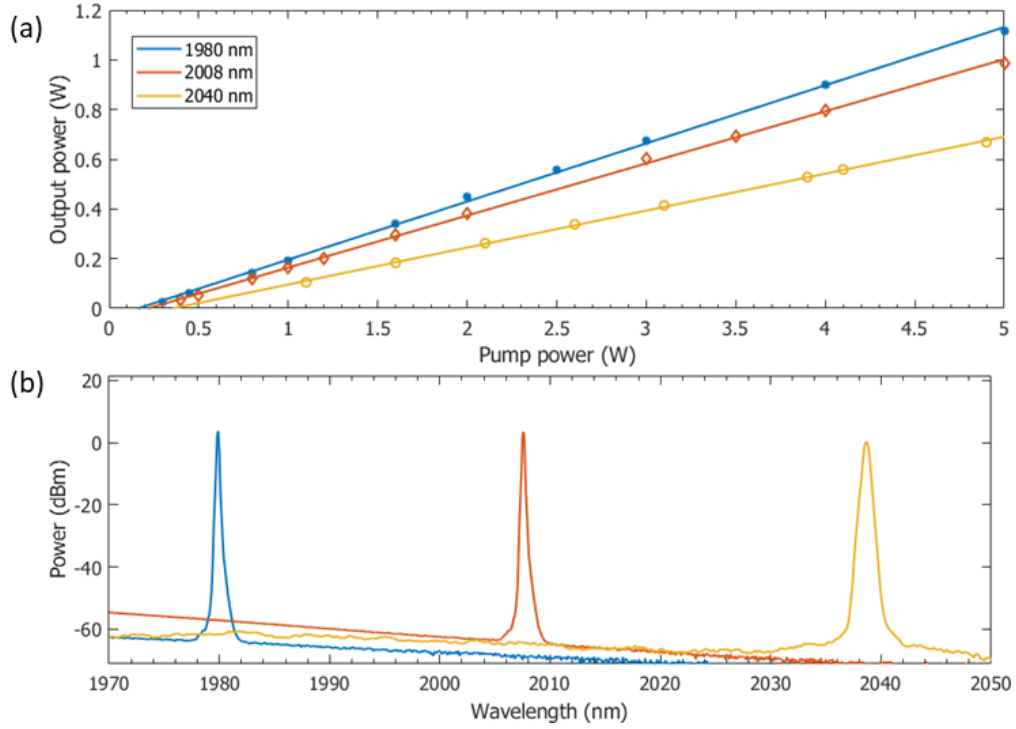


Figure 3.5. The slope efficiency and laser linewidth of multiple pump wavelengths. (a) Slope efficiency for the three lasing wavelengths. (b) Pump laser spectrum for lasing at 1980, 2008 and 2039 nm (resolution at 0.05 nm).

To characterize the pump laser performance, the standard method is to measure the laser linewidth, slope efficiency and lasing threshold. In Fig. 3.5(a), we show the linewidth of 1980, 2008 and 2040 nm lasing wavelength. The ASE for 2040 nm operation follows a slightly different trend due to the forward pumping scheme, since forward pumping scheme favors a longer wavelength emission than backward. For both 1980 and 2008 nm, the laser full width half maximum (FWHM) was measured to be about 0.1 nm. Due to the larger bandwidth of the 2040 nm FBG (0.8 nm FWHM), the FWHM of this laser is approximately 0.45 nm. This large linewidth will lead to strong SPM of pump laser if the ChG fiber has strong enough nonlinearity.

Figure 3.5(b) plots the laser output power as a function of the L-band pump power. At 1980 nm lasing wavelength, the slope efficiency is 23.4 % with lasing threshold at 161.7 mW and maximum output of 1.13 W. For 2008 nm FBG, the laser outputs a maximum 1 W of power with 21.0% slope efficiency. The laser threshold for this case is 217.8 mW. The forward pumping laser at 2040 gives a maximum output power of 0.691 W and a slope efficiency of 14.9 %. Lasing starts at a higher power of 354.6 mW in this case. The low slope efficiency and high threshold of the 2040 nm laser is due to the operation on the edge of Tm^{3+} emission and increased loss of optical components at the 2040 nm wavelength. Since all the components were designed for operation at 2000 nm, they are expected to have a higher loss at 2040 nm.

The cavity design in Fig. 3.5 proves to be efficient and meet our experiment requirement at both 1980 and 2008 nm wavelengths [66]. However, at high pump power, the large bandwidth of the pump laser at 2040 nm induced strong SPM on the pump and hence distorted both the signal and idler light. The larger laser linewidth of the 2040 nm laser leads to more temporal fluctuations of laser power, hence stronger SPM. In addition, during our experiment, we have noticed some pulsing operation of the pump laser near the laser threshold for all FBG wavelengths. This is due to nonlinear polarization rotation (NPR), where the nonlinearity comes from the 20 m in-cavity fiber. However, characterization of the tapered ChG PCFs are preferably performed at very low pump power, to avoid the impact of un-tapered region.

To avoid this problem, we decided to remove the PBS and PC from the laser cavity. In addition, the coupler switches to 90/10 coupling ratio where the 10% port serves as the output. In this case, the pulsing of laser at low output power is eliminated. For characterizing the tapered ChG PCFs (1m length), a 5 mW coupled power guarantees a CE of about -40 dB [66]. For this power level, an extra loss of about 4 dB at the outer-cavity PBS is absolutely tolerable. Therefore, this cavity configuration is ideal for low power characterization of tapered ChG PCFs at various wavelengths, which is done in multiple of our works [66, 67].

In addition, the linear cavity configuration requires much less in-cavity components. They can be simply made by a higher-reflective (HR) FBG and a low-reflective (LR) FBG pair with a Tm-doped fiber in between. The laser wavelength is 1950 nm, so it can also serve as the pump laser for Ho-doped fiber laser. In addition, a linear cavity can be directly incorporated into the Ho-doped fiber laser cavity due to its simple structure. The HR FBG has a reflectivity of 99.5% and 1.5 nm FWHM. The LR or output FBG has a 0.18 nm FWHM and reflectivity of 19.6 %. In between, we still use the 11.5 m of Tm-doped fiber, since its ASE is centered around 1943 nm (Fig. 3.7(b)).

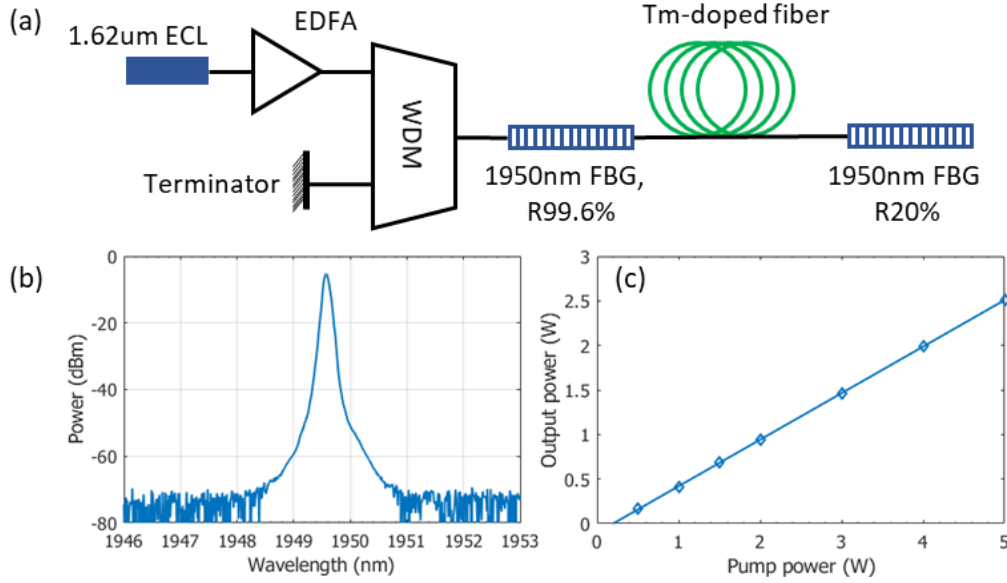


Figure 3.6. The 1950 nm pump laser cavity and output properties. (a) Experimental setup for 1950 nm pump laser. The simple linear cavity allows for a high slope efficiency to provide enough pump power for parametric amplification. (b). The laser output spectrum (c) The laser output relation with the L-band pump power.

The laser setup is illustrated in Fig. 3.6(a). After passing the PBS (Fig. 3.1), the laser can still provide around 1 W to the FUT. The PBS is removed when the laser acts as a pump for Ho-doped fiber. At the maximum output power of 2.51 W, the FWHM of laser is 0.12 nm. The lasing threshold is 197.7 mW, due to the large out-coupling ratio. A slope efficiency of 52.3 % is measured. The WDM was added for protection of the EDFA by directing the laser power leakage from the HR to an optical terminator. It is not an essential part of the laser and can be removed to further increase the slope efficiency and lower the lasing threshold. We have used this laser setup for our work on amplified parametric conversion, characterization of tapered ChG PCF, and construction of 2.1 μm all-fiber laser [98].

3.4.2 Signal laser

The signal laser requires continuous sweeping of wavelength. The wavelength tuning element is a commercial tunable filter. The filter has a tuning range of 1975 ± 75 nm, FWHM of 1 nm and insertion loss about 4 dB. The filter has a polarization dependence due to use of free space grating. Thus, we can expect a polarized output directly from the laser cavity. To reduce the signal laser linewidth, we decrease the out-coupling ratio to 10% and use the minimum required cavity components. The laser features ring cavity as indicated in Fig. 3.7(a). The insertion loss of isolator is less than 2 dB for all the whole operation band of tunable filter.

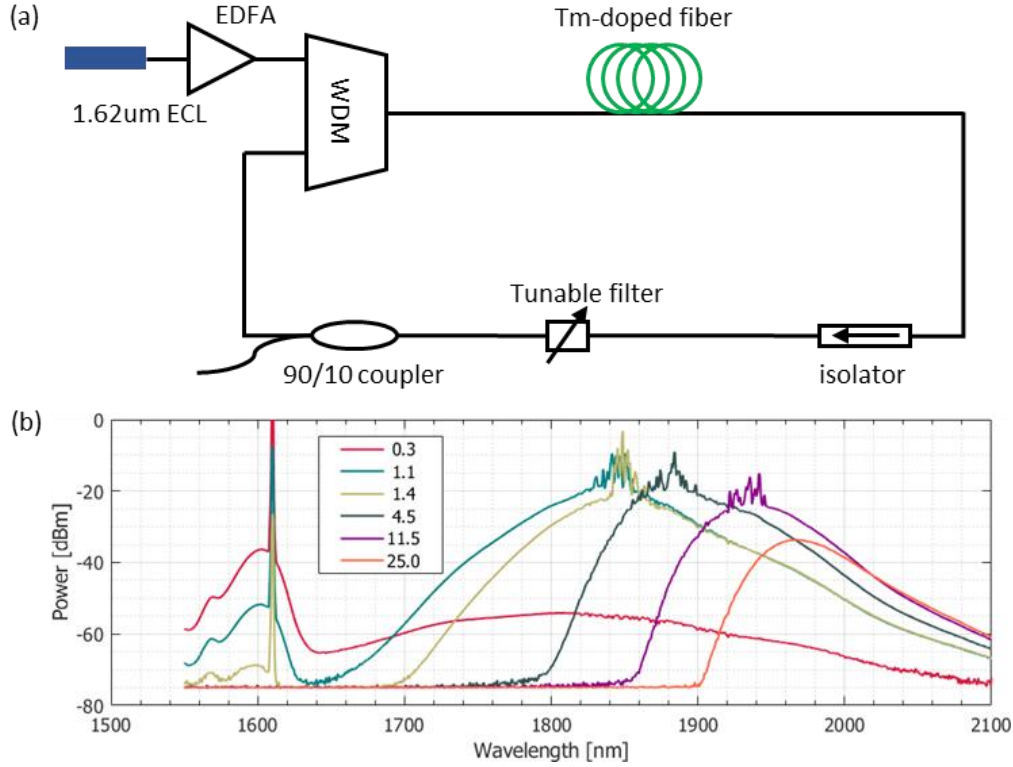


Figure 3.7. Signal laser cavity and ASE for various active fiber lengths. (a) Laser setup for the tunable signal laser. (b) Forward ASE spectrum for different Tm-doped fiber length (credit to Dr. Svyatoslav Kharitonov). The 25 m Tm-doped fiber is necessary for signal laser to reach beyond 2050 nm.

In order to operate more efficiently, we change the in-cavity Tm-doped fiber length for different laser operation range. While keeping the same doping concentration, the Tm^{3+} ASE features stronger red-shift with longer fiber length. Thus, for different sweeping bands, we use a corresponding optimal fiber length for the signal laser. For operation between 1900 to 1950, the Tm-doped fiber length is 1.4 m. For tuning range of 1950~2000 nm and 2000~2050 nm, the 4 m and 11 m Tm-doped fiber spools are used, respectively. Limited by the tunable filter operation range, 2050 nm is the longest lasing wavelength using this cavity configuration. At all the tuning wavelengths, the laser can output more than 50 mW, but more pump power is needed for operation longer than 2020 nm. The maximum laser linewidth (FWHM) of 0.18 nm happens at 2050 nm.

Ideally, the signal laser should be able to operate until 2100 nm. This coverage is necessary when we conduct experiment with 2100 nm pump laser. For L-band core pumped Tm-doped, it is very challenging to reach the 2100 nm wavelength. To the best of our knowledge, there is no report of such lasers. From our side, our limited equipment motivates us to explore the possibility of building such lasers. Therefore, we aim to build a Tm-doped fiber laser with L-band pump which can be continuously tuned between 2000 to 2100 nm. To achieve the design parameters, we need to reduce the number of components inside the laser for minimal inter-cavity loss.

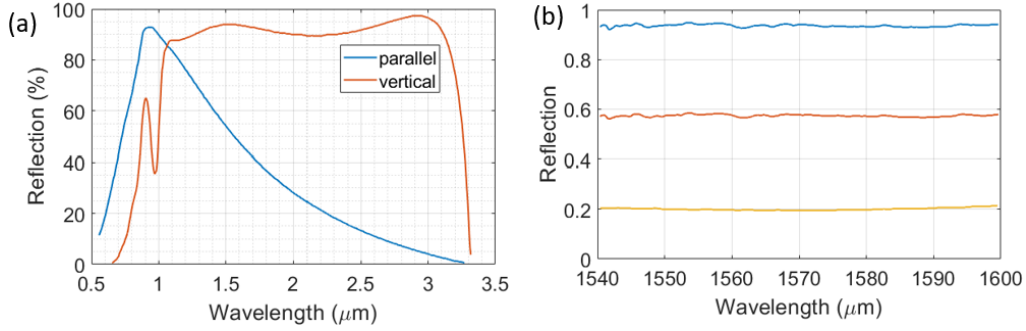


Figure 3.8. The wavelength dependent response of free space grating and fiber loop mirror. (a) The reflection of the grating, GR25-0616 under Littrow configuration (data from [99]); (b) One can perform broadband tuning of the out-coupling ratio (or reflection) in an FLM by inserting a polarization controller in the loop (data from [100]). The curves correspond to reflection percentages accessible from the LM (blue: maximum reflection, yellow: maximum transmission, orange: intermediate). The blue curve indicates maximum achievable reflection while the yellow curve is the maximum achievable transmission.

We worked with a new cavity configuration, where wavelength sweeping is obtained with a free space grating. Also, we use the grating with strong polarization dependent reflection. This would induce polarization selectivity into the cavity, hence removing the necessity of in-cavity polarizer. The Thorlabs GR25-0616 grating meets these requirements, as shown in Fig. 3.8(a). It has good reflection for the band from 1.5 to 3 μm and high polarization selectivity. With a groove density of 600/mm, it also provides a narrow FWHM bandwidth, due to the high spatial dispersion. A triplet collimator, TC12APC-2000, couples light to and back from the grating. This collimator has a $1/e^2$ beam waist diameter of 2.49 mm and operation range of 1880 to 2116 nm. An in-line PC made with SM2000 fiber, controls the input polarization to the grating. The whole assembly (including inline PC) has an insertion loss of 3.8 dB measured using a 2050 nm diode laser. This assembly acts as the HR part for a linear cavity.

The LR or out-coupling component is achieved by using a fiber loop mirror (FLM). By inserting a PC, one can tune the reflectivity of FLM from 0 to $(2R_{oc} - 1)^2$ [100], where R_{oc} is the coupling ratio. This has been demonstrated experimentally and theoretically in previous works [100, 101] [also replotted in Fig. 3.8(b)]. The reflectivity tuning in FLM is valid for both defined polarization and randomly polarized ASE. Due to the insertion loss of the PC, mating sleeves and coupler, the maximum reflection will be lower, and minimum will be higher in real experiment. The broadband 50/50 coupler, TW2000R5A2A, offers a working range of 2000 ± 200 nm and is fabricated with SM2000. Using this coupler, the FLM works as a broadband out-coupling mirror with a tunable reflectivity. Similar to the HR reflector, we use an in-line PC to control the polarization inside the FLM. An insertion loss of less than 1 dB was measured using 2004 nm diode laser.

We sketch the new signal laser setup in Fig. 3.9. To further narrow the laser linewidth, an iris is placed inside the HR reflector/filter. The FWHM bandwidth of this filter is measured to be approximately 0.2 nm. At the laser output, a 90/10 coupler send 90% of light into the power meter (PM) and 10% into the OSA for spectrum recording.

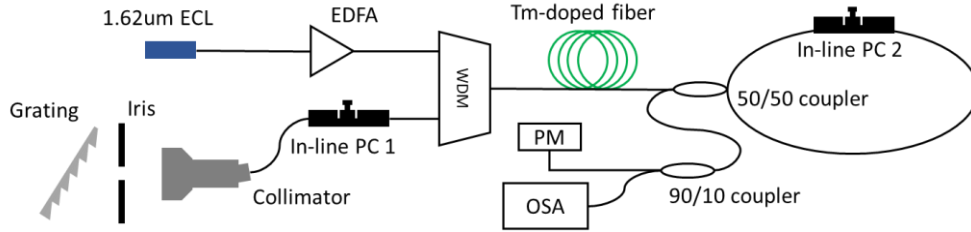


Figure 3.9. Cavity configuration for the new signal laser. This cavity enables signal laser operation up to 2107 nm with Tm-doped silica fiber. The iris helps to stabilize laser line when operating around 2100 nm. PM: power meter; OSA: optical spectrum analyzer.

Using the 25 m Tm-doped fiber as gain medium, the laser can easily cover the range of 2000 to 2105 nm, filling the gap of previous signal laser tuning range. At the maximum operation wavelength of 2105 nm, the ASE suppression ratio is more than 47 dB. Parasitic lasing starts to occur at 2108 nm and cannot be properly suppressed as shown in the black curve of Fig. 3.10(a). The spectrum around 1600 to 1700 nm is a result of OSA stray light [43].

In Fig. 3.10(b), we zoom in the output linewidth of the signal laser. For lasing below 2060 nm, only 1 W of L-band pump is needed. At 2000 nm, the output power is 100 mW and it drops to 40 mW for 2060 nm. For wavelength range of 2060 to 2090 nm, we increased the pump to 1.4 W. At 2080 nm, the output power is 28 mW. To operate around 2100 nm without parasitic lasing, the in-line PC2 is tuned to increase the reflection of FLM, hence reducing the cavity loss at the lasing wavelength. To keep an output power above 20 mW, the pump power is increased to 1.7 W. At this point, the output power reaches 24 mW. Further increase of pump power starts to induce parasitic lasing around 2000 nm. For the entire working range, the laser FWHM linewidth is below 0.09 nm. The polarization extinction ratio is larger than 15 dB for during the entire sweep of lasing wavelength.

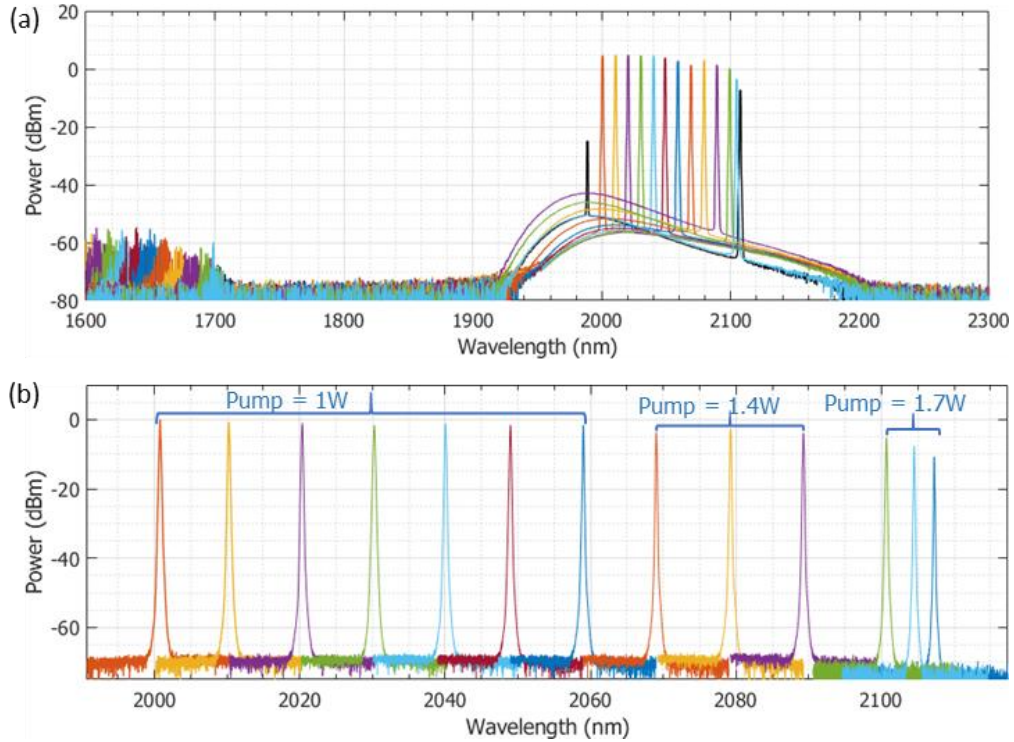


Figure 3.10. The OSA spectrum of improved signal laser using 25 m of Tm-doped fiber. (a) Laser output spectrum with full span of OSA. The resolution is 2 nm. At the wavelength of 2107, parasitic lasing starts to appear and very difficult to compress. Before 2017 nm, the ASE suppression ratio is more than 40 dB. (b) Zoom in of the lasing wavelengths. This cavity configuration covers the entire 2000 to 2100 nm range. We did not show the operation below 2000 nm since this wavelength poses little challenge to Tm-doped fiber laser.

3.5 Ho-doped fiber lasers

3.5.1 Background of 2.1 μm fiber lasers

Though the signal laser utilizing 25 m of Tm-doped fiber laser manages to reach 2.1 μm and is an appropriate signal laser, the slope efficiency and output power are not high enough to serve as a pump laser for FWM in ChG PCFs. For this purpose, we decided to build a 2.1 μm pump laser with Ho-doped fiber as the active medium. An efficient scheme for Ho-doped fiber laser is to use 1950 nm fiber laser as an in-band pump. Due to the limited power of Tm-doped fiber at 1950 nm, such approach required an all-fiber cavity that directly outputs highly polarized light. Since Ho-doped fiber lasers are not as mature as Tm-doped fiber lasers and cannot be pumped with telecom light, building a Ho-doped fiber laser is in general more challenging. The 2.1 μm wavelength has higher transmission and bending loss in silica fibers compared with 2 μm lasers, hence a shorter cavity is preferred. In addition, most optical components are optimized to perform at 2 μm band. Thus, we need to avoid the use of free space components, like

isolator and polarizers, for the cavity design.

Besides, the 2.1 μm CW lasers have found applications in several other aspects besides of the interest of our project. The atmosphere has a low-loss window at the 2.09 \sim 2.1 μm range [14]. Actually, comparison experiment and estimation had been made between a 10 μm CO_2 laser and a 2.1 μm solid-state laser in the 1990s [102]. It was found that 2.1 μm operation out-performs the CO_2 laser under all the tested atmosphere condition [14]. In addition, a solid-state laser offers much more efficient and integrated platform than a gas laser. Therefore, the compact and robust 2.1 μm fiber lasers are attractive for coherent LIDAR [13, 15] and can be potential sources for new optical communication windows for both free-space and hollow core fibers [103]. In both areas of applications, modulation of the laser is essential either for data transmission or to improve the LIDAR performance. Modulators require stable, linearly polarized and narrow-linewidth input. Therefore, developing linearly polarized and long term stable laser source is important for optical system at this wavelength range. A highly-polarized laser offers another degree of freedom for data retrieval, which has been used for a long time in polarization backscattering LIDAR [104]. Besides, the optical system for polarization-related LIDAR applications should possess a high and stable degree of polarization (DOP) [105].

During the past years, intensive studies have been made on the development of 2.1 μm fiber lasers. Using 790 nm diode pumping, Tm-doped fiber lasers can cover 1925nm to 2200nm with a slope efficiency of more than 42% [43]. However, ASE suppression drops around 40dB for wavelength near 2100nm and continue to decrease at longer wavelengths. On the other hand, Ho-doped fiber lasers have an emission cross-section favouring the longer wavelengths and have been demonstrated to lase efficiently until 2171nm. The most efficient 2116 nm wavelength of Ho-doped fiber laser exhibits a slope efficiency of 43% and ASE suppression of more than 50dB [96]. However, up to now, there is a lack of high efficiency lasers emitting polarized light directly from the cavity in this wavelength range. Due to their insertion loss, limited bandwidth (typically \sim 50nm around 2 μm), and low availability as fiberized components, it is preferable to avoid the use of polarizers. Instead high quality polarized light should directly be generated from the laser cavity. In addition, a completely all-fiber and simple cavity design is ideal for long-term stability, power handling and compactness.

3.5.2 Linear cavity design for 2.1 μm fiber laser

Though Tm-doped silica fibers provide broad emission spectrum close to 2.2 μm , it remains a challenge to suppress parasitic lasing around 1.9 μm . For Ho-doped fibers, it is feasible to shift the peak of ASE close to 2.1 μm , by using higher doping concentration and/or longer fiber length. As a result, pump laser for wavelength beyond 2.05 μm utilizes Ho-doped fibers as gain medium. Moreover, we would like to avoid use of free-space polarizers inside laser cavity to further reduce cavity losses. To bypass the polarizer, we use the PM-FBG as a polarization selection element.

As indicated in Fig. 3.11(a), the PM-FBG has Bragg wavelengths centered at 2100.2nm and 2100.7nm on fast and slow-axis, respectively. The bandwidth and reflection for both axes are the same, 0.175nm and 95.85%, respectively. The pump laser is a homemade Tm-doped fiber laser at 1950nm explained in chapter 3.4.1. The maximum output power is approximately 2.3W and has a bandwidth less than 0.1 nm. As shown in Fig. 3.11(b), the output of 1950 nm laser directly goes into the Ho-doped fiber as a pump. A 1.7m of Ho-doped double clad fiber (Nufern SM-HDF-10/130) is used as the gain unit. SMF-28 pigtailed were spliced for core pumping with less than 1 dB loss per splice, measured at 2004 nm. The Ho-doped fiber then goes through an in-line PC to adjust the input polarization to the PM-FBG. By operating the PC, the laser can lase on either or both of the PM-FBG axes. On the other side, a gold coated mirror acts as the HR mirror. The insertion loss of this mirror is 0.8 dB measured at 2004 nm. Basically, this cavity configuration uses the 1950 nm pump cavity as a sub-cavity. Thus, the 2.1 μm light also goes through all the components of the 1950 pump laser.

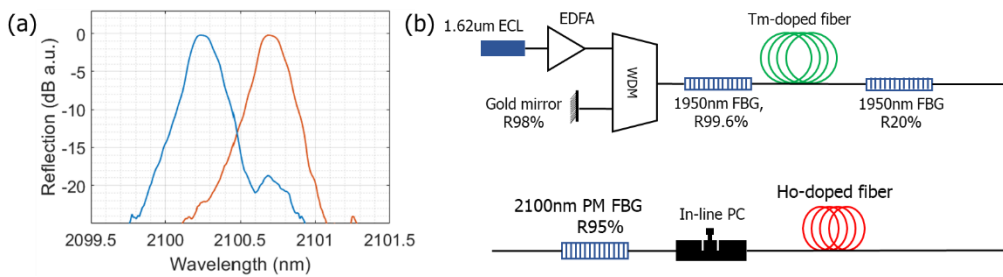


Figure 3.11. The reflection of PM-FBG and laser cavity design. (a) The fast (blue) and slow (orange) axes of PM-FBG. This test is conducted with low pump power. (b) Laser cavity for the polarized Ho-doped fiber laser. The Tm-doped fiber laser serves as the in-cavity pump.

This configuration gives a maximum output power of 321.4 mW as shown in Fig. 3.12(a). The slope efficiency is 17.5 % and the lasing threshold is 600.4 mW in terms of the 1950 nm pump laser. These parameters are the same for both operation at fast and slow axes. In Fig. 3.12(b), we show a zoom in of the laser line when lasing on the

fast axis. The laser FWHM linewidth is no more than 0.06 nm, limited by the OSA resolution. The center wavelength is 2100.3 nm, which is slightly red-shifted due to heat-up of FBG.

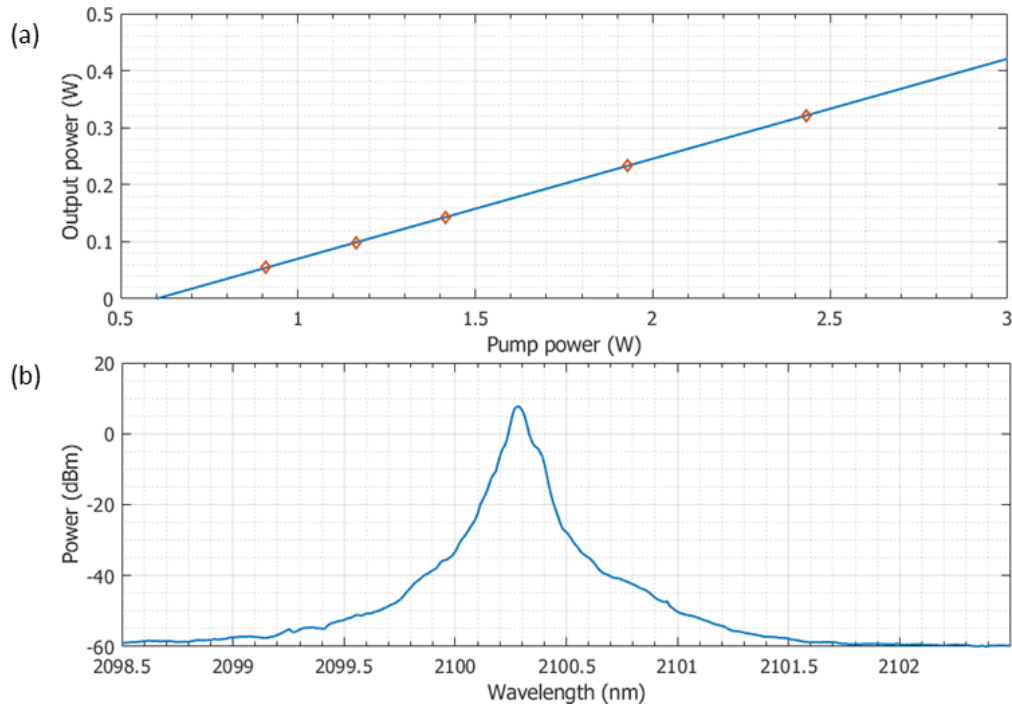


Figure 3.12 Laser property of the 2100 nm pump laser. (a) 2100 nm pump laser slope efficiency; (b) Laser line spectrum under 0.05 nm resolution.

Since 2100 nm PM-FBGs are not widely available on the market, in order to improve the output power and slope efficiency, we looked into optimizing the cavity design. A clear improvement is to move the 1950 nm and 2100 nm lasers into independent cavities with a possibility to bypass the WDM. For 2100 nm laser, the PM-FBG can be the HR. For the LR, we can use FLM for its continuously tunable reflection. Before disassembling the laser cavity in Fig. 3.11(b), we use this laser to characterize the performance of an FLM utilizing an 85/15 coupler and in-line PC. The coupler was also made of SM2000 to reduce losses in the 2.1 μm range. Figure 3.13 is the FLM characterization setup, where two photodiodes, PD1 and PD2, record the transmission and the reflection, respectively.

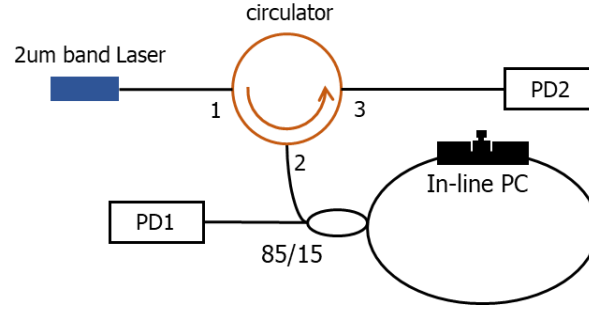


Figure 3.13 Test setup for FLM operation at 2100 nm. The insertion loss from the circulator is compensated in data processing step.

We plot the test results in Fig. 3.14. From simulation, an 85/15 coupler should have a maximum reflection of 49% when both clockwise and counter-clockwise propagations have the same polarization. By tuning the in-line PC, the reflection should drop close to zero. We measured a 0.7 dB insertion loss of this FLM at 2100 nm. The maximum and minimum reflection are 44% and 0.15%, respectively. The maximum transmission and minimum transmission are 88% and 44%, respectively.

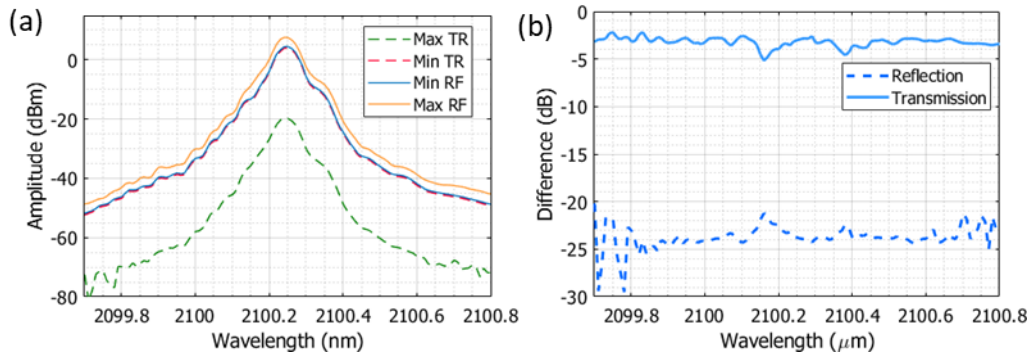


Figure 3.14. The tunable reflection from FLM at 2100 nm. (a). By tuning the inline PC, one can achieve 0 to 50 % of reflection (or 50 to 100% output ratio). (b) The maximum tuning range of the reflection (dashed) and transmission (solid) of the FLM.

The complete laser cavity and characterization setup is illustrated in Fig. 3.15. An SM2000 fiber was inserted inside the inline polarization controllers (PC1 and 2) and each of them has less than 0.4 dB insertion loss (measured at 2004 nm). The previously mention FLM is placed as the LR at the end of cavity. Another inline polarization controller (in-line PC1) was inserted for tuning the reflectivity of FLM, which allows for the switching of lasing axis. We have made multiple tests with this cavity and cavity in Fig. 3.9(b) regarding the position of in-line PC1. We conclude that the optimal position for this PC is right after the PM-FBG. The mating sleeves inside the fiber cavity are labeled with red double diagonal marks in Fig. 3.13. This new cavity configuration makes the pump and Ho-doped fiber lasers into two independent cavities. In this case,

the new Ho-doped fiber laser has a cavity length of about 5 m (or 10 m round-trip length), leading to a reduced loss in silica fiber.

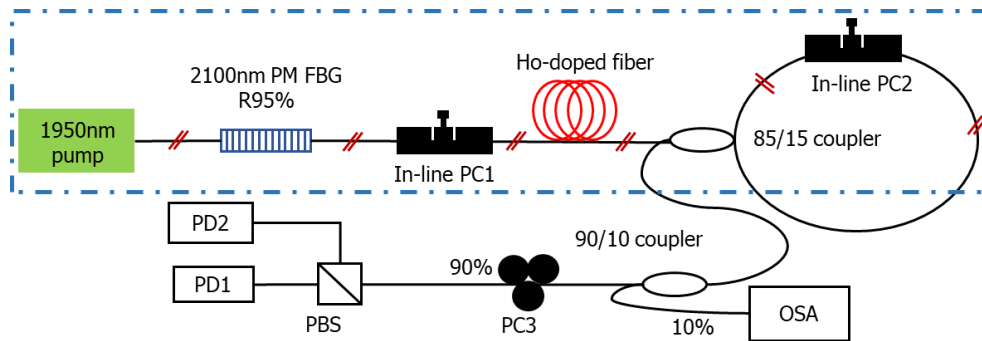


Figure 3.15 Experimental setup of the laser cavity and characterization setup. PM-FBG: polarization maintaining fiber Bragg grating; PD: photodetector;

The monitoring/characterization setup of the laser is indicated outside the dashed box in Fig. 3.15. The laser output is connected to a 90/10 coupler. An OSA is connected to the 10% port for spectrum recording. The 90% coupler port is connected to a 3-paddle PC (PC3) and then through a PBS for power monitoring on both polarization axes. The fiber in PC3 is also SM2000 and has an insertion loss of 2 dB. The semiconductor integrating sphere sensor has a sensitivity of -30dBm, which was used to monitor the low power port of PBS. A thermal detector monitors the high-power port after the PBS.

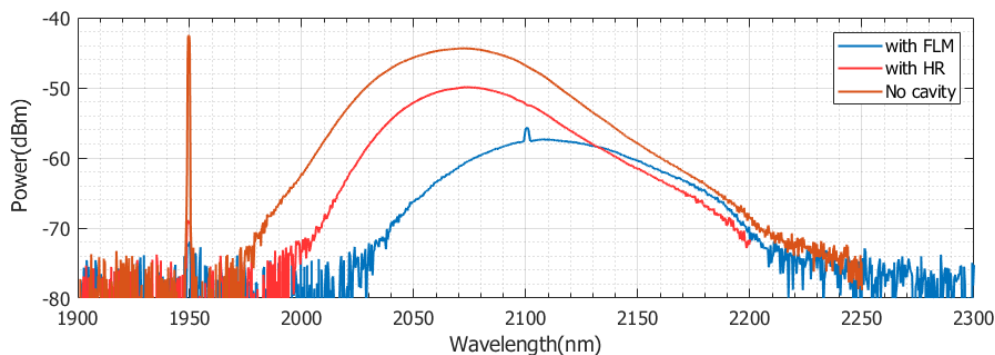


Figure 3.16 ASE spectrum recorded with multiple configurations. FBG-FLM cavity (blue); HR-FBG cavity (red); and forward ASE of fiber (orange). By implementing an FLM with lower reflection, the Ho^{3+} ASE center was red-shifted towards 2100nm.

The forward ASE of our 1.7 m Ho-doped fiber is centered at approximately 2070 nm. We compare the ASE with the previous linear cavity [Fig. 3.11(b)] using a free space mirror as HR to evaluate the effect of the FLM on the laser performances (Figure 3.16). For the cavity in Fig. 3.9(b), the ASE central wavelength (red line) stays roughly the same as cavity-less forward ASE (orange line). Implementing an FLM lowers the in-cavity energy. The gain cross section was redshifted due to less population inversion, which induces a loss favoring long wavelength side [106], thus increasing 2100nm lasing efficiency and ASE suppression (blue line).

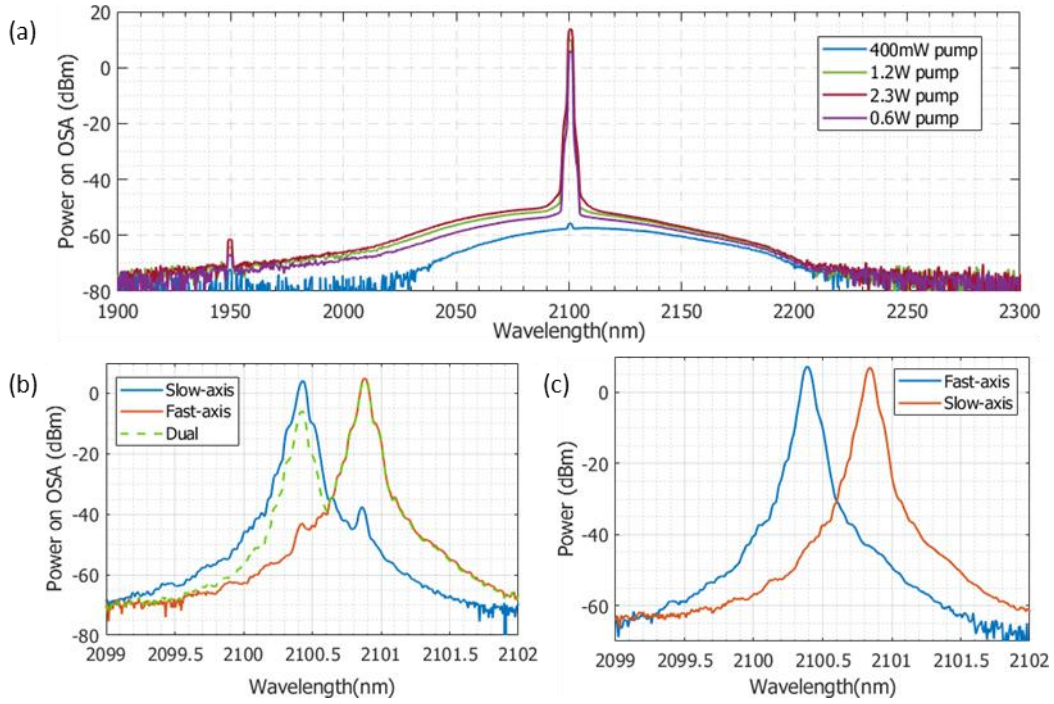


Figure 3.17. OSA record of the laser line spectrum and ASE suppression. (a) Broad range spectrum of laser (2nm resolution). (b) Spectrum recorded on two port of PBS (blue and orange) with PC3 fixed. The green trace is an intermediate state. (c). Laser spectrum when lasing on fast (blue) or slow axis (orange), respectively.

A broad range spectrum was recorded to study the ASE suppression and pump absorption (Figure 3.17(a)) from 1900 nm to 2300 nm with a resolution of 2 nm at four pump power levels – from the 400 mW to maximum pump power of 2.3 W. When FLM was optimized to have the maximum output power, an ASE suppression of more than 70 dB was measured at the maximum pump power of 2.3 W. The peaks were measured at approximately 2100.4 nm and 2100.9 nm, for fast and slow axis, respectively. Compared to the measurement at low power of FBG wavelength, the small drift from the initial central wavelength is a result of thermal expansion when the FBG is heated up by laser. This expansion redshifts the FBG center wavelength on both axes, with the same amount, as was measured here. Naturally, we would expect a stronger red-shift if the laser output power further increases. We were limited by the resolution of our OSA for estimation of the laser linewidth. An upper boundary of 0.06nm can be found as seen in Fig. 3.17(b), for lasing on both axes. To check the laser polarization property of dual-wavelength operation, inline PC1 and 2 were then tuned to achieve roughly equal power on both axes. The two lasing wavelengths are expected to be perpendicular to each other. The longer lasing wavelength was maximized on PD1 after the polarization beam splitter (PBS) by tuning the PC3 and then recorded by OSA. Then, keeping the PC3 unchanged, the spectrum of the other PBS output was immediately recorded. A

DOP of more than 99.999% can be clearly observed in Fig. 3.17(c) for both lasing axes, showing that a good orthogonality between the two lasing wavelengths is preserved.

Laser slope efficiency was then checked by inserting the laser output directly into an integrating sphere sensor. Lasing threshold was found to be 590 mW and slope efficiency is approximately 30% for the slow axis (Figure 3.18); Single-wavelength lasing on either axis was found to have the same slope efficiency and threshold while dual-wavelength lasing has ~ 0.2 dB lower efficiency. The laser threshold is 577.3 mW in terms of the output power of 1950 nm pump laser. Maximum output power of 480mW was reached, limited by the power of our pump laser. No indication of saturation is observed. Due to the mode field mismatch between the Nufern PM 1950 fiber and the Thorlabs SM2000 fiber, we measured approximately 1.5 dB input loss for the 1950 nm pump laser. Using an infrared thermometer, the mating sleeve temperature rises from 23 to 33 degrees during operation. Thus, the actual pump power coupled into the Ho-doped fiber laser cavity is smaller than the output power of the pump laser by 1.5 dB. We also plot the slope efficiency of this laser with respect to the coupled pump power. Under this condition, the slope efficiency reaches 44 % and the laser threshold drops to 381 mW.

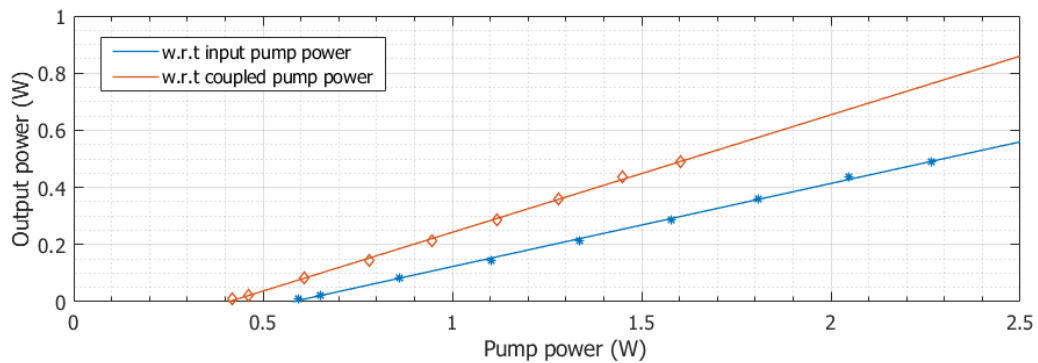


Figure 3.18. The 2100.9 nm output power with respect to 1950nm pump laser. By splicing all in-cavity components, the slope efficiency can be even higher. The 2.1 μ m output power is limited by the pump laser power; no output saturation is noticed during our measurement.

PC1 was tuned to select to lase on fast or slow axis and PC2 was tuned to maximize the output power. As FLM is a polarization sensitive element, PC2 also helps to enhance the degree of polarization (POD). The long-term spectrum/linewidth stability was then monitor on the OSA and power meters. In Fig. 3.19(a) and (b), a superposition of the laser linewidth over about 2.5 hours was plotted using more than 2000 recorded trace at a resolution of 0.05nm. The linewidth jitter does not exceed 12 pm both for single- and dual-wavelength operation regimes. The technique for the linewidth jitter

evaluation is stated elsewhere [107]. Stability of the dual wavelength lasing condition was then monitored for ~40min with 1000 traces shown in Fig. 3.19(c).

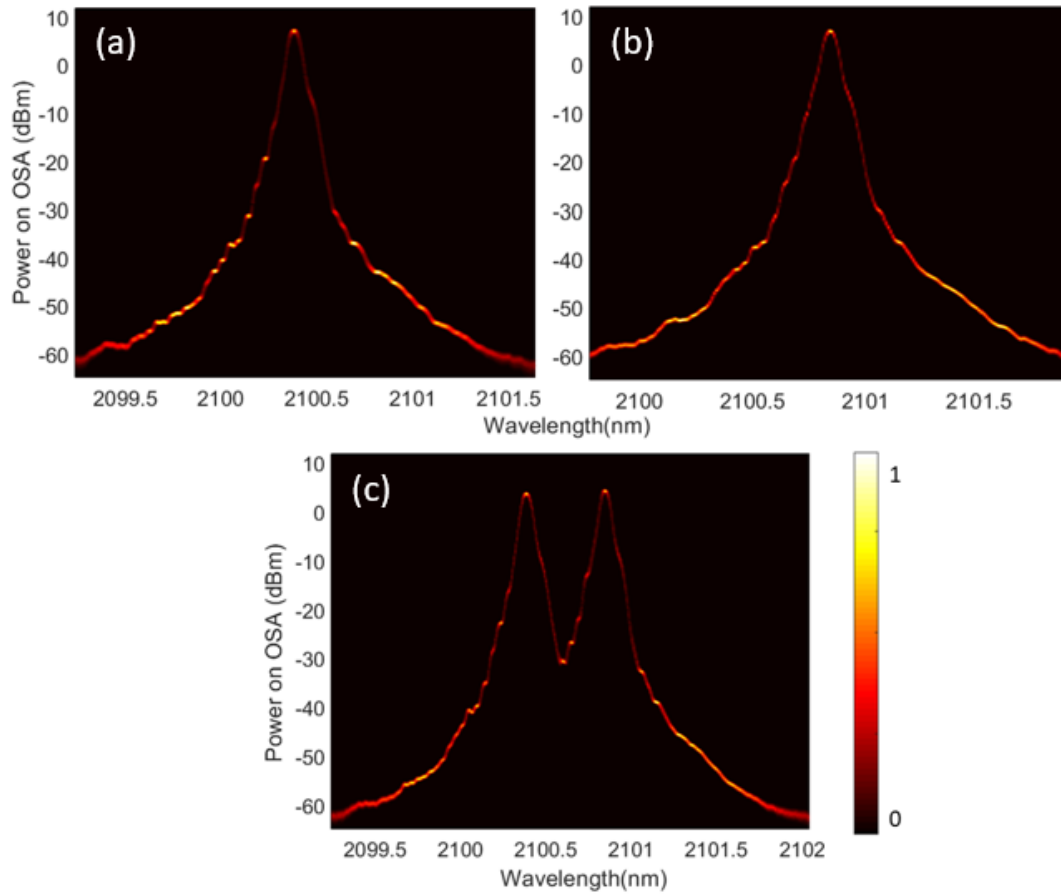


Figure 3.19. The laser line stability over time for all three operation categories. (a). Laser line distribution when lasing at fast axis; (b) Laser line distribution when lasing at slow axis; (d) laser distribution of dual-wavelength lasing. All data were recorded after 30 min of heating-up. The color bar (range from 0 to 1) corresponds to the probability of recording the laser line on a certain pump power and wavelength coordinate

The power stability of single wavelength lasing and dual wavelength lasing were also recorded with power meter as demonstrated in Fig. 3.20(a) and (b). The monitoring time for dual wavelength lasing and single wavelength lasing was 40 min and 120 min, respectively. Limited by the sensitivity of our integrating sphere sensor, the DOP can only be estimated to a lower boundary of 45dB. During single wavelength operation, the laser exhibits a good stability in terms of both power and polarization. For dual wavelengths operation, optical power at the cavity output on both polarization axes is equally distributed.

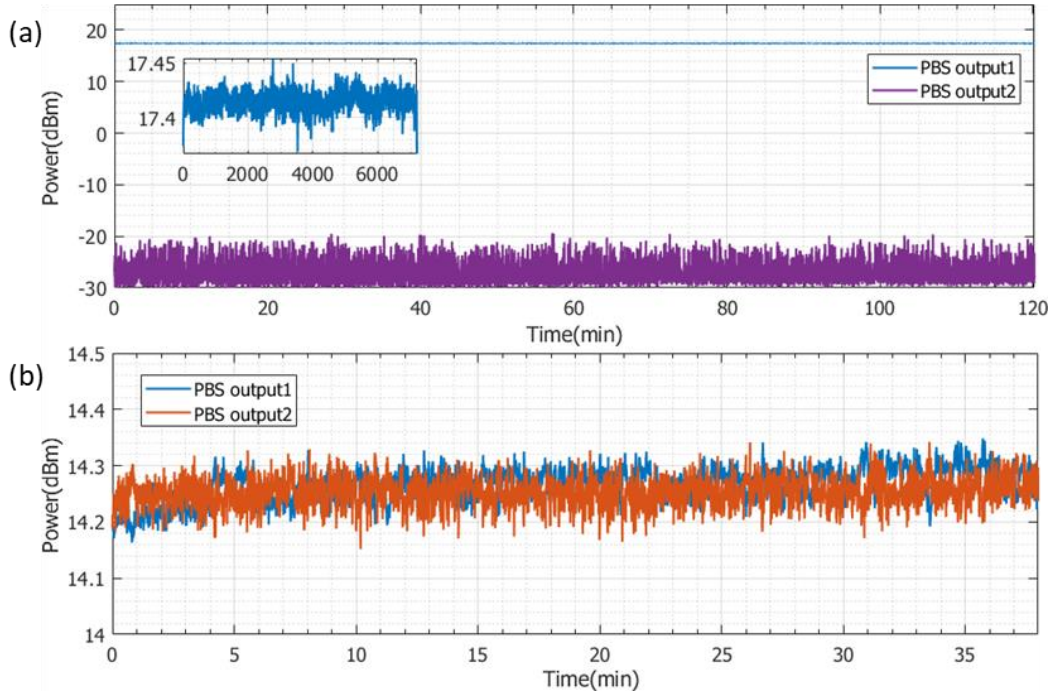


Figure 3.20. The laser stability when operating in single wavelength mode and dual wavelength mode. (a) Power meter readings for dual-wavelength lasing corresponding to Fig 4(d); (b). Power and polarization stability when lasing on single axis. Data recorded after 30min of heating up.

In the end, the laser efficiency was degraded by the loss between connectors. The highest connection loss comes from the mode field mismatch and Fresnel reflection between SMF-28 and PM 1950, which is around 1 dB. Splicing all cavity components is an effortless way to increase the slope efficiency, but also to enhance the high-power stability of the laser. Also, PM-FBG with higher reflection can be implemented. This laser is a promising light source for LIDAR and new telecommunication window.

Conclusion

In this chapter, we reviewed the configurations and performance of all our fiber laser cavities used in this project. By using properly designed cavities and active fiber lengths, we managed to cover until 2.1 μm for both pump and signal lasers. Thanks to the homemade fiber lasers, we can adjust the laser working parameters based on our experiment purpose and sample condition.

Chapter 4

Selection of fiber material and geometry

4.1 Introduction

With the 2 μm homemade fiber lasers, we can now move onto fiber design and characterizations. At the beginning of this project (year 2015), there are already a number of MIR fibers with various materials and geometries. Take tellurite and fluoride (including ZBLAN) glasses as an example. Though their transmission window does not extend as far as ChG in MIR, they can be good fiber material for MIR operation within 5 μm band. Both tellurite and fluoride glasses have low dispersion, hence releasing the requirements for dispersion engineering. Meanwhile, crystal fibers are becoming more interesting and practical in recent years. They have a lower theoretical loss, strong nonlinearity and significantly higher melting point. Besides, researchers are also trying to combine Tellurite and ChG soft glasses as another degree of freedom for dispersion engineering. There are also efforts made into combination of glass and crystal materials to ease the fabrication of crystal core fibers.

Figure 4.1 shows a list of current MIR fibers, categorised by their geometry and material types. It is worth mentioning that most of the mentioned fibers in Fig. 4.1 are research fibers – an indication of the active research in MIR fiber photonics – and that many parameters and characteristics have not been measured, hence not fully known. Only ChG step index fiber, ChG PCF and ZBLAN/fluoride step index fibers are commercially available. Note that this is not an exhaustive list – the figure only takes one fiber for each type. Even for the same fiber type, say ChG PCF in Fig. 4.1(g), there

are always multiple ChG fiber candidates. With such abundance of options, it is crucial to understand the state-of-art technology and challenges for all the MIR fibers.

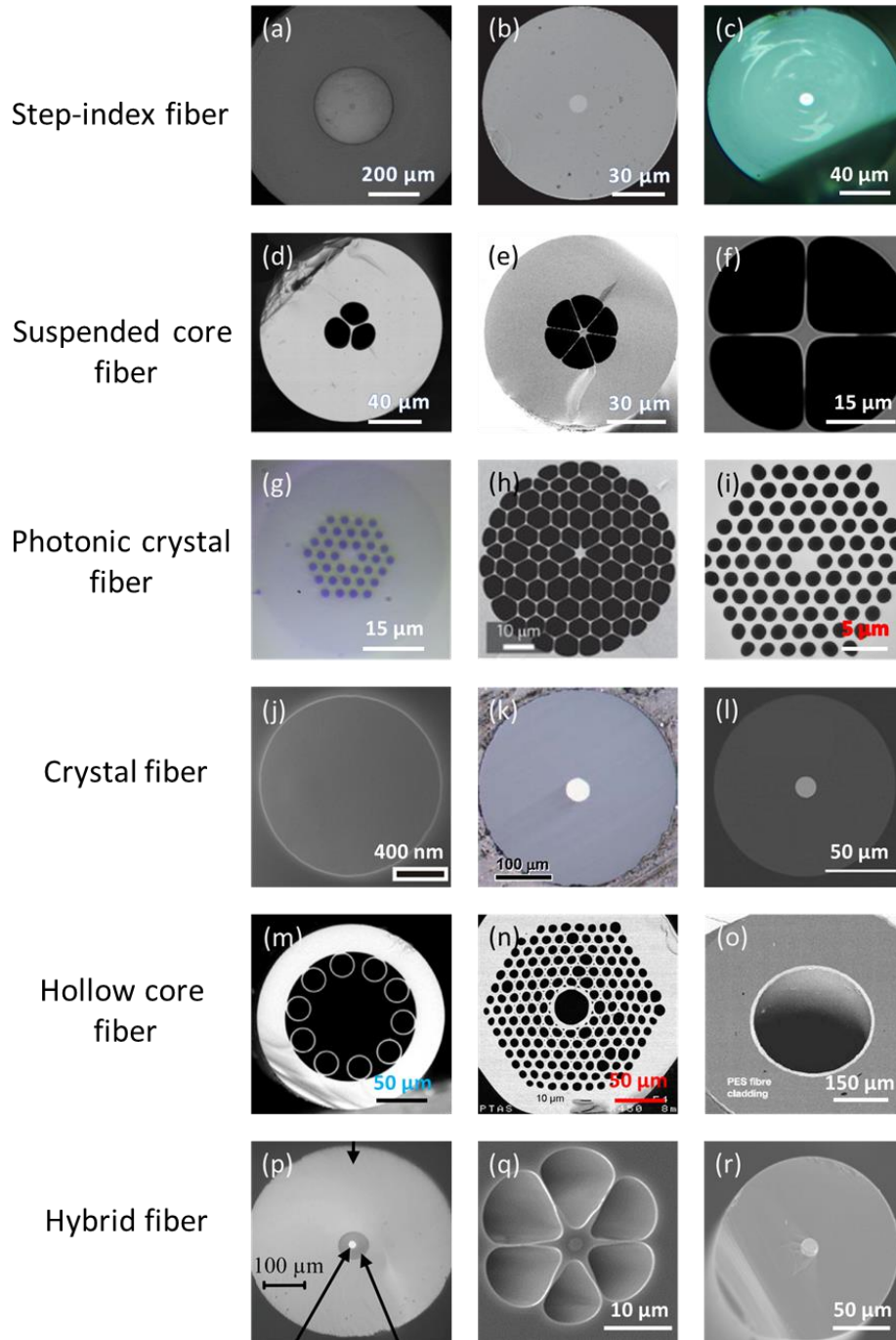


Figure 4.1. An overview of various MIR fibers. Step index fibers [108-110]: ChG (a), ZBLAN (b) and tellurite (c). Suspended core fiber [111-113]: (d) AsS ChG SCF; (e) Heavy metal oxides SCF; (f) Tellurite SCF. Photonic crystal fibers [114, 115]: (g) GeAsSe PCF; (h) ZBLAN PCF; (i) tellurite PCF. Crystalline fibers [116-118]: (j) silicon fiber; (k) sapphire fiber; (l) ZnSe fiber. Hollow core fibers [119-121]: (m) negative curvature fiber; (n) ChG photonic bandgap fiber; (o) omni-reflection/Bragg fiber. Hybrid fiber [77, 122, 123]: (p) AsS-CYTOP fiber; (q) AsS-tellurite fiber; (r) silicon-silica fiber. The figures are adopted with permission from publishers.

As a starting point, we compare ChG, tellurite, fluoride and crystal materials as material for the fiber preform. It is not possible to find a material that outperforms all the others in every aspect. We must make trade-offs based on the material's optical properties, the state-of-art fabrication technology and the market availability. Based on the comparison, we explain the reason for selection of ChG fiber as the material for our nonlinear platform. As mentioned before, there are multiple ChGs available for fiber fabrication. Hence, we make a short review of AsS, AsSe and GeAsSe ChG fiber using previous literatures to explain the use of GeAsSe glass in this project.

With the advance of fiber drawing technology, we now have multiple options for fiber geometry with GeAsSe ChG. The conventional step-index ChG fiber can leverage tapering and polymer cladding for dispersion engineering. Both SCF and PCF geometries are feasible options for microstructured GeAsSe fiber. We compare the performance and potential of step-index and microstructured ChG fibers. The final decision is made based on the possibility of dispersion engineering, linear loss, nonlinear parameter, fiber damage threshold, fiber chemical stability, coupling stability and fiber availability. The FOM, explained in Eqn. (2.28) to (2.30), can provide a more quantitative comparison of the structures. For a more complete view, we would also include several other MIR nonlinear waveguide platforms in this final comparison.

In the last sections of this chapter, we show experimental results on both SCF and PCF using low power FWM characterizations. Since ChG fibers are known for difficulties in handling, we will also describe the fiber preparation technique and compare different methods for preparation of fiber facets. At last, we specify the ChG PCF geometry and material for distant conversion into the MIR.

4.2 Material selection

4.2.1 Comparison of MIR fiber material options

Unlike ordinary MIR fibers, the fiber platform for nonlinear parametric conversion requires not only low propagation loss, but also high nonlinear parameter and good fiber uniformity. From Eqn. (2.9), a high nonlinear parameter comes from stronger mode confinement, hence higher optical power intensity. A small mode area leads however to two significant drawbacks. First, the fiber mode area increases at long wavelength, leading to high propagation. Second, high intra-core optical power intensity could lead to purely thermal damage or fiber fuse (optical discharge). To avoid such damages, the fiber needs to have a relatively high glass transition temperature (T_G) and, more importantly, low absorption of laser power.

Table 4.1 MIR fiber glass properties.

Material	n at 2 μm	$n_2/n_{2,\text{silica}}$ ⁽³⁾	ZDW (μm)	Transparency ^(4s) (μm)	T_G ($^\circ\text{C}$)
Fused silica [124]	1.43	1	1.26	0.2 – 2.6	1200
ZBLAN [125] ⁽¹⁾	1.51	0.85 – 1.2	~1.71	0.35 – 7	260
Tellurite [126] ⁽²⁾	2	~25	~1.9 – 2.1	0.4 – 5	240 – 400
As ₂ S ₃ [127, 128]	2.43	122	4.9	0.6 – 12	180 – 190
As ₂ Se ₃ [129, 130]	2.79	500	7.5	1 – 16	165 – 171
Ge ₁₀ As ₂₂ Se ₆₈ [67, 79]	2.63	215	7	>1 – 11 ⁽⁵⁾	~175

^(1,2) The exact nonlinear refractive indices of ZBLAN and tellurite glasses depend on the glasses' composition. Here, we put the generally accepted values.

⁽³⁾ The nonlinear refractive index of fused silica is $n_2 = 2.73 \times 10^{-20} \text{ m}^2/\text{W}$

⁽⁴⁾ This is the bandwidth when glass transparency drops by 50% from maximum values

⁽⁵⁾ Limited by data availability, we place the transparency of a microstructured GeAsSe fiber.

The GeAsSe glass has better transmission window than AsS at longer wavelength side.

In Table 4.1, we list the major soft glass candidates for fabrication of MIR fibers. We also include fused silica in the first row as a reference material. Once drawn into fibers, the glass transition window narrows due to defective bonds induced during the drawing process [69]. For this project, the fiber must have good transmission from 1.5 to at least 4 μm . All soft glasses in Table 4.1 satisfies the requirement for the telecom band laser. However, the long wavelength coverage is insufficient for most ZBLAN [131] or fluoride fibers [46]. On the other hand, tellurite [126] (including fluorotellurite [132]) fibers typically support low loss transmission slightly more than 5 μm . As early as 2010, highly purified ChG microstructured fibers achieved less than 50 dB/km transmission loss at 3.7 μm [133].

In terms of material nonlinearity, –Se and –S based ChGs [134] and tellurite glass [113] have ultrahigh nonlinear refractive index n_2 and good viscosity. The fluoride fibers, including ZBLAN, have a nonlinear refractive index close to that of silica [125]. From Table 4.1, we expect an easy dispersion engineering effort to shift ZDW of fluoride fibers to telecommunication laser band. However, this small n_2 requires larger fiber length and higher pump power for efficient FWM. For the matured silica HNLF, the fluctuations of fiber core size vary the phase matching condition along the fiber [135]. Unavoidably, the same problem will occur for ZBLAN fibers. One solution is to use very short fiber length, hence less core size fluctuations. In this case, the material must be highly nonlinear for efficient FWM under CW pump.

Under this condition, we hold a tendency towards either ChG or tellurides fibers. Since the bulk soft glass all have low loss in 4 μm range (Table 4.1), the propagation loss α of fiber is mainly dependent maturity of fabrication technique (purification, fiber drawing parameters, preform smoothness, etc.). In addition, the slope of ChG viscosity is very similar to that of silica fiber [69]. This could be one reason behind the extremely low loss of ChG microstructured fibers in several previous papers [111, 136–138]. Among all soft glass fibers, only fluoride/ZBLAN fiber has reported a similar small loss [69]. The first experiment with tapered ChG PCF appeared in 2012, with a nonlinear parameter of $11 (\text{W}\cdot\text{m})^{-1}$ and waist length of 1 m [139]. Due to an inherently much lower nonlinear refractive index of tellurite glass, one would need either a three times smaller core or nine times longer fiber to reach comparable performance as ChG fibers. Unfortunately, small fiber core leads to higher confinement loss and long fiber length increases the chance of core fluctuations. Unlike ChG PCFs, tellurite PCFs still suffer from high propagation loss of 4.2 dB/m at 2 μm [115] and the actual loss in MIR band could even be higher than reported [140]. Indeed, we did not see further nonlinear optical experiments on this PCF. Therefore, we believe tellurite fibers are not yet at the same level of maturity as ChG fibers.

Crystal fibers could be an ideal nonlinear platform in the future, once the fabrication techniques become more mature. The crystal ZnSe and sapphire can be made into a fiber with proper technique [117, 125, 141]. The sapphire crystal has good transmission until 5 μm [142]. The ZnSe crystal has a huge transmission window from 0.5 to 22 μm [118] and has already been used as a commercial MIR laser crystal. However, the ZnSe fiber propagation loss is still in orders of dB/cm, which mainly comes from scattering loss [69]. Efforts have been made into increasing of interface smoothness on Sapphire fibers leading to a loss below 0.1 dB/cm [117]. There are also explorations on combination of glass cladding with crystalline core to achieve small

fiber core size and long length [123]. However, these fibers still have high loss (likely more than several dB/m). Due to the big difference of refractive index between core and cladding, they are expected to be highly multimode. In addition, the low viscosity of crystals prevents any use of conventional fiber drawing techniques, hence requiring development of new fabrication methodologies. At this point, the freedom of dispersion engineering for crystalline fibers is highly limited, if not impossible. Thus, we conclude that crystalline MIR fibers are still in the early stage of development and not a suitable candidate for our project.

The negative curvature fibers [Fig. 4.1(m)] also have good transmission window. Silica negative curvature fibers can transmit from UV to MIR, thanks to the small mode overlap with the fiber material [143]. In negative curvature fibers, the MIR fiber lasers beyond 3 μm are already demonstrated utilizing gas excitation [144] or gas Raman shift [145]. The dispersion of such fibers can be tuned by changing the gas pressure [143]. However, due to the low nonlinearity of gas, these fibers are more suitable for high peak power ultrafast applications, especially few-cycle pulse generation [146-148]. It is impossible to expect a gas to have higher nonlinearity than solid state materials. Hence, we also exclude such fibers from our platform candidates.

4.2.2 Selection of ChG glasses

In the category of ChG glass, AsS, AsSe and GeAsSe are the three main candidates for fiber fabrication. Fabrication of tapered step index fibers, SCFs and PCFs have been reported with all three ChGs [61, 138, 139]. In terms of optical properties, AsS has the lowest ZDW while AsSe holds the largest nonlinear refractive index, as shown in Table 4.1. With a higher glass transition temperature, one can expect better power handling from an AsS platform. However, the higher nonlinearity of the AsSe platform implies less power is required for the same nonlinear parametric CE as AsS platform. In general, GeAsSe ChG has material properties lying between those of AsSe and AsS. Since none of the ChG materials is perfect, we must make proper trade-offs to find the best material for this project.

Compared with AsSe, GeAsSe has slightly less material dispersion. In addition, GeAsSe has a higher melting point and larger bandgap [79, 84], hence an expected better handling of optical power. More importantly, GeAsSe allows tapering of a PCF structure to small core size over long length while keeping high smoothness and low loss [139]. Compared with AsS, the GeAsSe glass holds larger nonlinearity and better environment stability [79]. Though AsS is very attractive due to its low dispersion, the fast environment degradation of microstructured AsS fibers prohibits at this point any

further development. Indeed, we did not see any further progress of AsS PCFs after its first appearance almost ten years ago [149]. AsS SCF suffers heavily due to surface degradation due to water absorption [75]. Thus, we believe GeAsSe is the optimal solution for the moment, providing a long aging time [79] and the best freedom for dispersion engineering. It is worth mentioning that investigation and optimization of the exact composition of GeAsSe (Table 4.2) glass will allow for further improvements of GeAsSe PCFs.

Table 4.2. Optical and thermal properties of GeAsSe with various composition [84]

Material	Bandgap (nm) $\pm 4\%$	$n_2(\times 10^{-18} \text{ m}^2/\text{W})$ $\pm 25\%$	T_G ($^{\circ}\text{C}$)
Ge ₃₅ As ₁₅ Se ₅₀	639	24.6	380
Ge ₃₃ As ₁₂ Se ₅₅	600	15	362
Ge ₂₂ As ₂₀ Se ₅₈	614	9.2	292
Ge ₂₅ As ₁₀ Se ₆₅	585	6	305

It is important to mention that there used to be concerns regarding CW operation with ChG mainly due to questioning of their power handling capability. Thanks to the advances in fabrication, the damage threshold was found to be higher than 5.6kW/cm² when pumped with a Tm-doped fiber laser at 1.97 μm and the overall fiber temperature has seen about ten degree increase [150]. Higher pump power was not tested only due to the limit of the authors' pump laser power. These finding were then confirmed by us and other researchers with even higher values for both AsS and GeAsSe ChGs [66, 108]. More importantly, low loss and robust splicing between ChG and silica fiber was demonstrated with a splicing loss of 0.5 dB at 2 μm range [150]. From Table 4.2, it is also possible to further vary the composition of GeAsSe glass for a higher melting temperature, hence a better power handling capability. Integration of a ChG fiber with silica fiber laser now becomes feasible. Splicing with silica fiber not only allows for all-fiber systems, but also closes the air holes of PCFs thus limiting water absorption for longer lifetime.

4.3 Geometry and preparation of ChG fiber facet

4.3.1 ChG fiber geometries

In 2007, the first ChG fiber taper was fabricated in order to further enhance its nonlinearity [151]. The tapering process not only reduces the mode effective area, but also enhances the waveguide dispersion. Using a proper cladding material, such as polymer or air, it is possible to shift the ZDW of ChG taper even to C-band wavelength, which allows efficient and broad parametric amplification under a ns pulse pump [152]. To avoid the TPA and reduce the fabrication difficulties, it proves to be useful to pump the tapered ChG fibers in the 2 μm band. It was later found that the use of PMMA polymer limits the use of ChG tapers in MIR due to PMMA's strong absorption [78]. Thus, a large linear loss was measured [78], which strongly pulls down the FOM of this fiber. In 2016, researchers found that another polymer, CYTOP, has a good transmission in MIR (Fig. 4.3) and the right viscosity for making a ChG taper [77]. Using such tapers, ChG tapers based OPO and broadband wavelength converters were demonstrated with 2 μm pulsed pump [61]. However, such fibers still have a relatively high loss at 0.5 dB/cm at the 2 μm wavelength band [61]. This is mainly due to the viscosity difference between the ChG and CYTOP polymer which leads to strong surface scattering [77]. Under this condition, the fiber performance under high intensity CW pump power is doubtable. In addition, longer tapers are yet to be demonstrated and are essential to lower the required pump power for efficient nonlinear conversion. Therefore, it is preferable to use a fiber fully fabricated from the one or very similar material.

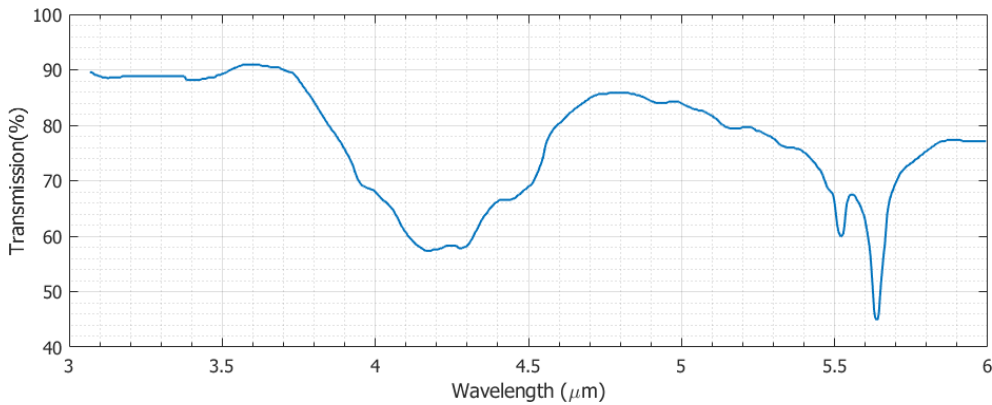


Figure 4.2. Transmission of a 0.1 mm thick CYTOP in the MIR band. The first absorption peak comes from CF_2 bond and the second comes from the COOH bond. Data from [153].

Low loss ChG PCFs and SCFs were developed in recent years [133]. For ChG SCFs, including the “grape fruit” structure, the cladding is effectively air, leading to a refractive index difference of 1.4 to 1.8. Thus, ChG SCFs are highly multi-mode

(numerical aperture > 2.4) at the core size range of $\sim 1 \mu\text{m}$ and remains to be a problem to be solved [138]. From the light guiding mechanism, the SCFs are the same as the ChG tapers, except from using air as their cladding. Though termed as microstructured fibers, the SCFs only have one degree of freedom for dispersion engineering same as step-index fibers. In addition, having the direct air contact of the core results in water absorption on the ChG surface and degrades surface smoothness, which increases propagation loss and harms nonlinear optical performance [75].

Unlike the SCF or step-index fibers, the ChG PCFs can provide additional degrees of freedom for dispersion engineering. By changing the hole-pitch ratio, the waveguide dispersion can be alternated. Thanks to the modified total internal reflection, the ChG PCF can be operated in single mode region starting at $1.5 \mu\text{m}$ [67]. As early as 2012, researchers have demonstrated FWM using tapered ChG PCF, where the PCF structure is well maintained. The purpose of tapering in that work [139] was solely to enhance the fiber nonlinearity. Naturally, one can also use the tapering for dispersion engineering of the ChG PCF.

Table 4.3 FOM of various nonlinear waveguides

	SMF-28	Silica HNLF	Si waveguide	As ₂ S ₃ waveguide	As ₂ Se ₃ taper	Tellurite SCF	GeAsSe PCF	GeAsSe T-PCF
	[124, 154]	[155]	[156]	[128]	[157, 158]	[113]	[67]	[66]
$n_2 \cdot 10^{-20}$ (m ² /W)	2.7	2.7	1100	300	1100	59	530	530
$n_2/\alpha \cdot 10^{-19}$ (m ³ /W)	58	16	1.9	2.6	16	86	230	100
FOM (W ⁻¹)	0.19	0.14	1.89	0.85	3.44	2.41	7.31	85.05

Design of a waveguide based optical parametric converter at MIR should take three factors into consideration: material, geometry and feasibility of fiber fabrications. There are, of course, some trade-off among those parameters and we use FOM as the design reference, which provides a quick estimation of nonlinear platform performance. The derivation of FOM is based on the coupled-wave equation under the assumption of no pump depletion as described in chapter 2. The design rule is straightforward – maximize nonlinear parameter γ and minimize propagation loss α . Here, α is dependent on the loss resulted from scattering, absorption, fabrication imperfection and surface

smoothness. Thus, the FOM can provide a good estimation of the fiber nonlinearity and fabrication maturity. For better comparison, we compute the FOM of our ChG tapered PCF together with other nonlinear waveguide platforms in Table 4.3. With a much higher FOM, we can expect highly efficiency FWM processes using ChG PCF taper.

4.3.2 ChG facet preparation for coupling

Since ChG is a type of soft glass, very few cleavers are available to make a good cleaving facet. Flat cleaving facet of ChG PCFs can be achieved using the York ultrasonic cleaver and Vytran cleaver. When inspecting the facet, the light absorption on the input facet must be reduced to minimum. Otherwise, the high reflection from the ChG facet would easily saturate the camera and hide the defects. An optical microscope can normally provide enough resolution for ChG fiber facet inspections. Comparing the facet quality of Fig. 4.3(a) and (b), the York ultrasonic cleaver cannot provide a good facet quality, even though we have adjusted the tension rigorously.

Table 4.4 Polishing disk number and smoothness

Disk number	1	2	3	4	5
Roughness	3 μm	1 μm	0.5 μm	0.3 μm	NA

Another method to get a smooth facet is polishing. I modified the standard Krell polishing setup for bare fiber polishing. With proper arrangement of polishing disks and careful control of fiber holder pressure, highly smooth surface can be polished. Our experimental measurements indicate that the polished facet has the same loss as the cleaved facet obtained with the by Vytran. From the microscope photos in Fig.4.5 (c) and (d), the smoothness is ultrahigh. With a high quality polished ChG facet, one can fuse splice the ChG fiber with silica fiber using the same technique as [70]. There are small grains of ChG inside the air holes. We did not notice any thermal damage nor extra coupling loss due to the ChG grains. In addition, for the 4 μm core sized GeAsSe PCF, the small air holes prevent the entrance of ChG grains during polishing.

When cleaving our new GeAsSe PCF with Vytran cleaver, however, the cleaving repeatability is very low. Most of the time, even the lowest tension setting breaks the GeAsSe PCF. The reason of this failure is not yet clear. Polishing, on the other hand, leads highly repeatable results and very low coupling losses. In addition, we can also make angled PCF facets at Brewster's angle to further reduce coupling loss. A small polishing angle can also avoid back-reflection into the pump laser, which is not achievable by normal cleaving method for soft glass fibers. We show the list of

polishing disks in Table 4.4 in the order of usage. For fine polishing, it is recommended to add 80% alcohol onto the disks.

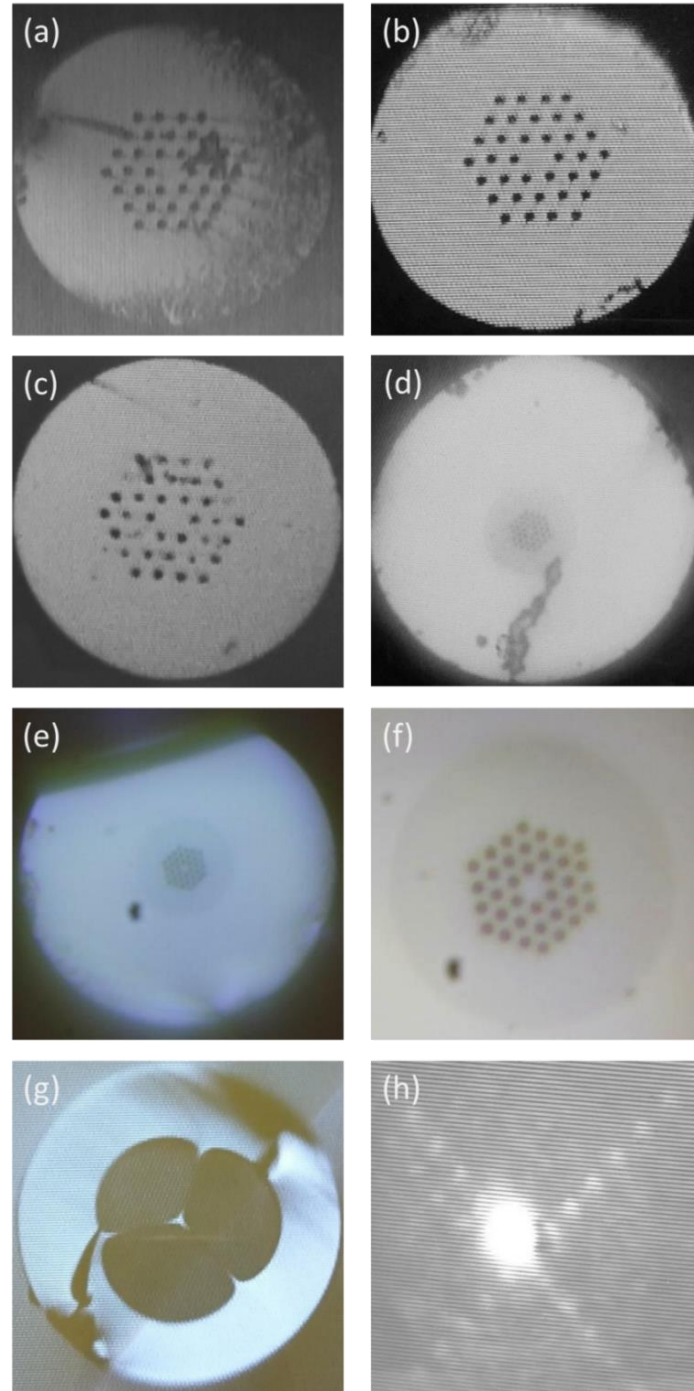


Figure 4.3. Comparison of facets from different cleaving methods. (a) AsSe PCF cleaved by ultrasonic cleaver. (b) AsSe PCF cleaved by Vytran cleaver. (c) AsSe PCF after polishing. (d) GeAsSe PCF after polishing. (e) manually prepared GeAsSe tapered PCF. (f) Manually cleaved GeAsSe PCF; (g) Manually cleaved AsS SCF; (h) Far-field image from IR camera at fiber output after sending telecom band laser, indicating proper core coupling.

However, preparation of a good polishing facet is time consuming. Moreover, polishing does not allow for mm fiber length, which as we will see, is critical for the study of ANDi SCG. Therefore, we have also developed the proper manual/hand cleaving method using a Ruby blade from Thorlabs. Fig. 4.3(e) to (g) show the manually prepared facets of a 1.5 μm core GeAsSe tapered PCF, 4 μm core GeAsSe PCF, 3 μm core AsS SCF, respectively. The coupling tests indicate same coupling loss as polished fiber facets. The defect on the cleaving starting point does not degrade the coupling if the fiber core is smooth and without defect. At the output side, we inspect with an IR camera using low power 1.5 μm laser to ensure core coupling [Fig. 4.3 (h)]

4.4 Experimental results

In this section, we compare the performance of PCF and SCF fiber geometries. In addition, this series of experiment enables us to check the uniformity of our samples, to extract nonlinear refractive index and to confirm our simulation results. We performed the test with AsS SCF instead of AsSe or GeAsSe SCF due to the limited fiber availability. Since As-S bond is stronger than the As-Se bond, the AsS SCFs have a better mechanical stability than the AsSe SCFs. Therefore, any mechanical stability issues happening for AsS SCFs are also expected to occur for (Ge)AsSe SCFs with similar (or smaller) core sizes.

4.4.1 AsSe Photonic crystal fibers

We tested an $\text{As}_{38}\text{Se}_{62}$ PCF with a length of 31.5 cm, provided by PERFOS. The core diameter is 14 μm while the external diameter is 125 μm . From an SEM image, the air hole diameter d and the pitch distance Λ are measured to be about 3.79 μm and 8.54 μm , respectively, leading to a ratio of 0.44 between air hole diameter and pitch distance. From our COMSOL simulations using “Wave optics” module, the fiber shows a single mode behavior for wavelength beyond 1.3 μm . The refractive index at different wavelengths is provided by the manufacturer. Using interpolation, we simulated the dispersion of this fiber from 1.5 μm to 6 μm as showed in Fig. 4.4. Due to the large core size compared to the operational wavelength, the dispersion is expected to be mostly dominated by material dispersion. The simulated ZDW is 5.1 μm , which is in accordance with expectation.

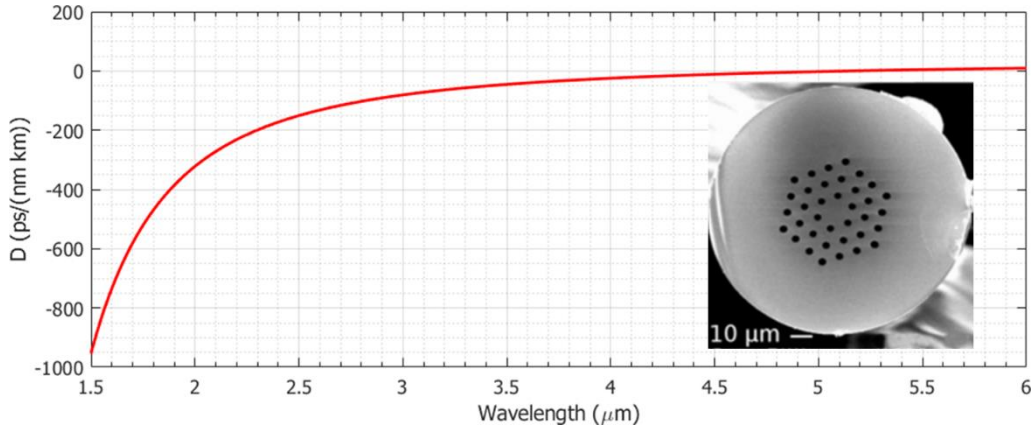


Figure 4.4. Dispersion parameter as a function of the wavelength. Inset: SEM image of the cross section of the AsSe PCF.

The set-up follows the same principle of Fig. 3.1. The pump was fixed at 1980.6 nm and we tuned the signal laser wavelength and recorded the FWM spectrum on the OSA. We collect the output of the AsSe ChG PCF using a multimode fluoride fiber. The total coupling loss is about 11 dB. Fig.4.5 shows the superimposed optical spectra by sweeping the signal laser on the blue side of the pump, where pump power is 54 mW and signal power is about 6 mW. Multiple periods of oscillations in the idler generation are observed in Fig.4.5 for a relatively small wavelength detuning due to the high dispersion ($699 \text{ ps}^2/\text{km}$) of the fiber at $2 \mu\text{m}$. It can be noticed that idlers are generated both on the signal and pump side. This is a combined effect of high fiber nonlinearity and high signal power, which allows the signal to act as a pump as well.

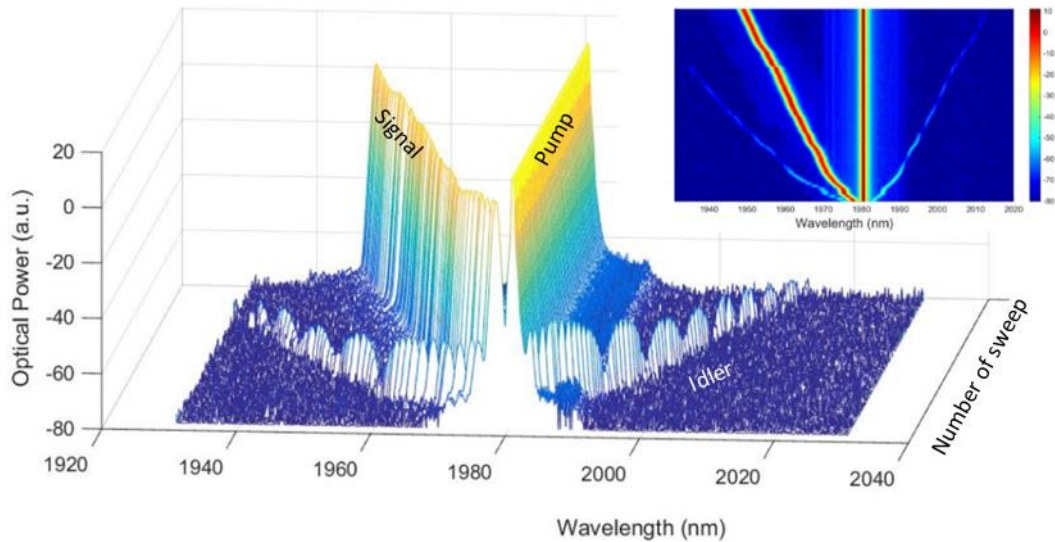


Figure 4.5. Superimposed FWM spectra of different signal laser positions with constant pump power. Pump wavelength at 1980 nm and swept signal wavelength starting from 1950 nm to 1978 nm. Maxima and minima in CE due to the phase matching condition are clearly visible. Inset: view from the top to view.

To confirm that the observed effect is indeed FWM, we first characterize the CE as a function of the pump power with a fixed signal detuning of 6 nm. A Tm-doped fiber amplifier (TDFA) was used to get measurements at high pump power. The linear loss was retrieved by a cutback experiment and estimated to be between 4.5 and 6 dB/m at 2 μm wavelength, which is slightly higher than the nominal one attributed to water absorption, aging and photodarkening. The CE as a function of the pump power follows the expected quadratic behavior (slope = 1.9), as it is shown in Fig. 4.6(a). Maximum CE of about -36 dB is achieved at 151 mW coupled pump power without any sign of saturation. When we vary the signal power keeping the pump power constant, we verified the linear dependence between idler and signal powers plotted in Fig. 4.6(b). The CE as a function of the wavelength for three different coupled pump powers is shown in Fig. 4.6(c). Idler waves are seen over a bandwidth of at least 25 nm with a 3 dB conversion bandwidth of about 18 nm considering both sides around the pump wavelength.

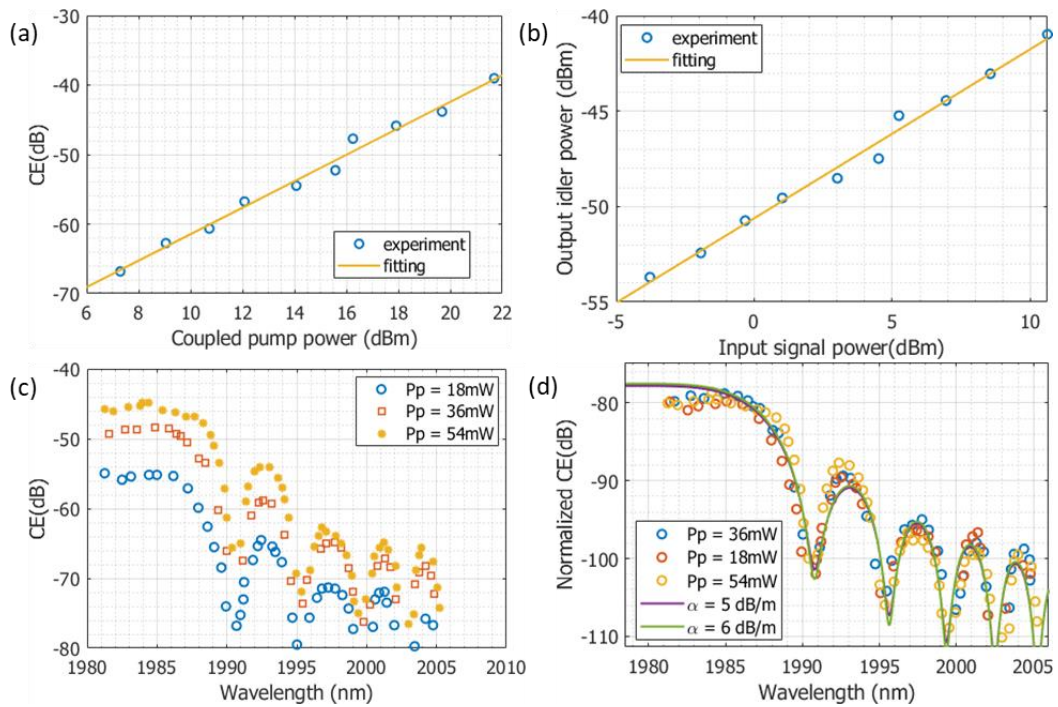


Figure 4.6. FWM results with the AsSe PCF. (a) Conversion efficiency (CE) as a function of coupled pump power in logarithm scale together with the theoretical fit of a quadratic polynomial. (b) Idler output power as a function of the signal input power. (c) CE as a function of the generated idler wavelength for three different coupled pump powers. (d) CE for three different coupled pump powers normalized to the pump power squared superimposed to the theoretical CE/P_p^2 plotted with different linear losses values.

As seen in Fig. 4.6(c), the conversion bandwidth does not change as a function of the pump power, hence the nonlinear phase mismatch can be safely neglected in calculation. In Fig. 4.6(d) we normalize the three curves to the coupled pump power squared to remove the influence of pump variation. The data was then fitted with the normalized CE to retrieve the dispersion parameter $D = -2\pi c\beta_2/\lambda^2$ and the nonlinear coefficient γ retrieved from the quadratic behavior. We used different fitting curves, with different α values ranging from 4.5 dB/m to 6 dB/m. The estimated dispersion is $D = -336 \text{ ps/nm/km}$, in perfect agreement with the numerical simulation ($D = -334 \text{ ps/nm/km}$) in Fig. 4.4. The nonlinear parameter is estimated to be $\gamma \approx 0.53 \text{ (Wm)}^{-1}$. Since the nonlinear refractive index n_2 is more universal, we calculated the nonlinear refractive index n_2 from the estimated γ and the mode effective area of the fiber obtained from COMSOL simulations resulting in $n_2 = \lambda A_{eff}\gamma/(2\pi) \approx 7.9 \cdot 10^{-13} \text{ cm}^2/\text{W}$. This value is indeed consistent with previous results found in literature at telecommunication wavelength obtained by SPM experiment: $n_2 \approx 1.1 \cdot 10^{-13} \text{ cm}^2/\text{W}$ [159] and by FWM with pulsed pump: $n_2 \approx 1.3 \cdot 10^{-13} \text{ cm}^2/\text{W}$ [138].

4.4.2 AsS Suspended core fibers

Due to the air cladding nature of this kind of fiber, the SCF structure has a large waveguide dispersion which can be engineered by varying the core size. Therefore, it is possible to shift the ZDW of AsSe SCFs even to the telecommunication wavelength band by tapering. There have already been several experiments utilizing dispersion engineered ChG SCF including supercontinuum generation and FWM with a tapered SCF as mentioned in previous section. To simulate the dispersion, we constructed the SCF structure using 3rd order Bezier curves as indicated in Fig. 4.7(a).

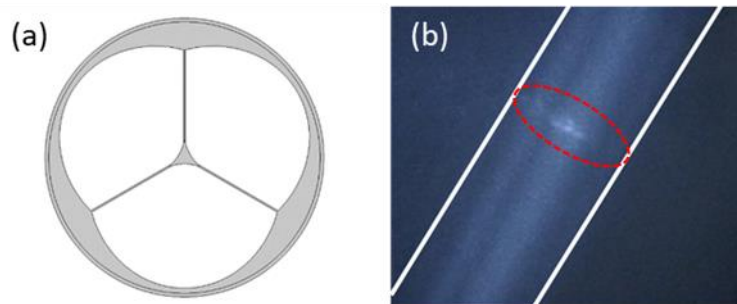


Figure 4.7. AsS SCF geometry and light leakage. (a) Geometric structure of SCF used for COMSOL simulation. (b) In the red circle: Observed light leakage from the SCF due to internal damage

Since the strut size is normally smaller than the operational wavelength, the SCF is effectively a triangular fiber with air cladding. In this thesis, the core size of SCF is

defined as the circle diameter that is tangential to the three Bezier curves. We have tested some As_2S_3 SCFs of different core sizes fabricated by Université de Bourgogne. We characterized several pieces of SCFs using CW FWM at both $1.55\ \mu\text{m}$ and $2\ \mu\text{m}$ band.

We started our experiment with the same setup as shown in Fig. 3.1. We used a pair of identical lensed fibers for in and out coupling. The most critical problems come from the mechanical strength of such fibers. Due to the extremely narrow strut (sub-micrometer) and fragility of soft glass, the struts can break easily. The build-in tension during the cooling process after fiber drawing releases when the fiber is straightened or bent in another direction. This small energy is strong enough to break the strut. The broken struts lead to sharp bending of the fiber core. Light is no longer guided with such strong bending and escape from the fiber as indicated by the photo taken from a top-view IR camera [Fig. 4.7(b)]. In addition, we noticed strong coupling fluctuations once the pump power exceeds 40 mW, due to the optical pressure. Due to the SCF geometry, the struts need relatively high deformation to compensate for the optical pressure and leads to misalignment. As a result, the coupled pump power is greatly limited for this fiber geometry.

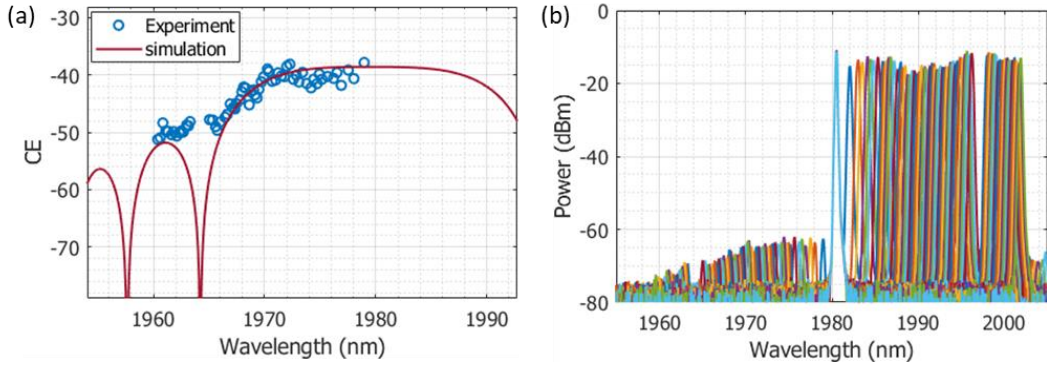


Figure 4.8. FWM result with the AsS SCF. (a) experimental retrieved CE superimposed with the simulated curve; (b) superimposed spectrum when sweeping the signal.

We conducted the $2\ \mu\text{m}$ FWM experiment on SCF with 20 mW pump power and 13 mW signal power. However, the experimental CE completely diverges from the simulations. From Fig. 4.8, no obvious oscillations of the CE can be observed. We did not observe the presence of dips after a complete sweeping of input polarization either. It is a combined result of the strong multimode nature of this fiber (1.4 difference in refractive index) and SCF core size variation. Given the strong confinement, the higher order modes can propagate with low loss. Under SEM, we noticed core variations of $\pm 0.2\ \mu\text{m}$, which leads to strong dispersion fluctuations along the fiber length.

Besides the abovementioned issues, splicing of SCF with silica fiber is yet to be demonstrated and the possibility remains unclear. Due to the chemical and mechanical instabilities, multimode behavior and core fluctuations, we believe ChG SCF is not a suitable platform for CW nonlinear parametric converters.

4.4.3 GeAsSe Photonic crystal fibers

We tested a new $\text{Ge}_{10}\text{As}_{22}\text{Se}_{68}$ PCF of 27.5 cm in length with core size of $4\text{ }\mu\text{m}$ and diameter-to-pitch ratio $r = 0.49$ fabricated by PERFOS. The GeAsSe has less material dispersion and slightly smaller nonlinear refractive index at the same time. Thanks to the smaller core size, the ZDW is shifted closer to $2\text{ }\mu\text{m}$ and the nonlinear parameter γ is expected to be comparable to our AsSe PCF. As mentioned in section 3.5, we used the Sellmeier equation from $\text{Ge}_{11.5}\text{As}_{24}\text{Se}_{64.5}$ for the dispersion simulation. From the COMSOL simulation, we estimated the ZDW at $\sim 3\text{ }\mu\text{m}$ (Fig. 4.9).

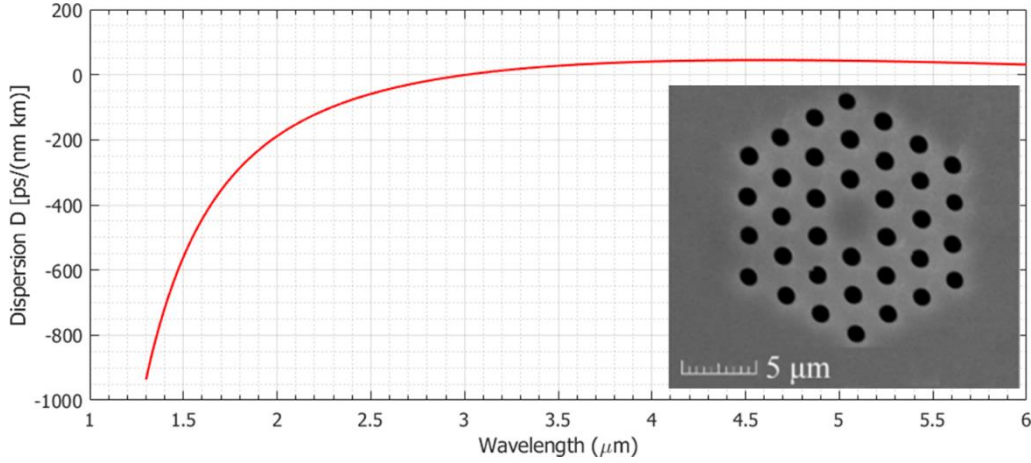


Figure 4.9. Dispersion parameter as a function of the wavelength.

We tested the fiber for three different pump wavelengths: 1565 nm, 1981 nm and 2008 nm, while the pump powers were measured to be: 36 mW, 65 mW and 60 mW respectively. Due to a high material absorption and potential two photon absorption (TPA), we used the lowest power at 1565 nm range. The average overall losses were about 4.5 dB, with an estimated 2.5 dB in-coupling losses, 1.5 dB out-coupling losses and 0.5 dB of propagation losses, i.e. $\alpha = 2\text{ dB/m}$. Fig.4.10 (a)-(c) show the CE as a function of the idler wavelength for the three employed pump wavelengths. The experimental data are superimposed with the theoretical simulated CE. It is noticed that the magnitude of the lowest experimental points has an upper bound given by the OSA noise floor. The dispersion parameters are estimated to be $D = -171\text{ ps/(nm km)}$ at 2008 nm, $D = -183\text{ ps/(nm km)}$ at 1980 nm, and $D = -477\text{ ps/(nm km)}$ for 1565 nm pump. As expected, the dispersion decreases (in absolute value) when the

pump wavelength approaches the ZDW, leading to a maximum overall 3 dB conversion bandwidth of 24 nm for the 2008 nm pump wavelength. The theoretical values, $D = -185 \text{ ps}/(\text{nm km})$, $D = -196 \text{ ps}/(\text{nm km})$ and $D = -480 \text{ ps}/(\text{nm km})$ at 2008 nm, 1980 nm and 1565 nm respectively, are larger (in absolute value) than the experimental ones. This could be explained by the slight difference in our glass composition which leads to a small difference in material dispersion.

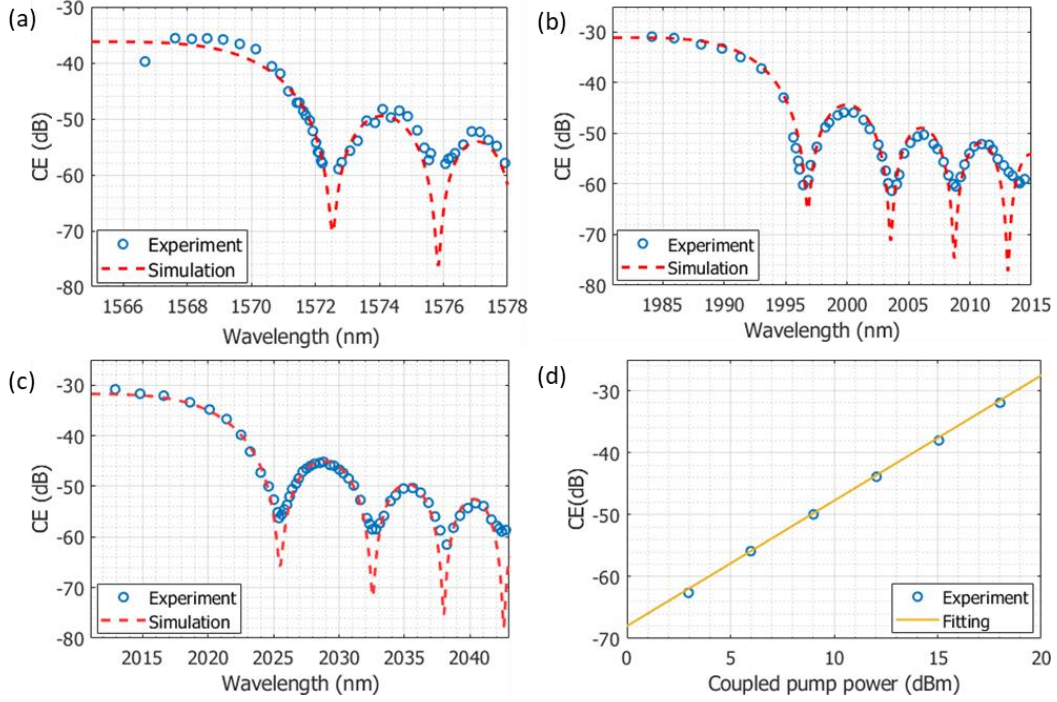


Figure 4.10. Experimental points superimposed to theoretical fits of the CE as a function of the idler wavelength for pump wavelength of (a) 1565 nm. (b) 1980 nm and (c) 2008 nm. (d) CE as a function of the coupled pump power for pump wavelength of 1980 nm and pump signal detuning of 6 nm.

In Fig. 4.10(d) is shown the CE as a function of the coupled pump power for the 1980 nm pump wavelength, and signal – pump detuning of 6 nm. The experimental data follow very well the expected quadratic dependence, notably there is no sign of saturation due to fiber damage or multiphoton absorption and the CE reaches -25.4 dB for a CW coupled pump power of about 20.5 dBm. Experimental data in Fig. 4.10(b) are fitted using the dispersion value retrieved from the experimental setting γ as the fitting parameter. The nonlinear parameter is thus found to be $1.68 \pm 0.11 \text{ W}^{-1}\text{m}^{-1}$. Using Eqn. (2.19) to (2.23), a nonlinear refractive index $n_2 \approx 5.3 \cdot 10^{-13} \text{ cm}^2/\text{W}$ has been estimated using the effective area computed from numerical simulations.

These first experiments with ChG PCF and SCF structures helped us to decide the fiber geometry for further experiments in this project. Both AsSe and GeAsSe PCFs

have shown good uniformity and ease of handling. AsS SCF, however, is not suitable in this project due to its low mechanical strength, core fluctuation, and strong multimode behavior. In the following content of this thesis, we will concentrate our discussion on ChG PCFs.

4.5 Design of tapered GeAsSe PCF

For distant wavelength conversion to happen, the pump laser needs to be set close to the ZDW. Dispersion engineering is possible thanks to the geometry freedom offered by microstructured fibers. By enhancing the waveguide dispersion of ChG PCF, it is possible to shift the ZDW towards to pump laser wavelength (i.e. 2 μm band). However, larger diameter-to-pitch ratio would also increase the fabrication difficulty, especially for soft glasses. The fiber design simulates the dispersion of a realistic hole-period upper limit to the ratio at $r = 0.7$ provided by the manufacturer. Simulation results indicate that varying this ratio alone is not enough to shift the ZDW down to 2 μm . For this purpose, a further reduction of the core size diameter is needed, implying a further technological step for tapering the fiber. While maintaining the PCF structure in the tapering process is not trivial, low loss tapered GeAsSe PCFs can be made with good uniformity and performance. Chalcogenide PCF tapers were originally investigated to increase the nonlinearity through a reduction of the effective area. In our design we thus combine high ratio and a small fiber core diameter for dispersion management, more precisely to shift the ZDW around 2 μm .

The proposed fiber geometry is shown in the insets of Fig. 4.11. The core is the circle tangential to the first ring of air-holes. Currently, a three-ring of air holes geometry is achievable in fabrication. From a simple geometry analysis, the fiber core diameter ϕ follows the relation:

$$\phi = (2\Lambda - d)T = \left(\frac{2}{r} - 1\right)dT \quad (4.1)$$

Here, T is the scaling or tapering factor for simulating the tapering process. We assume that the ChG PCF core diameter can be tapered down to 1.5 μm with a good uniformity. Since we do not have a Sellmeier equation for our fiber material $\text{Ge}_{10}\text{As}_{22}\text{Se}_{68}$, we used the Sellmeier equation of $\text{Ge}_{11.5}\text{As}_{24}\text{Se}_{64.5}$ [1] in the COMSOL simulation instead. In the purple and green curves of Fig. 4.11, we managed to blue-shift the ZDW of ChG PCF down to 1.995 μm with a ratio $r = 0.64$ through the tapering process. However,

the larger r means more difficulty in ChG PCF fabrication. Therefore, we select the ratio of 0.64 instead of the ratio 0.66.

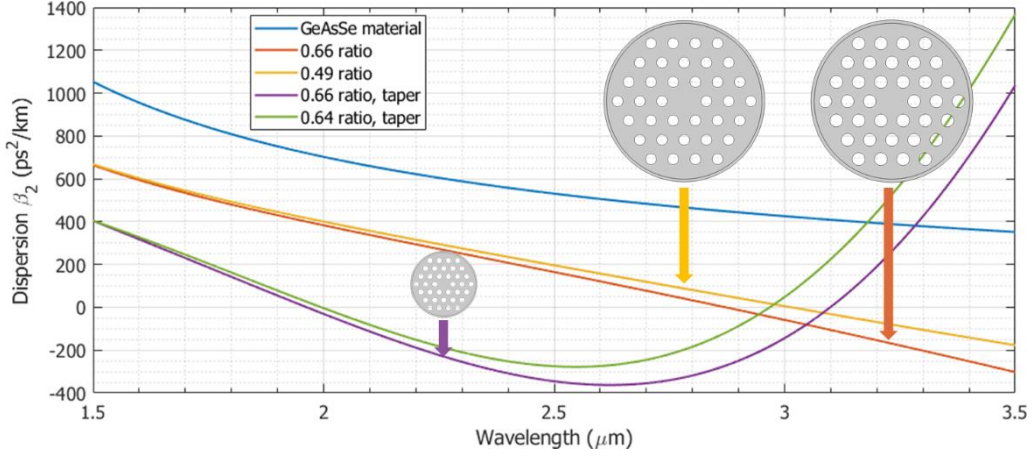


Figure 4.11. The dispersion of designed fiber and tested fibers. Inset: PCF geometry of 0.49 ratio and 0.58 ratio. After tapering down to 1.5 μm core, one can shift the ZDW to 2 μm band.

Figure 4.12 shows the simulation result for the GeAsSe T-PCF with a ratio of 0.64 at three pump wavelengths. In this simulation, we consider a coupled power of 50 mW into the 1 m fiber waist. At the 2 μm band, the theoretical effective area is approximately $1.7 \times 10^{-12} \text{ m}^2$. Employing the measured value for the nonlinear refractive index, the calculated nonlinear parameter is $\gamma = 9.8 \text{ W}^{-1} \text{ m}^{-1}$. For all the simulations, we neglect fiber loss and pump depletion.

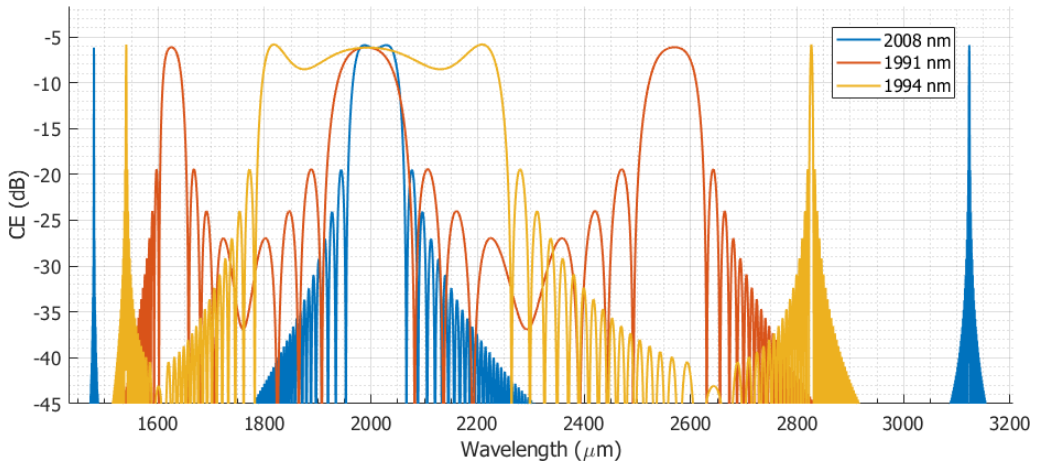


Figure 4.12 The simulated CE plot with two pump wavelengths at normal and anomalous region

For a broadband conversion, the pump laser lies close to the ZDW to merge the MI peaks into the central lobe. Pumping at 1994 nm, one can achieve a 3 dB conversion bandwidth of 440 nm. When placing the pump in a slightly normal dispersion region, the phase mismatch from second and fourth order dispersion cancels each other and

result in distant FWM conversion. One option is to pump at 1991 nm. In this scenario, a signal in the 1620 nm band can convert into an idler at 2550 nm band, as the orange curve of Fig. 4.12. For a more distant conversion, another possibility is to involve even higher dispersion order into the phase matching condition. With a pump at 2008 nm, we can achieve a phase matching condition until the sixth order of dispersion. The phase matched signal at 1480 nm down converts into an idler wave at 3121 nm.

However, since COMSOL applies finite element method for solving partial differential equations, the effective refractive index solution is not a perfectly smooth trace. The finite size of individual element gives tiny fluctuations of the solution, leading to larger fluctuations at higher dispersion orders. Besides, for the real experiment, tiny variation of the PCF geometry can lead to huge change in β_4 and β_6 . We can only be sure that when pumped close to the ZDW, distant and/or broadband conversion could happen. However, the exact position to put the signal may differ a lot from the simulation. Therefore, we would use the FWM near pump to estimate the experimental ZDW. Then, by utilizing the high CE of ChG tapered PCF, we try to find the phase matched wavelengths using a CW pump and a broadband ASE seed.

Conclusion

In this chapter, we compared various fiber glass material and concluded that ChG is the most suitable glass for this project. By experimental comparison between SCF and PCF structured ChG fiber, we proved ChG PCF has good uniformity and mechanical strength. In the end, we designed GeAsSe T-PCFs to blue-shift the ZDW into the 2 μm laser band. The simulation of designed fiber geometries shows the possibility to have broadband and distant FWM from GeAsSe T-PCFs.

Chapter 5

Amplified parametric conversion

5.1 Introduction

In this chapter, we present the main experimental results from the tapered fiber as designed in chapter 4, for FWM experiments. At the beginning of this chapter, we describe the experimental setup for characterization of the fabricated ChG PCF tapers. Pumped at low power, we show the retrieved dispersion. By rotating the input PM lensed fiber, we map the birefringence of the ChG PCF tapers and report the geometry vibrations on the fast and slow axes. The taper dispersion is also retrieved using a low coherent interferometry method. We show that all the experimental results match perfectly with our simulations and the tapers have exceptional uniformity. With the low power FWM characterization, we conclude the ChG PCF tapers have a hole-period ratio varying from 0.56 to 0.58, instead of the targeted 0.64.

After we confirm the low propagation loss of our ChG PCF tapers with both linear and nonlinear characterizations, we move forward to improve the CE under CW pumping condition. In the second part of this chapter, we report our experimental results confirming a 5 dB signal gain and 3 dB amplified parametric conversion in the 2 μm band under continuous wave operation. The study of CE relation with pump and signal powers proves the amplification is due to parametric processes. We have checked the repeatability of our results using different ChG PCF tapers fabricated from the same fiber preforms at different times. In addition, the result is repeatable at different pump wavelengths. By closely monitoring the relation of input pump power and the output pump power, we can conclude on the stable coupling and good taper condition under all pump levels. At last, we show the importance to have a narrow linewidth pump laser

so as to avoid strong SPM of pump laser. It is worth mentioning that we did not observe purely thermal damage in any of the tested ChG PCF tapers under all the pump power levels and more than 70% relative humidity. These results are not only the first demonstration of amplified parametric conversion for CW MIR pump wavelength, but also confirms the possibility to operate ChG fibers under several MW/cm² of intra-core power intensity.

5.2 Experimental setup and fiber parameters

5.2.1 Fiber geometry and fabrication

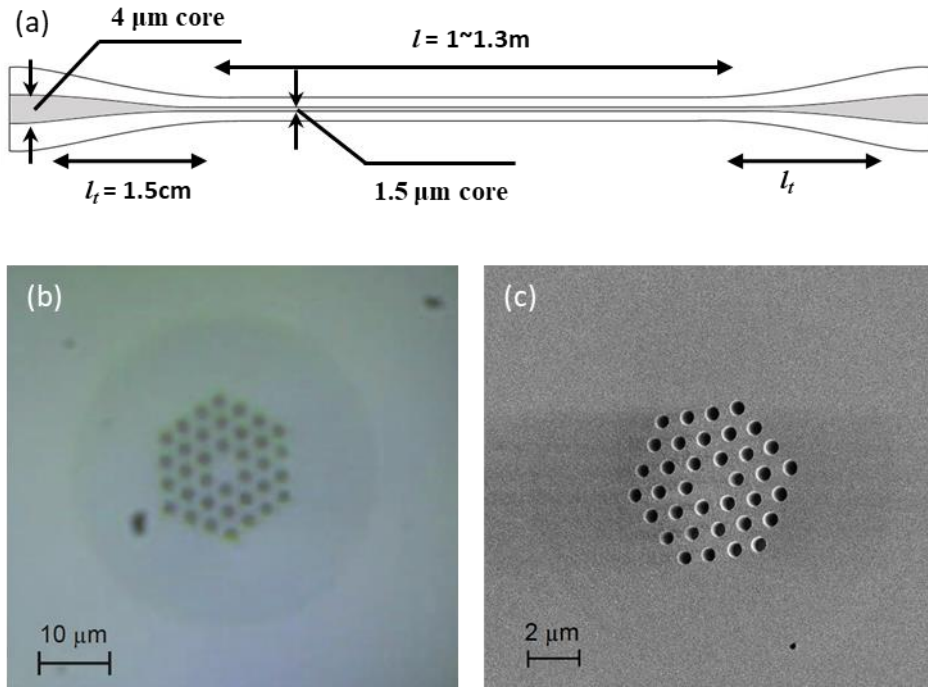


Figure 5.1 Dispersion engineered GeAsSe tapered PCF. (a). schematic of the GeAsSe fiber: the microstructured fiber of initial core size $\phi_s = 4 \mu\text{m}$ is tapered to a new core size $\phi_t = 1.5 \mu\text{m}$ over a length l . On either side of the taper is a $l_t = 1.5 \text{ cm}$ waist region acting as a mode filter. (b). Image of the fabricated microstructure fiber before tapering. (c). Image of the fiber after tapering, within the waist. The structure appears well preserved. The facet is prepared by manual cleaving

The zero-dispersion wavelength (ZDW) of a PCF is highly dependent on the hole-period ratio (ρ). Based on the results in chapter 4, we aimed for a ChG PCF with hole-period ratio $\rho \approx 0.64$. A segment from the fiber spool can be tapered to a core size of $1.5 \mu\text{m}$ for further blue-shift of ZDW [Fig. 5.1(a)] down to the $2 \mu\text{m}$ band.

The fabrication starts from a previously synthesized highly purified $\text{Ge}_{10}\text{As}_{22}\text{Se}_{68}$ bulk glass. The glass preform has an optical loss of 0.6 dB/m measured at $1.55 \mu\text{m}$

measured by SelenOptics. Part of the GeAsSe glass was then modeled to fabricate a preform with 3 hexagonal rings of air holes. The preform was drawn into a cane of 4 mm diameter. This cane was then inserted into an As₂Se₃ tube and the whole tube assembly was drawn into a photonic crystal fiber with an outer diameter of approximately 130 μm and a core size about 4 μm [Fig. 5.1(b)]. The period of hole, Λ , was measured to be approximately 2.88 μm and the air hole diameter was 1.69 μm ; leading to a hole-period ratio of 0.58 measured by the manufacturer. Clearly, the hole-period ratio is smaller than the designed value of 0.64, leading to a ZDW beyond 2.1 μm . The propagation loss of the PCF was measured to be 0.65 dB/m at 1.55 μm using a cutback experiment by the manufacturer. With a segment of this PCF, tapered fibers with about 1 m waist were then fabricated on the drawing tower at a temperature around 270 °C. During the fabrication process, the PCF holes are purged by nitrogen gas to prevent shrinking. Due to the slight variations in temperature control, tapering speed and nitrogen gas pressure, we expect a shrink and variation of hole size among different samples. In the following experiment part, we will investigate this assumption. The core diameter in the waist portion was decreased to approximately 1.5 μm and the transition length l_t is around 1.5 cm [see Fig. 5.1(c)]. The fiber fabrication and tapering are performed by SelenOptics.

Table 5.1 Data of FUTs in this experiment

	Insertion loss	Production date	Waist length
T-PCF1	9 dB	2015.12	0.8 m
T-PCF2	10 dB	2016.07	1 m
T-PCF3	8.5 dB	2016.07	1.12 m
T-PCF4	8.5 dB	2016.09	1.2 m
T-PCF5	5 dB	2017.01	1 m

In Table 5.1, we summarize the known ChG T-PCF parameters at the beginning of the tests. For clarification, we will differentiate the tapers by their production set number. In the following context, the ChG PCF tapers will be referred as T-PCFs with a number to distinguish different samples. The T-PCFs fabricated from the same month have very similar tapering condition, hence similar hole-period ratio. Since all the T-PCFs are research fibers, their property and transmission vary from set to set. All the T-PCFs were stored with silica gels under the relative humidity of 30%. In the Table 5.1, we perform the in- and out-coupling to the T-PCF using a pair of identical lensed fiber. Hence, the insertion loss here includes in- and out-coupling loss, Fresnel reflection, loss of taper transitions and linear propagation loss.

5.2.2 Experimental setup

While an interferometric method was used to characterize the dispersion of the untapered PCF, it cannot be directly applied to measure the dispersion of the tapered ChG PCF structure shown in Fig. 5.1(a) since the phase delay contribution from the untapered and transition sections are significant and could not be decoupled from the targeted contribution of the tapered region only. Therefore, to perform an interferometric measurement, the fiber sample must contain the ChG PCF waist only. On contrary, in the FWM method, the nonlinear conversion from other part of taper is negligible compared with taper waist. Therefore, we can apply the low power FWM process to retrieve the dispersion of the taper waist directly. This process also can provide a good indication of fiber uniformity, suppression of higher order modes and strength of birefringence.

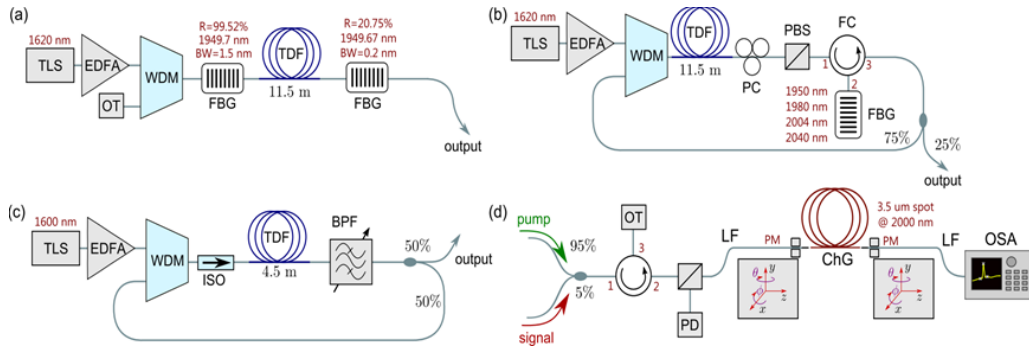


Figure 5.2 Experimental setup for GeAsSe T-PCF characterization. TLS: tunable laser source; WDM: wavelength division multiplexer; TDF: Tm-doped fiber; OT: optical terminator; ISO: isolator; PC: polarization controller; BPF: bandpass filter; PBS: polarization beam splitter; PD: photodetector (2 μ m); LF: lens fiber; (a). Pump laser cavity used to get parametric amplification in our experiment, which favors high slope efficiency and simple geometry to avoid pulsing; (b). Pump laser cavity for low power characterization and dispersion retrieval of ChG fiber. An additional PC was inserted at the output of coupler before going to the PBS. (c). Tunable signal laser; (d). Complete setup for light injection and data recording.

We used an all-fibered FWM set-up, detailed in Fig 5.2. The sources in this test were covered in detail in Chapter 3. We provide here a quick summary of their characteristics. The 2 μ m pump and signal lasers used in this experiment were implemented with Tm-doped fiber pumped by an amplified 1620 nm laser source. The pump laser utilized either linear or ring cavity depending on the wavelength. To achieve signal amplification, a high slope efficiency, linear cavity laser was built with a 1950 nm fiber Bragg grating (FBG) pair. Due to a lack of matched FBG pairs at other

wavelengths, a ring cavity was built and different FBGs were used to select the pump wavelength for dispersion characterization. Both pump configurations were checked using a photodetector to confirm CW operation and no parasitic pulsing operation. The pump laser linewidth was measured to be approximately 0.08 nm at 1950 nm in the linear cavity configuration. The signal laser was based on a ring cavity where the wavelength was selected by a tunable bandpass filter of 1 nm linewidth. The length of the Tm-doped fiber was 11.5 m in the pump and 4.5 m in the signal laser. The output from pump and signal lasers were combined by a 95/5 fiber coupler, designed to operate at 2 μm , and then send through a 2 μm circulator to prevent back reflection. A fibered PBS was mounted after the circulator. One arm of the polarizer was connected to a PM lensed fiber for coupling into the PCF and the other arm was used for power monitoring. The PM lensed fiber was fabricated with PM1550 and has a beam spot diameter of approximately 4 μm at 2 μm wavelength. The output from the chalcogenide fiber was collected using another PM lensed fiber with the same parameters. The lensed fiber was then connected to an optical spectrum analyzer (OSA), Yokogawa AQ 6375, for data recording. A total insertion loss of 8.5 dB was measured at 1950 nm for T-PCF3, where approximately 4.5 dB are the total coupling losses (including Fresnel reflection), 3.4 dB comes from the transition regions and 0.6 dB comes from propagation losses (α). The insertion loss fluctuations among different T-PCFs, except for T-PCF5, come from variations of cleaving quality, coupling efficiency and loss in the transition regions. For T-PCF5, a longer transition region and a better coating, dramatically reduced the total insertion loss by more than 3dB. By rotating the input PM lensed fiber in an increment of 15 degrees, we can change the input angle of the linearly polarized pump laser. We then perform a sweep of signal at each input rotation to estimate the birefringence of the T-PCF.

Figure 5.3 shows the dispersion simulations with various hole-period ratios for T-PCF with 1.5 μm core diameter. Among different T-PCFs, the hole variations come from the hole shrinking during the tapering process [160, 161] and leads to different dispersion among T-PCF samples. For a single T-PCF, the fluctuations of hole sizes lead to fiber birefringence. When we pump close to the expected ZDW of the test fiber, we would expect a stronger influence from birefringence on the conversion bandwidth when rotating the input lensed fiber, as is illustrated in the insets of Fig. 5.3. Ideally, for more accurate measurement, the FWM characterizations should be conducted at wavelength longer than 2.1 μm . However, since not all lasers presented in chapter 3 were available during the early tests, we present mainly FWM results tested using Tm-doped fiber lasers operating at a maximum pump wavelength of 2040 nm. At the 2040

nm, it is still possible to find the fast and slow-axis of our T-PCFs. The test data presented here were obtained with samples T-PCF1 and T-PCF5.

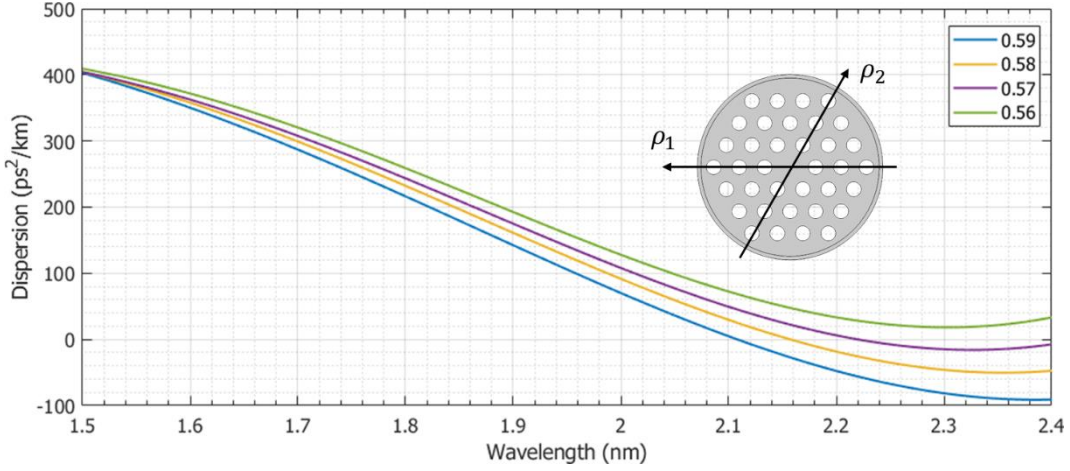


Figure 5.3 Dispersion simulation for different hole-period ratios. Inset: demonstration of birefringence due to hole-period ratio depending on the input polarization. The different dispersion from various hole-period ratios leads to different bandwidth in FWM experiment. By matching the retrieved dispersion with simulation, we can estimate the actual T-PCF hole-period ratio. In addition, one can notice more significant dispersion change among different hole-size ratios when getting closer to the ZDW.

5.3 T-PCF characterization at low and medium power

In this section, we present some notable experimental results when characterizing the T-PCFs with low or medium coupled pump powers. We show the experimentally retrieved FWM lobes and their high coincidence with theoretical simulations. Here, we refer to the low coupled power when CE is about -20 dB. For CE of around -15 dB, we consider the coupled power as medium power.

To start, we show the test result on T-PCF1 and explain the retrieval of fast- and slow-axis. By recording the FWM sweep over multiple lobes, we can deduce important information about the uniformity of the T-PCF. Knowledge about the fiber birefringence and uniformity is critical for broadband or far-detuned FWM processes as they are much more sensitive to any fluctuations. We show that at medium power level, the impact of the input un-tapered region starts to be more pronounced, contributing to a shift of CE dips. By including the CE contribution from this un-tapered region, the theoretical simulation and experimental results match perfectly for higher pump power conditions, giving us a full modeling of the fiber. In addition, the simulation of contributed CE from the un-tapered region can be used to re-check loss estimations in the taper transition region. This extensive experimental characterization

and extracted information is finally used to estimate the T-PCF hole-period ratio variations and the ZDW range.

5.3.1 FWM characterization of T-PCFs at low pump power

All our characterizations of T-PCFs start with low pump power level (around 10 mW of coupled power in taper waist). By using a low pump power, we can minimize the impact of other nonlinear optical effects and avoid potential fiber damages during the lengthy and extensive testing period. Low power operation also means that the effect of the un-tapered region on the dispersion is strongly suppressed. Therefore, the CE dip positions and depth is only impacted by the taper waist length and dispersion. The available pump laser wavelengths are 1950 nm, 1980 nm, 2008 nm, 2040 nm, 2090 nm and 2100 nm. In this sub-section, we mainly present the experimental data retrieved from T-PCF1 to avoid redundancy. For 2090 and 2100 nm pump wavelengths, a complete signal sweep was performed only recently such that the full characterization at 2100 nm pump is shown for T-PCF5 wavelength. The same characterization procedure was followed for all other T-PCFs.

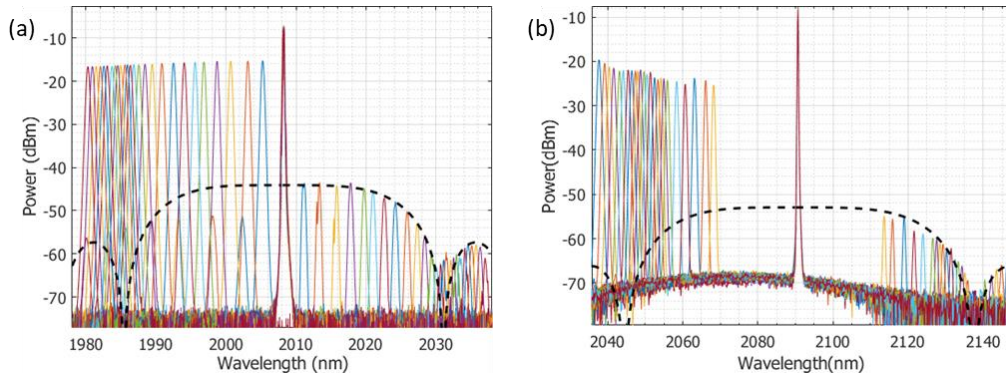


Figure 5.4. FWM spectrum together with theoretical fitting. (a) FWM with pump wavelength at 2008 nm. (b) FWM with pump at 2090 nm. Limited by the signal laser wavelength at the time of experiment, we could only cover up to 2070 nm (in year 2016).

Figure 5.4 shows two examples of FWM spectrum at 2008 nm and 2090 nm pump wavelengths. When recording the spectrum, we align the pump laser polarization so that the first dip appears at the longest possible wavelength. The largest conversion bandwidth implies smallest dispersion, hence the fast axis of the PCF. In this scenario, we ensure the recorded FWM traces are from the same fast axis. Then, using the coupled wave equation discussed in chapter 2, we fit the simulation result with recorded data and retrieve the fiber dispersion (T-PCF1 in this case). Limited by the operation wavelength of our signal laser, we could only sweep the signal up to 2070 nm [Fig. 5.4(b)]. However, we still managed to find the first dip and second lobe, hence deducing

the dispersion at 2090 nm pump wavelength. We have performed similar experiment with 1980, 2040 and 2100 nm pump wavelengths. A summary is made at the end of this section.

The input light polarization was rotated to record the change of CE bandwidth to check the fiber birefringence. Here, we show the FWM test with pump wavelength at 2040nm on T-PCF1, where Tm-doped laser and optical components work better, and the pump wavelength is close to the ZDW. Before going to the ChG PCF, a polarizer was added to make sure the polarization maintains constant during the sweep of signal wavelength. The rotation of input polarization was achieved by rotating the lensed fiber chuck. After each rotation of lensed fiber, we perform minor adjustments to recover the coupling of the T-PCF. Typically, the rotation angle of PM-lensed fiber is 0, 45, 90 and 135 degrees. In some cases, we use smaller rotation steps to reach higher precision.

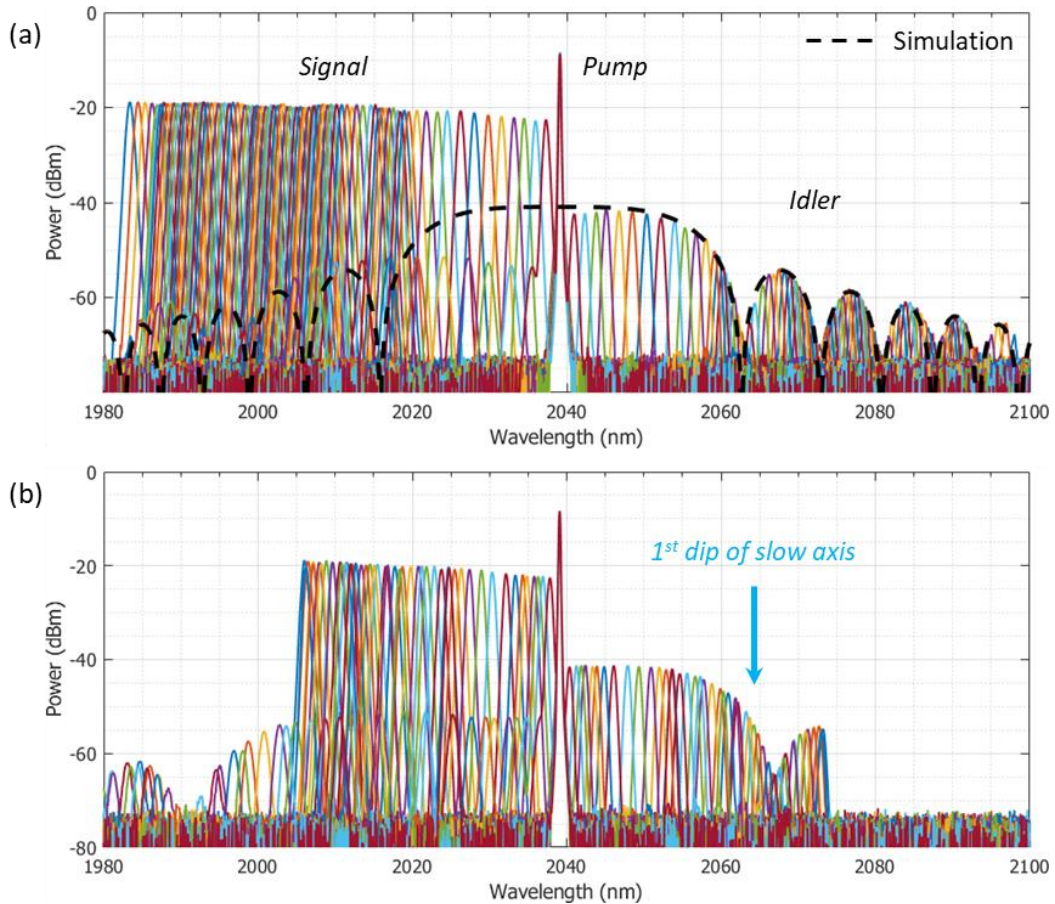


Figure 5.5. Spectrum indicating birefringence of T-PCF1. (a) Superimposed spectrum of a complete sweep with pump at 2040 nm. The coupled pump power is approximately 10 mW, leading to a CE of -20 dB. (b) By rotating the PM lensed fiber at input, we managed to find the slow axis of T-PCF1. The pump power is fixed at roughly the same value as (a).

Figure 5.5 shows a superposition of signal sweep with pump laser fixed at 2040 nm with input polarization aligned at slow- and fast-axis, respectively. The T-PCF1 has

a taper waist length of 80 cm. With approximately 10 mW of coupled power, the maximum CE can reach -20 dB. The 3 dB bandwidth of conversion is about 32 nm, when pump aligns to the fast-axis. A preliminary fitting, indicated by the dashed lines in Fig. 5.5(a), is a signature of small propagation loss and exceptional uniformity of T-PCF1. By rotating the input PM lensed fiber, we found the fast-axis in Fig. 5.5(b), where the 1st CE dip is about 4 nm broader than the slow axis. The dispersion β_2 for fast and slow axis is 53.49 ps²/km and 73.70 ps²/km, respectively. This dispersion variation matches with the dispersion for hole-period ratio change from 0.58 to 0.585. From our simulation in Fig. 5.3, the ZDW varies from 2.13 to 2.16 μ m, which could be reached by a carefully designed Ho-doped fiber laser.

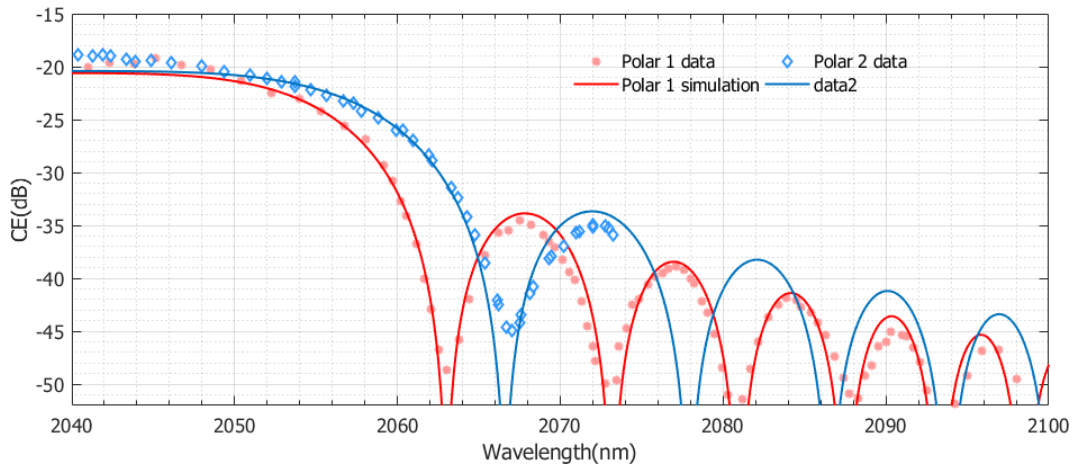


Figure 5.6. Retrieved CE data and simulation on the fast (blueish color) and slow (reddish color) axes. This different corresponds to effectively 1 % fluctuations of the hole-period ratio.

We then use the Eqn. (2.31) to retrieve the dispersion by fitting the measured FWM data points. The linear loss is set to 0.5 dB/m by fitting the curvature of the experimentally retrieved points near the dip. This loss estimation agrees with our measurement in chapter 5.2. The nonlinear refractive index n_2 of our GeAsSe fiber was measured from our previous work [67]. Since the pump laser is CW and low power, this simplified NLSE, is valid for dispersion retrieval. The nonlinear coefficient γ and the coupled optical power were all fixed using values deduced from previous measurements. The effective area for each wavelength comes from simulation results using the commercial FEM software COMSOL. The fitting with Eqn. (2.31) was performed to match the theoretical and experimental dip/minima of the CE positions. The tolerance of this fitting was set to 0.05nm. Using this method, we retrieve the dispersion of fast- and slow-axis of T-PCF1 as in Fig. 5.6. The lower CE on the second lobe for both polarizations is likely due to small fluctuations in the coupling efficiency, which has twice impact on the CE in dB scale. One can notice the dip level is higher

than the simulation. This is due to the CE contribution from the un-tapered region, which will be further explored in chapter 5.3.2.

Ideally, the hexagonal shaped PCF structure should not express any birefringence [162]. However, two main sources lead to inevitable breaking of its geometry symmetry and cause birefringent. First, minor variations of preform hole sizes always exist. Then, during the taper process, the difference in nitrogen pressure among the holes results in further hole size variations. The size fluctuations of cladding air hole size lead to effectively a different hole-period ratio depending on the input light polarization angle with respect to the fiber facet. For a single T-PCF, this polarization dependent dispersion corresponds to fluctuation of ρ of less than 1%, further proving the good uniformity of the tapered PCF. By comparing the dispersion of all sets of T-PCFs, we conclude a total hole-period variation of 2% as indicated in Fig. 5.7.

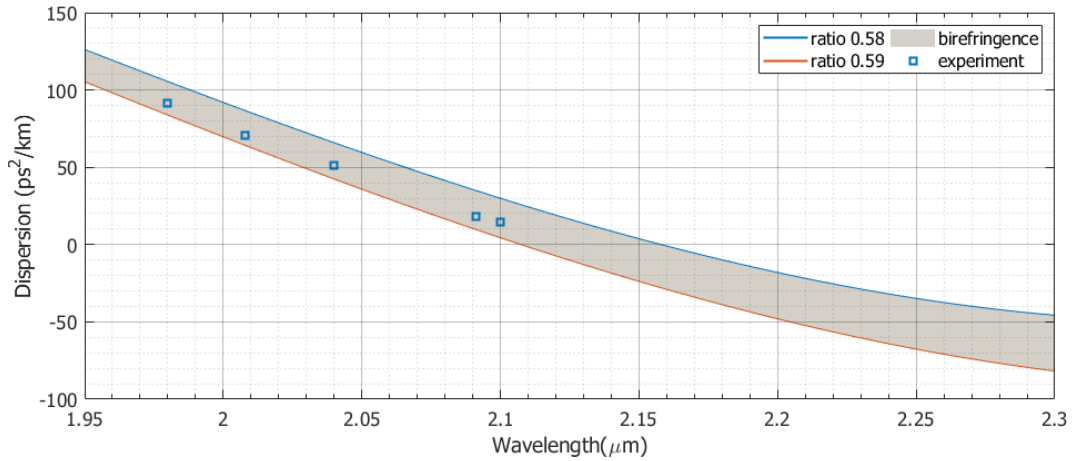


Figure 5.7. The retrieved dispersion from T-PCF1 and simulations at several wavelengths. In this plot, we fixed the polarization on the fast axis of the T-PCF.

Due to the limited availability of 2.1 μm fiber components, we have only recently managed to build the 2.1 μm tunable fiber laser as the signal laser. The signal laser utilizes the same cavity configuration demonstrated in Fig. 3.8.

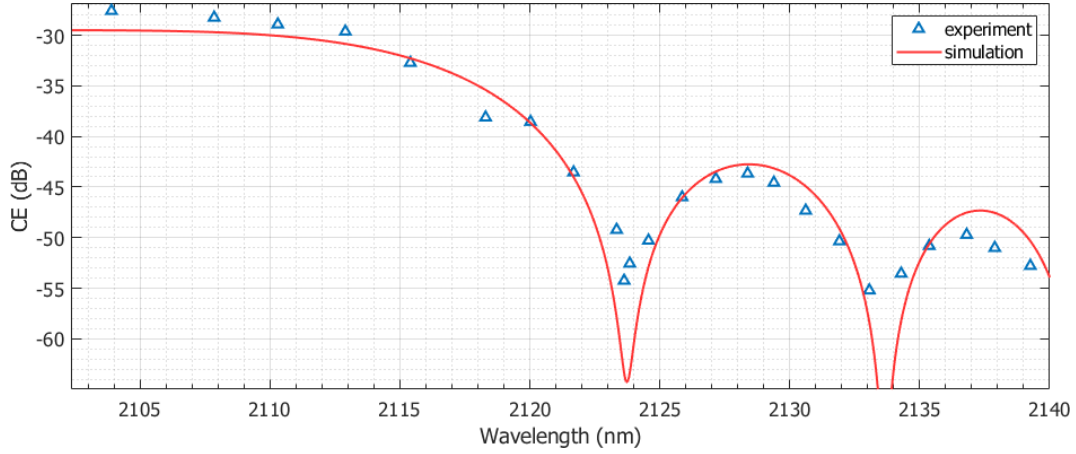


Figure 5.8. The retrieved dispersion with 2.1 μm pump from T-PCF5. The improved Tm-doped fiber laser covering the entire 2~2.1 μm is recently developed.

As a result, only the T-PCF5 has been fully characterized at 2.1 μm wavelength. Figure 5.8 shows data retrieved after a sweeping of signal laser from 2060 to 2100 nm. Further signal detuning is not performed due to the fast drop of CE and limited pump power. With a coupled pump power of about 4 mW, the maximum CE reaches -28 dB. The retrieved dispersion of T-PCF5 is approximately $63.7 \text{ ps}^2/\text{km}$, corresponding to the dispersion of 0.565 hole-period ratio. Limited by the noise floor of OSA, the dips of CE are higher than simulated. Note that the total insertion loss of T-PCF5 is less than 5 dB. Thus, the coupled power between the taper and un-tapered region is very similar. In the case of low pump power, the impact of the un-tapered part can be safely neglected.

5.3.2 Impact of transition un-tapered fiber

As previously discussed, the depth of CE dips can be used to retrieve the linear loss of fiber samples. While this is always true with standard fibers or un-tapered ChG PCFs, for T-PCFs more parameters need to be taken into consideration. As Fig. 5.1(a) illustrates, the T-PCFs consists three distinct sections: un-tapered PCF, transition region and taper waist. All the regions have a contribution to the FWM process. Our T-PCFs all have taper transition regions of around 2 cm, which is more than 50 times smaller than the taper waist length. Therefore, it is reasonable to ignore their contribution in the FWM process when the CE is low. However, the un-tapered part can be longer than 15 cm. Consequently, when the coupled power is higher (for $CE > -20 \text{ dB}$), the CE in the long un-tapered segment alone could reach more than -40 dB. While still lower than the CE expected from the waist segment, the position of the CE dips for un-tapered and waist regions will differ due to the dispersion difference. In rare cases, the peak conversion from the un-tapered region could overlap with the dips of the taper waist.

In this case, the dips of the resulted overall CE trace will be higher and lead to an over-estimation of T-PCF's linear loss.

To solve this problem and provide a more accurate modeling of the FMW process, we simulate the contribution of the un-tapered input side and add the corresponding generated idler linearly to the final output, as indicated in Fig. 5.8. The experimental data plotted in Fig. 5.8 comes from a FWM sweep on T-PCF4, with a coupled power of 15 mW in the taper waist and 25 mW in the un-tapered region at input side. The un-tapered region on the output side has little contribution to the CE trace, due to an even lower pump power inside and can therefore be safely neglected. We can confirm that the un-tapered region has limited effect on the CE spectrum shape: the position of the dips is unaffected due to the strong dominance of the long waist region dispersion. However, we observed a decrease in the depth of FWM dips. To retrieve the fiber parameters from such FWM traces, fitting with the slope of the lobes is more precise than fitting with the bottom of the dips. Overall, it is still more suitable and precise to perform the characterization of T-PCF at very low pump power, typically around 5 mW, which completely avoid the impact of the un-tapered input segment.

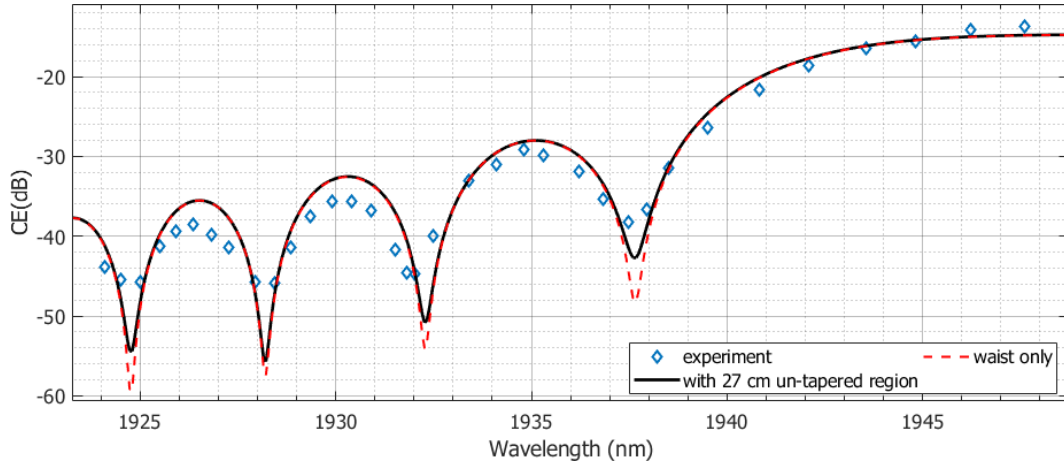


Figure 5.9. The retrieved data from T-PCF4 using 1950 nm pump laser. The CE contribution from un-taper region increased the dip value, but the position sees only trivial changes.

5.3.3 Temperature dependence

Naturally, one might consider the impact of environmental condition to the T-PCF's dispersion, one of them being temperature. Due to thermal expansion, the hole-period ratio is dependent on the environment temperature. From previous researches [163], however, ChG was found to exhibit a very small thermal expansion. Therefore, we would expect the same or very similar dispersion characteristics of the T-PCFs at various temperature conditions.

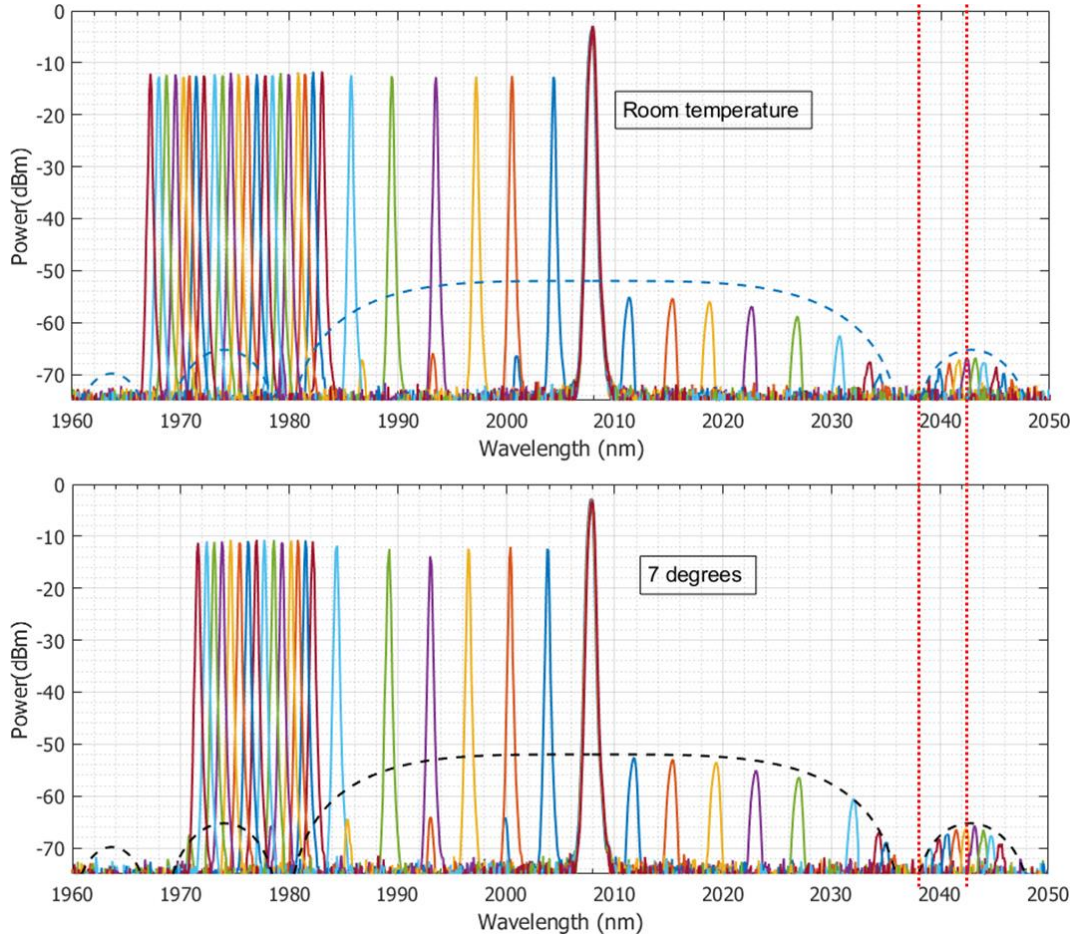


Figure 5.10. Test of fiber dispersion at different temperature. Clearly, the peak of the second FWM lobe remains identical at 7 and 22 degrees.

We conducted the experiment on a 28 cm T-PCF waist. To cool down the sample temperature, we put the fiber close to an ice folded by an aluminum foil. We then carried out the experiment at stabilized temperature around 7 °C. An infrared thermal meter monitored the T-PCF environment temperature during the whole test. Figure 5.10 shows the FWM trace at lab temperature and 7 °C. No difference in the dip or peak positions could be observed. As a result, we confirm that normal lab temperature fluctuations will not impact the precision of our experimental measurements.

5.3.4 Summary of the test results

Comparing the experimental results and simulations, we can estimate that the T-PCFs available for testing have a hole-period ratio varying from 0.56 to 0.59. The interferometric measurements performed on both the un-tapered and tapered segments further confirmed the results from FWM and simulation. The details of this low-coherent interferometry method are explained in detailed in [164]. In Fig. 5.11, we present a summary of all our experimental and simulation results on T-PCF GVD values. To avoid redundancy, the data points for T-PCF2 and T-PCF4 are not plotted as they

coincide with the ones for T-PCF1 and T-PCF3, respectively. T-PCF4 has the same hole-period ratio as T-PCF1 while T-PCF2 has the same ratio as T-PCF3. One can also notice that the GVD values of T-PCF3 and T-PCF5 are identical at 1980 and 2008 nm pump wavelengths. Thus, they both have the same hole-period ratio. The difference measured at 2040 nm is an indication of birefringence of T-PCF3.

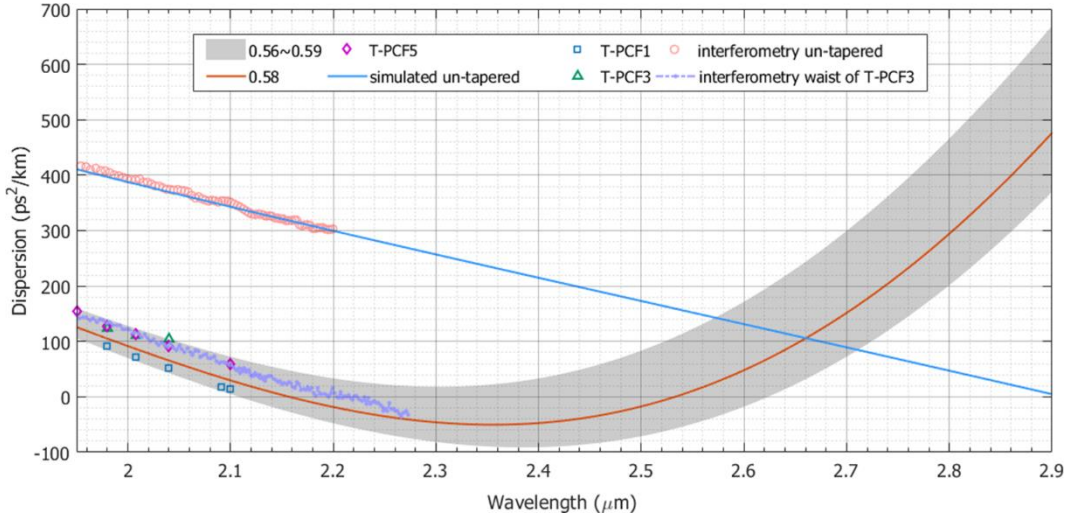


Figure 5.11. The summarized data from various T-PCFs. The birefringence corresponds to 1% effective hole-period ratio fluctuations. Among different T-PCFs, the fluctuation is around 2%. In addition to parametric conversion, the interferometric method is applied to both tapered and un-tapered PCFs. Good matching from simulations and experiments is obvious.

The excellent agreement with simulation indicates the accuracy of our model and the excellent quality of the tapered fibers. In addition, we also show in the same graph the simulated and measured dispersion of the ChG PCF before tapering, i.e. core diameter at 4 μm . Before tapering, the ZDW is expected around 2.9 μm . The tapering process helps to red-shift the ZDW to 2.1~2.2 μm , which is closer to the Tm-Ho fiber laser band. The hole-period ratio fluctuation from 0.56 to 0.58 can be translated to a fabrication variation of 2%. It is worth mentioning that the variation between T-PCFs is a common result due to change of tapering condition, like nitrogen pressure, tapering temperature, temperature slope, motor speed, etc. However, for each T-PCF, the hole-period ratio is highly constant as indicated from our FWM measurements.

While simulations indicate a slight multimode behavior, the transition region acts as a mode filter so that only the fundamental mode propagates in the taper waist region. The single mode operation is confirmed both in FWM experiment and interferometry measurement. We believe it is due to the good mode match between the input lens fiber and PCF fundamental mode. In addition, the PCF structure is found to be more immune to higher order modes due to the strong difference in wave vector between different

modes [88]. Therefore, it is more difficult to excite higher order modes when input beam diameter matches with the fundamental mode of GeAsSe PCF.

Another important conclusion of these tests is that the fabricated ratio is lower than the targeted one. The consequence, as mentioned above, is that the ZDW is longer than expected. Our initial goal of broadband or far-detuned/distant FWM requires a pump positioned near the ZDW. For our fabricated fibers, it means that a pump laser between 2.12 and 2.2 μm is required. This wavelength is however beyond the optimal or conventional operation range for Tm- or Ho-doped silica fibers. With the currently available sources and fibers, we therefore first aim on improving of the FWM CE. Indeed, practical MIR fiber sources would also require high CE but very few MIR waveguided platforms can reach +0 dB CE in single path configuration, and none so far in CW pump configuration.

5.4 Amplified parametric conversion

In this section, we will concentrate our experimental results and discussions on T-PCF4. Since this is the last T-PCF tested for amplified conversion, the data of T-PCF4 is the most complete. Chapter 5.4 starts with the experimental results on amplified conversion. We then analyze the results to prove that the purely CE comes from parametric process. At the end, we show the amplified parametric conversion spectra from T-PCF1 and T-PCF3, to prove the repeatability of our results on different samples and at different pump wavelengths.

5.4.1 Impact of laser linewidth

A CW laser does not equal to a single-frequency laser. Thus, the SPM effect is inevitable. As explained in chapter 3, the 2.04 μm pump laser uses a broadband FBG as wavelength selection element. In addition, operation at 2.04 μm with Tm-doped fiber requires higher output ratio to reach enough power to achieve CW parametric amplification [see the ASE in Fig. 3.7(b)]. With a low Q-factor cavity and a large bandwidth FBG, the laser linewidth of our 2.04 μm laser can easily exceed 0.4 nm. However, we expect a larger FWM conversion bandwidth when pumping closer to the ZDW. Thus, it is still worth investigation high power operation with this laser despite its relatively large linewidth.

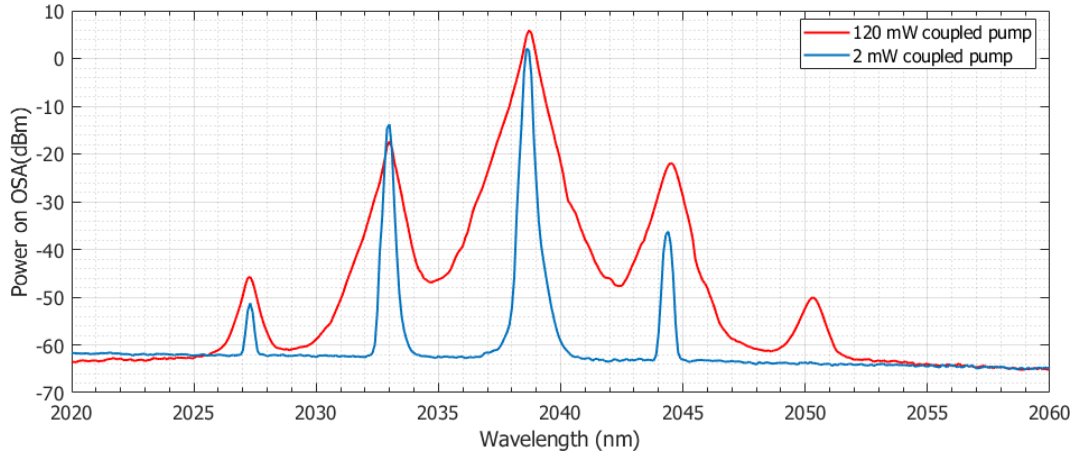


Figure 5.12. Broadening of pump laser linewidth due to strong nonlinearity of T-PCF. The drop of signal power comes from the misalignment on the output side because of laser radiation pressure.

After a fiber fuse at the middle of the waist on T-PCF2 (detailed in next section), we used the remaining half of the taper for experimenting with the 2.04 μm pump. This half taper (50 cm long) from T-PCF2 has an total insertion loss of 11 dB, the increase being mainly due to the output coupling loss. Figure 5.12 shows the OSA recorded spectra at the output of the taper with 2mW (blue) and 120 mW (red) of coupled pump power. The strong SPM experienced by the pump at high power significantly distorted the pump spectrum. This SPM effect is also converted to the 1st and 2nd order signal and idler through FMW. Such distortion is clearly not acceptable for a nonlinear parametric converter. At high pump power, the signal peak value also seems to be lowered by 2 dB. This is a consequence of output misalignment due to radiation pressure.

To avoid strong pump SPM and provide the best possible characterization, a smaller linewidth laser is necessary. As such, we reverted to 1950 nm operation, closer to the Tm-doped fiber ASE peak, enabling the construction of a simpler linear cavity with higher Q-factor and less in-cavity components. In the following test with T-PCF3 to 5, we thus performed the main characterizations with this 1950 nm laser. We used the 1980 nm laser only to confirm the repeatability at other wavelengths.

5.4.1 Experimental results

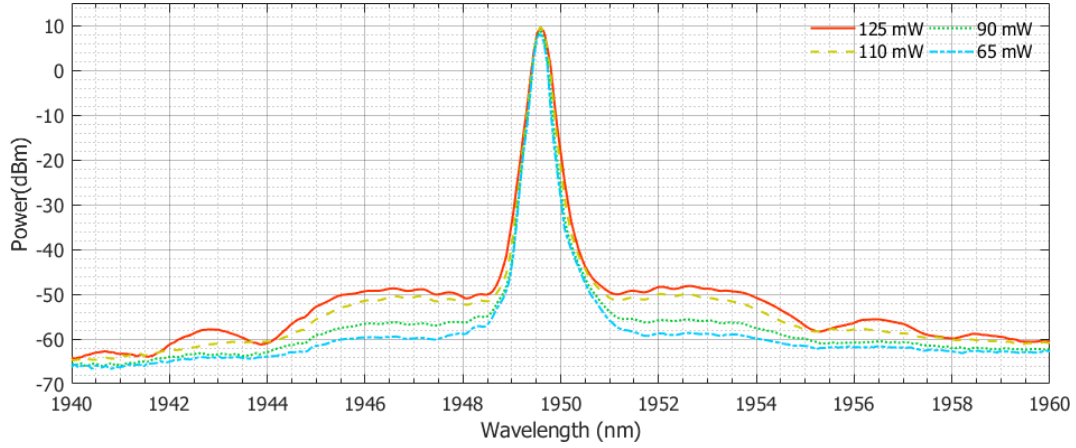


Figure 5.13. The amplification of laser ASE at various pump power. The ASE shows a clear phase matching feature with local maxima and minima. In addition, no strong SPM can be noticed.

During a FWM process, the ASE from the pump laser can also act as seed for the parametric process. Thus, the ASE near the pump wavelength will grow and express the features of conversion maxima and minima, which is clearly demonstrated by Fig. 5.13. Since the laser ASE is not constant over wavelength, one would also notice unbalance between the red and blue side of the pump laser. Once the coupled pump power reaches 125 mW, one can notice three orders of cascaded FWM, indicating high efficiency of the process. More importantly, no obvious pump broadening can be seen during increase of pump power. Therefore, the pump laser will not induce distortion to the signal laser and the idler laser will truthfully replicate the signal laser properties.

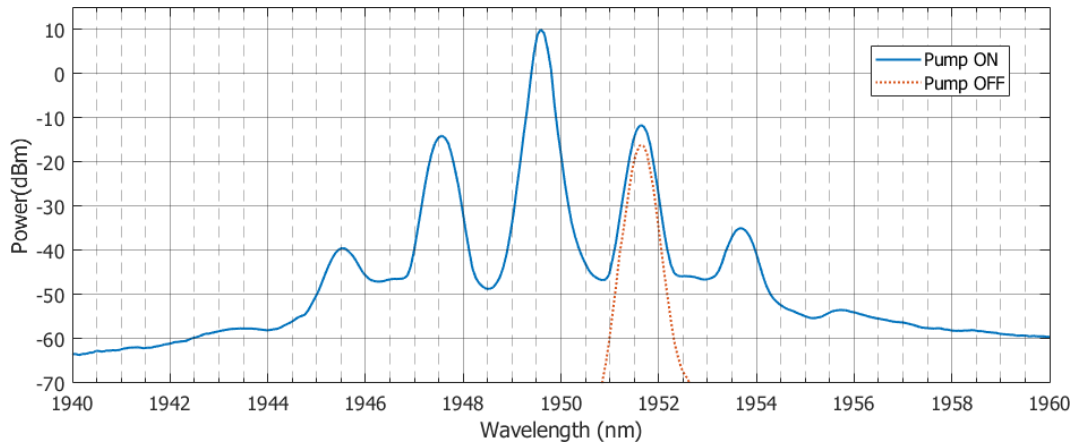


Figure 5.14. The ON/OFF signal amplification recorded on OSA. The signal power is taken with pump off. We can see obvious signal gain and idler amplification.

At the coupled power of 125 mW, we tune the signal laser 2 nm longer than the pump wavelength. The signal has a coupled power of about 1 mW. We illustrate the resulting spectrum in Fig. 5.14. When the pump laser is on, one can notice a cascaded

FWM up to the 3rd order. For the cascaded FWM processes, either the signal or the idler acts as the “pump” and the pump acts as a new “signal” laser. As a result, part of the signal and pump laser power will be converted into the cascaded idler peak. Reading from Fig. 5.14, the signal laser experiences about 4.7 dB on-fiber gain (ON/OFF amplification) and the idler on-fiber CE is about 2.4 dB. The signal gain and idler CE satisfies the relation given in Eqn. (2.20).

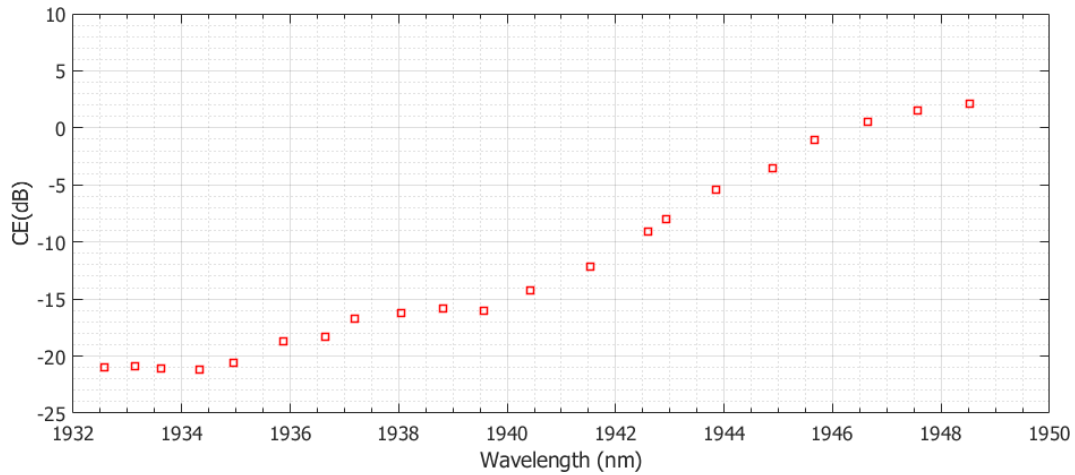


Figure 5.15. The retrieved data points with 125 mW coupled pump power. The maximum CE reaches about 2.4 dB. We can still see the local minima and maxima.

When sweeping the signal laser at a given pump power level, the idler as a function of wavelength can be recorded, as shown in Fig. 5.15 for a signal positioned on the blue side of the pump. Here, we show the recorded data at the maximum pump power of 25.5 dBm, corresponding to a coupled waist power of 125 mW. Due to the non-negligible contribution of the input un-tapered region, the dips are not as deep. Because of the combination of parametrically amplified laser ASE and laser SPM due to finite linewidth, it is difficult to match the experimental data perfectly with simulations. For 4 nm around the pump (one sided), we have an idler CE larger than transparency ($CE > 0$ dB). The -20 dB bandwidth is about 15 nm (one sided). The first dip happens at 1940 nm – a few nanometers earlier than for the measurement with low pump power (< 10 mW). This can be explained by the nonlinear phase mismatch which, at high pump intensity, starts to induce strong impact on the FWM trace bandwidth.

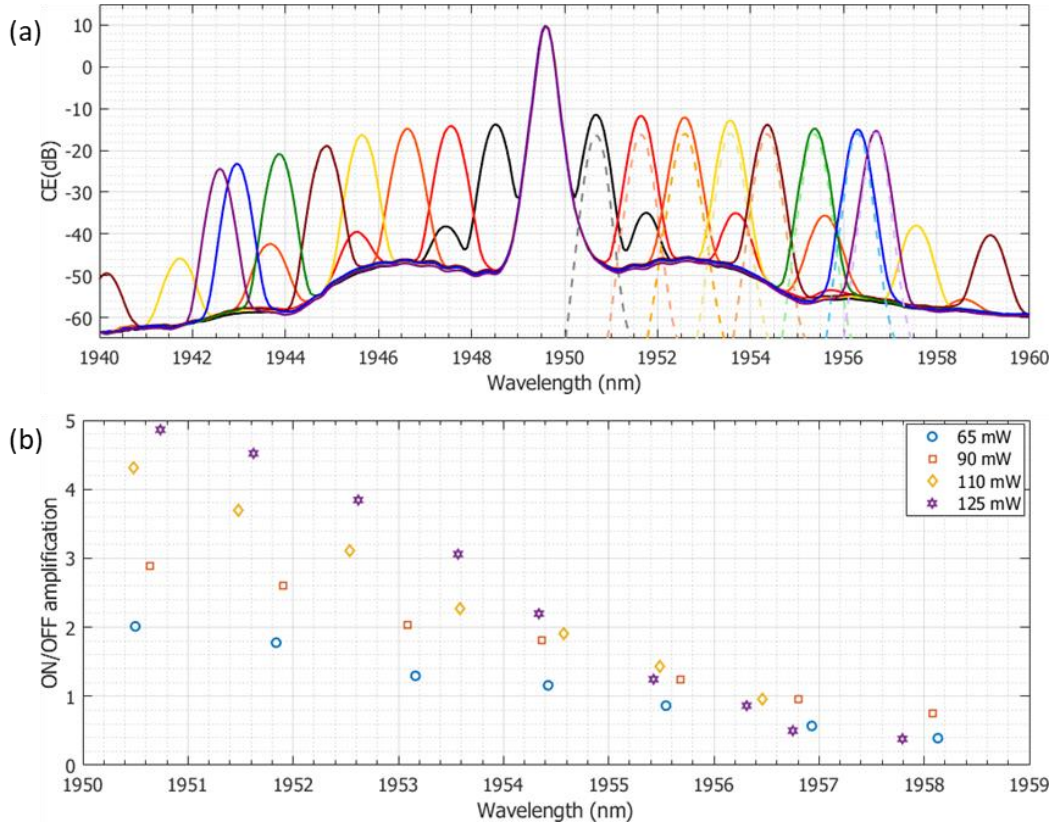


Figure 5.16. Parametric amplification of T-PCF4 with various signal laser positions. (a) OSA recorded traces from T-PCF4. The dashed spectrums are the reference signals with pump off. (b) Superimposed ON/OFF amplifications at various pump power. The shrink of bandwidth is a result of increased nonlinear phase mismatch.

As expected from the theory, we have observed a similar sinc shaped signal gain trace on the red side of the pump laser. Figure 5.16(a) shows the recorded spectra during the signal sweep for a coupled pump power of 125 mW. One can notice strong signal gain for detuning within the first ASE lobe. In Fig. 5.16(b), we show the experimental data for signal gain at four coupled pump power levels. The ON/OFF amplification is calculated using the ratio between the measured output signal power without pump laser and with pump laser on. Due to the operation in the normal dispersion regime, we notice as expected a narrowing of the first dip position with increasing pump power levels. This effect will be discussed in more detail in the following chapter.

5.4.2 Data analysis

As a starting point, we check the evolution of the first dip position at various pump power levels. The PCF geometry has direct impact on the fiber dispersion, hence the position of first FWM dip. By monitoring the dip position at various pump power, we can deduce the condition of fiber geometry. We present the experimental data and simulation extracted for T-PCF4 in Fig. 5.17. The theoretical values for the 1st

dip/minima position can be estimated using Eqn. (2.27). Since we cannot monitor the T-PCF geometry during the experiment directly, tracking the evolution of 1st dip position is one alternate way to check the existence of the T-PCF's geometry variations. The 1st dip position follows perfectly with the simulation, indicating no dispersion variation as the pump power level increases. Thus, we conclude that no noticeable changes to the PCF geometry happen during testing, even at 6.65 MW/cm² intra-core pump intensity, as any changes would impact the dispersion of the fiber,

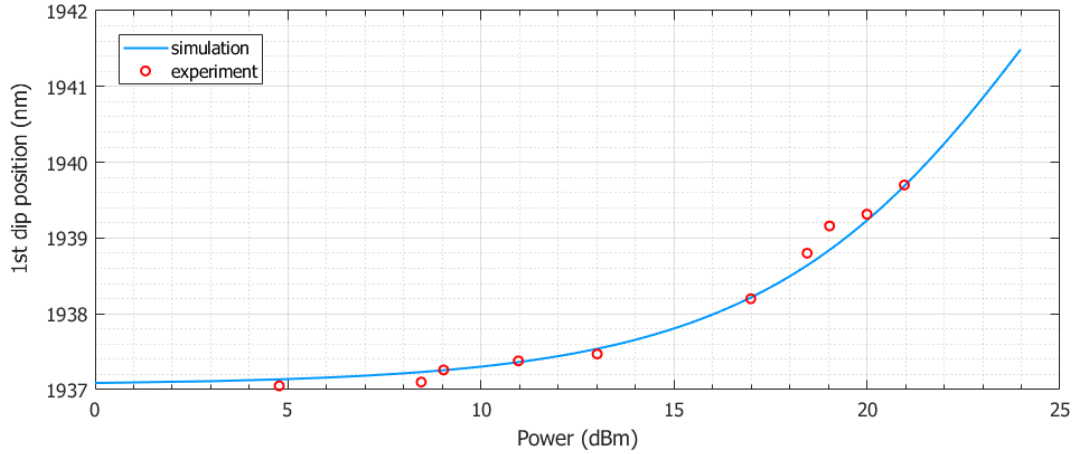


Figure 5.17. The simulation and experimental position of first dip. Perfect matching with the theory indicates that the fiber geometry remains intact at all pump power levels.

It is also important to confirm whether damage exists after the test performed at high power intensity to ensure no structural damage or loss increase. After all tests at 125 mW coupled pump power described in chapter 5.4.1, we inspected the facet of T-PCF4 using an optical microscope. No damage could be observed on either input or output facets. To check the waist dispersion, once again a way to quantify any changes to the PCF geometry, we performed an additional FWM experiment at low pump power level. For comparison, we also superimpose the test results before sending high intensity pump power, shown in Fig. 5.18. For both tests, we use only 3 mW of coupled pump power. The experimental data before and after the high-power test show perfect overlap and match well with the simulation. The small changes on the second and third lobes are due to the fiber birefringence and non-identical coupling conditions as the test were performed on different days. Thus, we can conclude that no structural changes or loss increase occurred during the high-power tests.

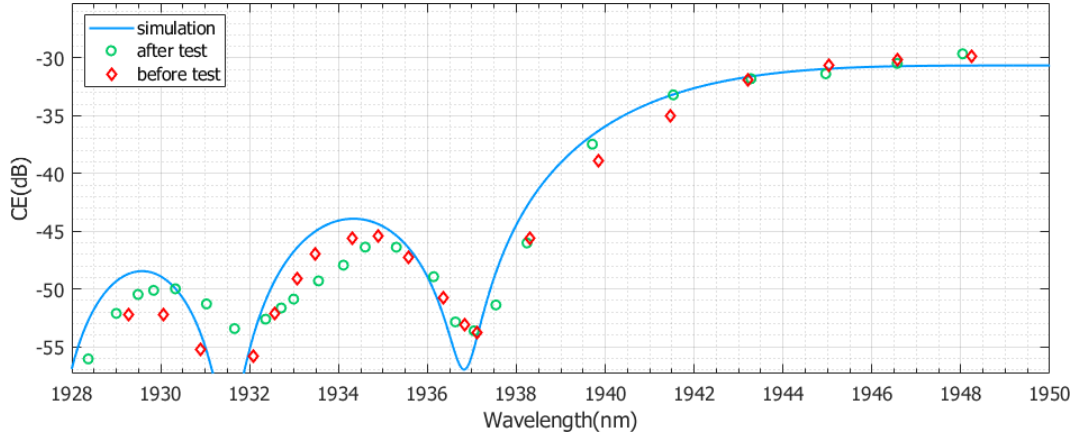


Figure 5.18. Low pump power characterizations before and after sending 125 mW of coupled power into T-PCF4. The small discrepancy is due to slightly different input polarization.

From Eqn. (2.23), we expect the CE to increase quadratically with the coupled pump power. This behaviour can also help us to exclude the contribution of other effects to the CE. To check the input-output characteristics of T-PCF4, we placed the signal laser at 1951.5 nm. Reading from the left y-axis of Fig. 5.19, one can see a linear relation between CE and coupled pump power in logarithm scale. A linear fitting gives a slope of 1.8, which is very close to 2. This small discrepancy is a combined result from cascaded FWM where idler light acts as a pump, the linear propagation loss that lowers the pump power during propagation, and SPM of pump laser that effectively lowers the pump power during propagation.

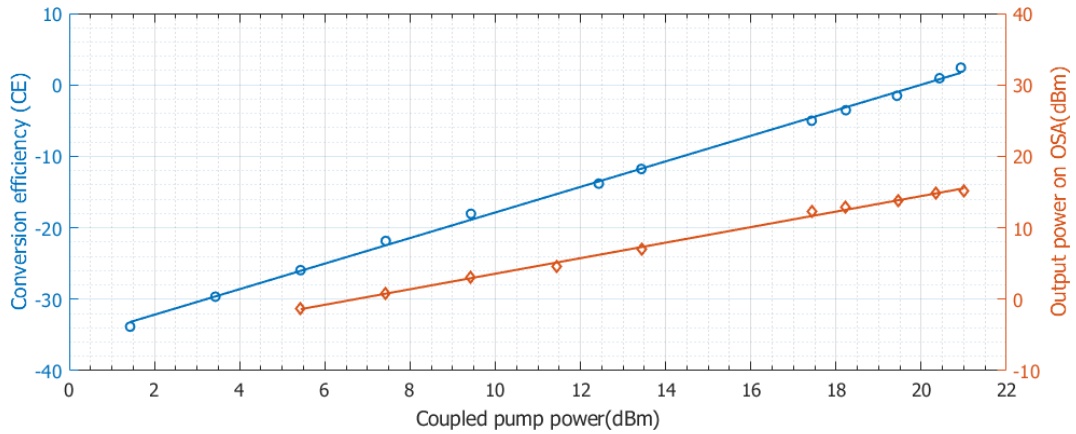


Figure 5.19. The CE and coupled pump power result in a slope of 2 linear fitting in log scale. This indicates the amplification comes from nonlinear parametric conversion. In addition, the output pump power follows linearly as input, showing good alignment and fiber transmission.

On the right y-axis of Fig. 5.19, we plot the input and output pump power relationship. The fitting gives a slope of 1, indicating a stable free-space coupling. Also, the slope of 1 implies no increase of fiber propagation loss during the operation.

Therefore, T-PCF4 can sustain at least 6.62 MW/cm^2 CW intra-core optical intensity at 1950 nm.

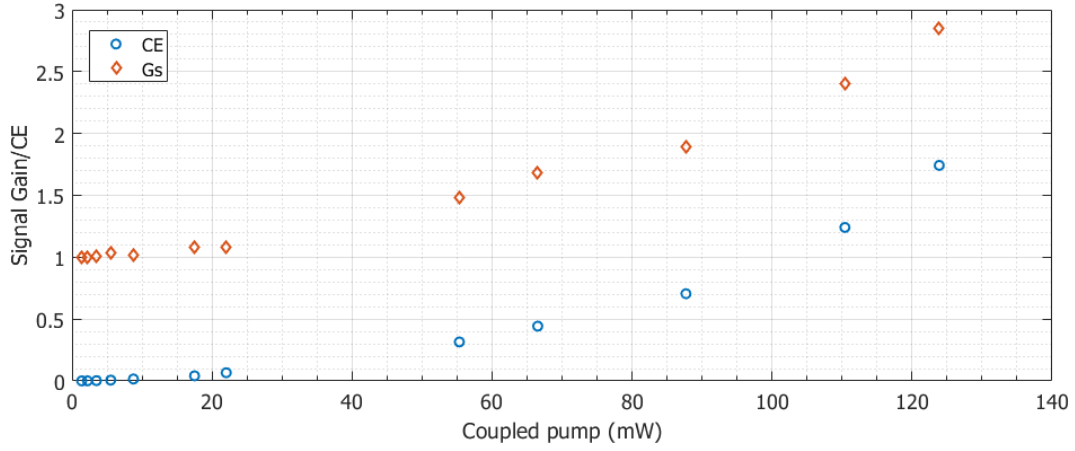


Figure 5.20. The relation between signal gain (G_s) and idler CE. The curves follow equation $G_s = CE + 1$ perfectly, which is another signature of nonlinear parametric conversion.

The relation between CE and signal gain should follow the relation of Eqn. (2.20) in linear scale. We show the experimental data in Fig. 5.20. Both the signal gain and CE follow a constant difference and same slope, which correlates well with the theory and shows no sign of saturation. Based on all the data, T-PCF4 clearly shows a parametric amplification process and is able to operate at very high intra-core optical intensity level.

5.4.3 Repeatability

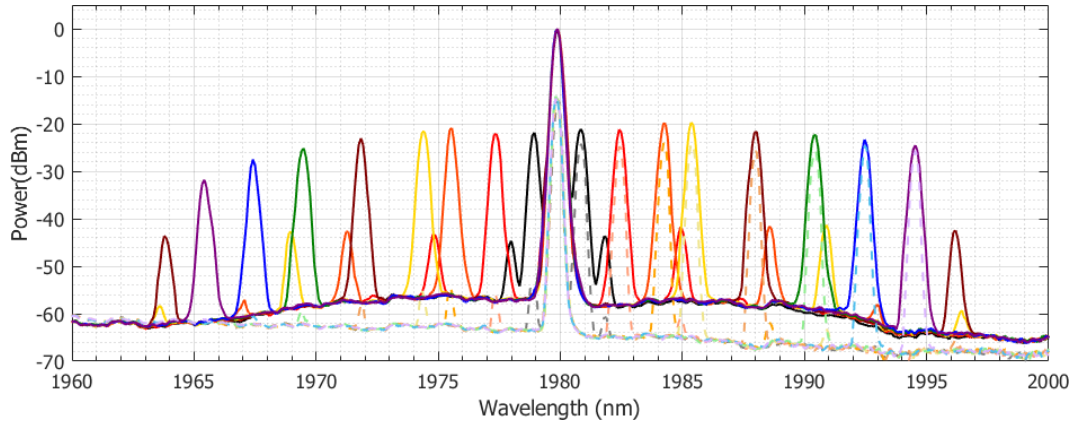


Figure 5.21. The spectrum recorded on OSA for T-PCF1. In this plot, the dashed colored signals are references. The pump power is lowered by more than 10 times, hence 100 times lower signal gain for these references.

For any experiment, it is critical to guarantee the repeatability of the result. We have performed similar set of tests on T-PCF1 and T-PCF3. With both T-PCFs, we recorded amplified parametric conversion with similar pump power levels. Particularly for T-

PCF1, the pump wavelength was set at 1980 nm instead of 1950 nm, showing that our result is not limited to a specific wavelength of operation. Actually, from the absorption of GeAsSe fiber [79], a longer pump wavelength will yield less loss and, thus, even better performance for parametric conversion. One of the OSA spectrum for T-PCF1 is displayed in Fig. 5.21, for pump wavelength of 1980 nm. Limited by the pump laser power, we managed to couple a maximum pump power of 207 mW. The signal power is approximately 1 mW. In this case, we have a maximum signal gain of about 5.2 dB and CE of 3.7 dB. The corresponding intra-core pump intensity is more than 11 MW/cm². We did not observe any damage to the T-PCF1 at this pump power over 1 hour of data recording.

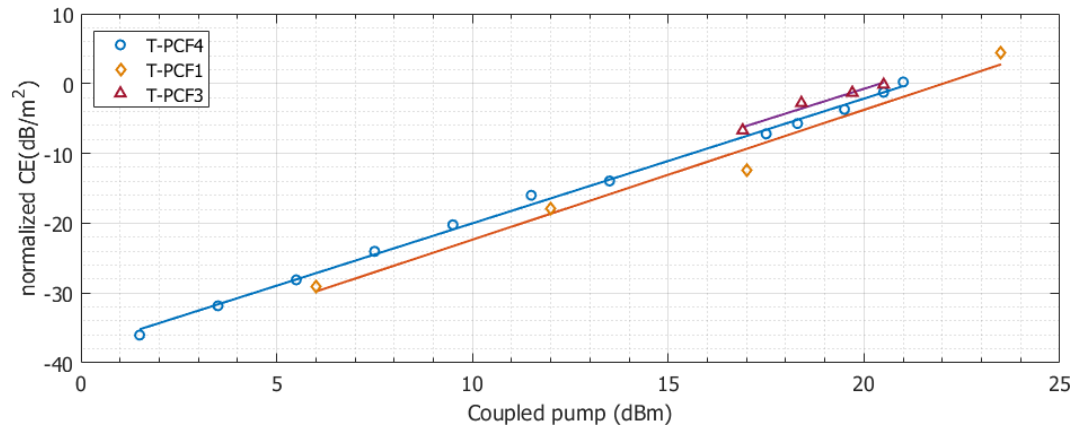


Figure 5.22. The CE normalized to fiber length for T-PCF1, 3 and 4. All the results have almost the same slope efficiency. The data for T-PCF1 is recorded with 1980 nm pump laser.

Since the three T-PCFs have different waist length, the CE over length squared is plotted as a function of coupled pump power in Fig. 5.22 for better comparison. Instead of a gradually increased pump power, we used different start pump power level for T-PCF3 and different step size for T-PCF1 to check different pump power increase schemes. All three T-PCFs follow the same slope of about 1.8. Clearly, we managed to couple much higher power into T-PCF1, leading to a higher maximum normalized CE. The discrepancy among the T-PCFs is due to slight difference of loss in the taper transition region. When we further increase the pump power for T-PCF3 and T-PCF4, the samples were damaged by fiber fuse – a catastrophic damage due to a localized defect, direct result of the extremely high intensity inside the taper. Thus, a better way to increase the CE or signal gain is to fabricate longer T-PCFs, reducing the required pump for highly efficient parametric process. Given the linear loss of 0.5 dB/m, the ChG T-PCFs have an effective length of 9 m. If a T-PCF of such length can be fabricated, one can reach 0 dB CE with no more than 15 mW.

5.4.4. Summary of all test results

We summarize the final test results and conditions after all the experiments on T-PCFs in table 5.2, which is an extended version of table 5.1. We have observed the first amplifier parametric conversion ($CE > 0$ dB) in T-PCF1. The maximum intra-core power intensity is more than 11 MW/cm^2 . T-PCF1 operated under such intensity level for more than 1 hour and no damage happened during the entire time. The maximum waist power intensity is only limited by our pump power. In T-PCF2, we have observed the first fiber fuse starting at the middle of taper waist at an intra-core pump intensity of close to 10 MW/cm^2 . The fiber fuse is likely due to the high environmental humidity during the test, which reached more than 80%. In both T-PCF3 and T-PCF4, we have observed more than 4 dB signal gain and about 3 dB CE. The starting point of fiber fuse for both fibers were found around the output transition regions. We have performed detailed study on these two fibers [165]. The results and findings will be stated in the last part of this chapter. The last taper, T-PCF5, has improved coating and tapering parameters. The fiber has only 4.8 dB insertion loss, measured at 2004 nm. However, the hole-period ratio requires longer pump wavelength to reach the ZDW.

Table 5.2 Data of FUTs in this experiment

	ρ	Insertion loss	Production date	Waist length	Notes
T-PCF1	0.58	9 dB	2015.12	0.8 m	$>11 \text{ MW/cm}^2$, no damage
T-PCF2	0.56~0.57	10 dB	2016.07	1 m	Fiber fuse in middle of waist
T-PCF3	0.56	8.5 dB	2016.07	1.12 m	Fiber fuse, signal gain
T-PCF4	0.58	8.5 dB	2016.09	1.2 m	Fiber fuse, signal gain
T-PCF5	0.57	5 dB	2017.01	1 m	Low loss, ~3 cm transition

Conclusion

In this chapter, we start with low power characterization of T-PCFs. Using low power FWM, we managed to retrieve the T-PCF uniformity and birefringence. Then, using increased pump power, we demonstrated the amplified parametric conversion under CW light at MIR band. To achieve this, we need a power intensity reaching the range of MW/cm^2 . In some T-PCFs, an optical discharge occurs and leads to catastrophic damage to the fibers (T-PCF2 to 4 in Table 5.2). In the next chapter, we will cover the studies on this damage effect.

Chapter 6

Fiber fuse in chalcogenide Photonic crystal fibers

6.1 Introduction

Fiber fuse – an optical discharge occurs at fiber core due to the thermal runaway at a localized defect – leads to irreversible and catastrophic damage to the optical fiber system. The induced plasma propagates backward to the pump source, where energy is provided, and leaves discrete voids inside fiber core. Since its first observation in the 1980s [166], many studies have been performed on this topic with both continuous-wave (CW) lasers and pulsed laser [72, 167]. An intensity threshold was found to be in orders of several MW/cm^2 with a propagation speed in orders of m/s [167]. Due to its severe threat to dense wavelength division multiplication system, fiber amplifiers and fiber laser systems, both characterization [168-171] and suppression methodologies [172-174], mostly limited to silica fiber networks, have been explored. However, study of such effects is mostly confined within silica fibers. For other fiber materials, fiber fuse in polymer fibers has also been observed in 2014 [175]. Another study performed in fluoride and As_2S_3 fibers claimed fiber fuse to be improbable in such fibers due to their low melting temperatures [71]. Thus, for a long time, it was believed that the destruction mechanism inside soft-glass fibers was purely thermal and distinct from fiber fuse in silica fibers [71, 176].

In recent years, the interest in mid-infrared (MIR) applications and compact MIR platforms has catalyzed the development of MIR fibers with novel materials and

structures as well as improved transmission [69]. Among them, Chalcogenide glass (ChG) fibers possess the largest transmission band, nonlinearity, and can be fabricated into suspended core [177] or photonic crystal fiber (PCF) [178] geometry for various applications. It followed that great efforts have been put into ChG fiber development and optimization. In terms of the ChG fiber platforms, breakthroughs in both CW and pulsed applications have been reported in the recent two years. For pulsed applications, all-fiber MIR optical parametric oscillator [157], parametric wavelength converter [61] and all-fiber MIR supercontinuum source [62] became feasible. For CW laser applications, advances in fabrication technology now allows for amplified parametric conversion in MIR [66], power delivery [109] and integration into the silica fiber network [70]. In CW applications, power intensities have exceeded 5 MW/cm^2 . Such values, orders of magnitude higher than what used to be believed feasible [69], are sufficient to ignite fiber fuse in silica fiber. At this early stage of research and development it is therefore important to look back into the possibility of fiber fuse in ChG fibers. In addition, fiber fuse inside a different material platform can provide more insights and lead to better understanding of the phenomenon.

In this chapter, we report the first observation of fiber fuse in non-silica fibers. Inside T-PCF3 and T-PCF4, fast backward propagating damages were observed at a lowest power intensity of 6.5 MW/cm^2 . The fiber fuse propagation speed is estimated to be larger than 0.6 m/s . Inspection with scanning electron microscope (SEM) and optical microscope revealed smooth, shallow and discrete voids inside fiber core region. We also polished a small segment of un-tapered region along its longitudinal axis and revealed the quasi-periodic nature of voids inside our ChG PCF. By a quick shutdown of pump laser, we managed to terminate fiber fuse and saved a 30-cm segment of tapered fiber. By performing a parametric conversion experiment, clear change of dispersion can be noticed. This is a result of decreased hole-period ratio, where hole size shrinks due to solidification of vaporized core material the walls. To our knowledge, this is also the first study on the impact of fiber fuse to the survived PCF segment, meaning suppression of fiber fuse in a PCF system is more challenging than traditional fibers.

6.2 Observation of fiber fuse

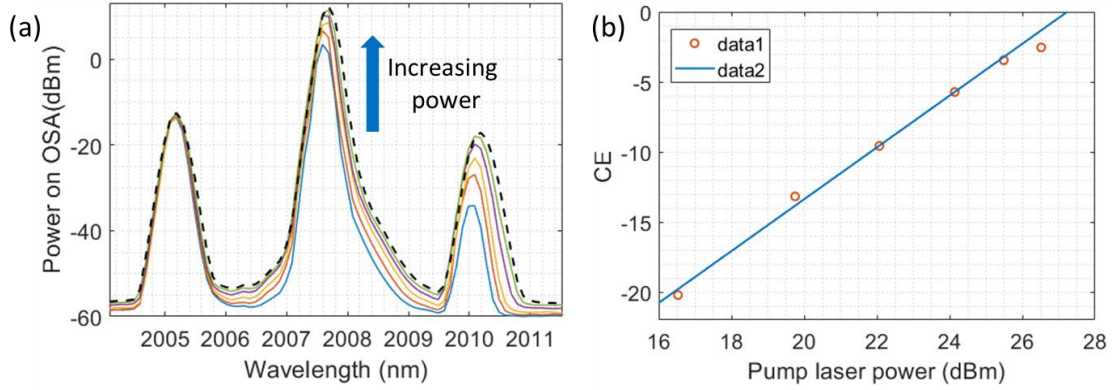


Figure 6.1. FWM power evolution before the onset of fiber fuse. (a) OSA traces recording increase of pump power values: 16.53 dBm, 19.75 dBm, 22.07 dBm, 24.14 dBm, 25.49 dBm, 26.52 dBm. (b) Retrieved CE in terms of pump laser output power. The fitting uses only the first five points.

Before going into detailed study of fiber fuse in ChG T-PCFs, it is helpful to check what happens right before the fiber fuse. We observed the first fiber fuse in T-PCF2 when increasing the pump laser power gradually towards 0 dB CE. We increased the pump power following: 16.53 dBm, 19.75 dBm, 22.07 dBm, 24.14 dBm, 25.49 dBm, 26.52 dBm, as illustrated in Fig. 6.1(a). By scaling the CE at 16.53 dBm pump, we expect to reach 0 dB CE with a pump laser power of approximately 27 dBm. However, when pump power increased from 25.49 dBm to 26.52 dBm, the CE does not follow the same increase. If we perform a linear fitting for the first five data points, we can notice a sudden offset on the sixth data point [increase of 0.7 dB instead of 2 dB, in Fig. 6.1(b)]. When further increase the pump power to 27.81 dBm, which proved to be safe to T-PCF1, the display on OSA suddenly went to zero. At this point, the intra-core power intensity is about 8.3 MW/cm^2 .

From the spectrum in Fig. 6.1 (a), no strong SPM effect occurred during experiment. In addition, the same cavity was used to get +0 dB CE in the old taper. Thus, it is not likely to be a problem of the fiber laser. Initially, due to previous beliefs, we failed to realize the damage came from a fiber fuse. Checking the fiber facets, we noticed the core was vaporized in both tapered and un-tapered region. It should be noticed the shape of the hole changes with the length and we noticed some periodicity. Also, at some point, the core seemed to be intact, but further test indicates existence of holes after this point. Thus, we have a damage that extend along the fiber, has some sort of periodicity and blast lots of fiber material out from the input end. After comparison with previous literatures [72, 167], the only phenomenon leading to this kind of damage is fiber fuse. With this initial knowledge in mind, we managed to perform more rigorous characterizations on fiber fuse in T-PCF3 and T-PCF4.

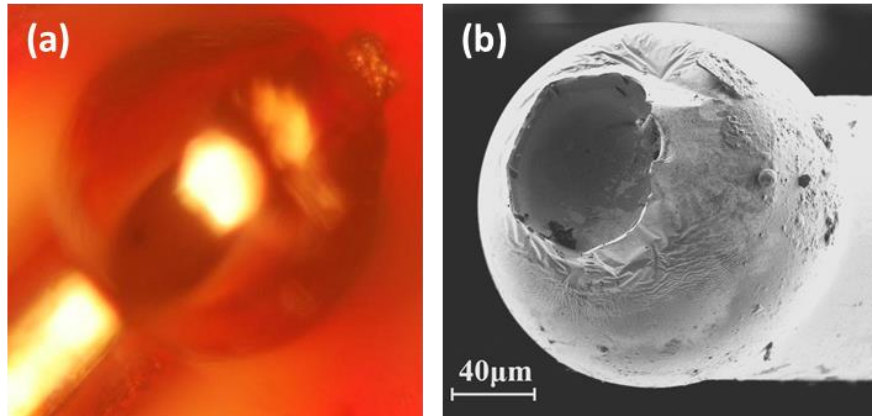


Figure 6.2. The top-view of T-PCF3 input after fiber fuse. (a) ball of Chalcogenide formed on the PCF input facet. Note high reflection from sphere surface; (b) SEM image of (a), the “crater” came from collision with lens fiber.

We gradually increased the 1950 nm pump power until the intensity in T-PCF3 waist reached about 6.5 MW/cm^2 . At this intensity the transmitted light abruptly dropped to zero, and the pump laser was shut down within 2 seconds. Inspection with the top-view microscope at the input side showed an input lensed fiber coated by ChG and formation of a smooth ChG ball on the T-PCF3 input as Fig. 6.2(a). Top-view inspection of the output side revealed no noticeable changes, indicating that the damage propagated backwards from an ignition point all the way back to the input where the core material blasted out. In Fig. 6.2(b), the SEM image shows a sphere on T-PCF3 input. The “crater” on the sphere results from collision with the input lensed fiber during the sphere formation. Formation of such sphere is an indication of fast thermal equilibrium process and discrete blast of ChG. Noticeably, core material blast from input facet is one of fiber fuse’s distinct features in contrast with other fiber damage mechanisms [72, 167].

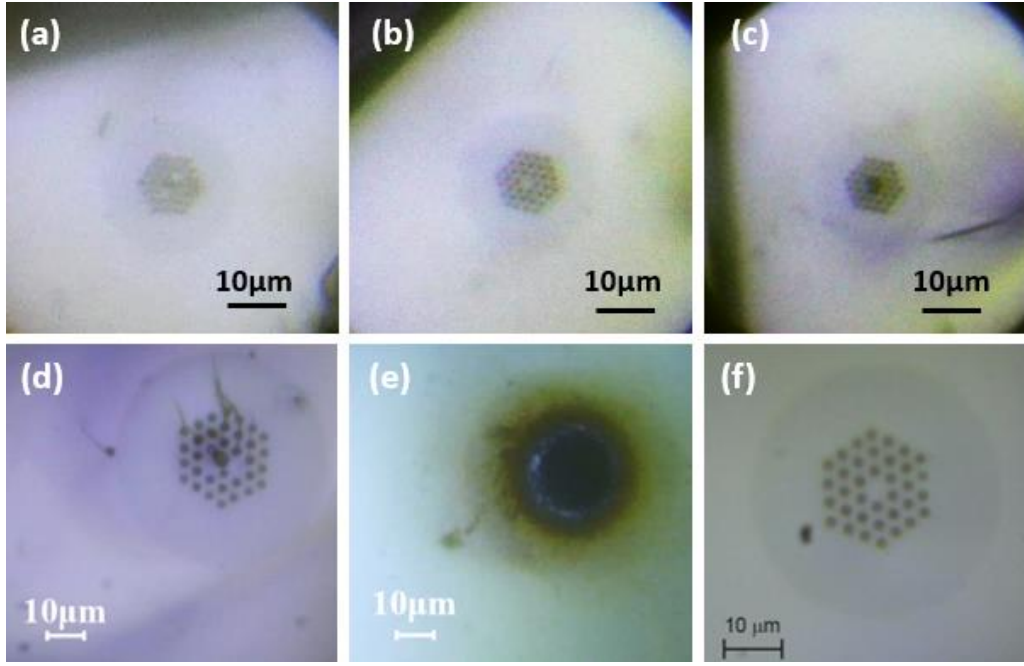


Figure 6.3. Optical images of damaged PCF facets. (a), (b) and (c). Optical image of T-PCF3 waist facets after fiber fuse cleaved continuously around the center of waist. The interval between each cleaving is about 1 cm. As a comparison with purely thermal damage, we show (d) Core void due to fiber fuse; (e) A purely thermal induced damage on input facet; (f) An intact facet

The rings of air holes inside T-PCF3 cladding prohibit us from a direct inspection of the core voids' geometry. One way to solve this issue is to cleave piecewise along T-PCF3 and image the facets. Given a proper cleaving step size, such method could also guide us close to the starting point of fiber fuse. Due to the large number of cleaves required, the optimal approach is to start with an optical microscope then move the most important samples to an SEM for better details. During the process, we noticed that voids exist in both taper waist and input un-tapered region. The optical images of three consecutive cleaved facet inside the waist region are shown in Fig. 6.3(a) to (c), respectively. Apparently, these voids in waist core have various geometry and are isolated. The smooth voids confined in the fiber core implies the hot point/damage must propagate faster than the thermal conduction speed in GeAsSe. Fiber fuse also managed to travel through the input un-tapered region [Fig. 6.3(d)]. Thus, while the fuse ignited at 6.5 MW/cm^2 in T-PCF3, its propagation was maintained after the intensity dropped to 1 MW/cm^2 . Facet damage from fiber fuse differs significantly from a purely thermally induced facet damage, shown in Fig 6.3(e). For comparison, an intact fiber facet is included in Fig. 6.3(f).

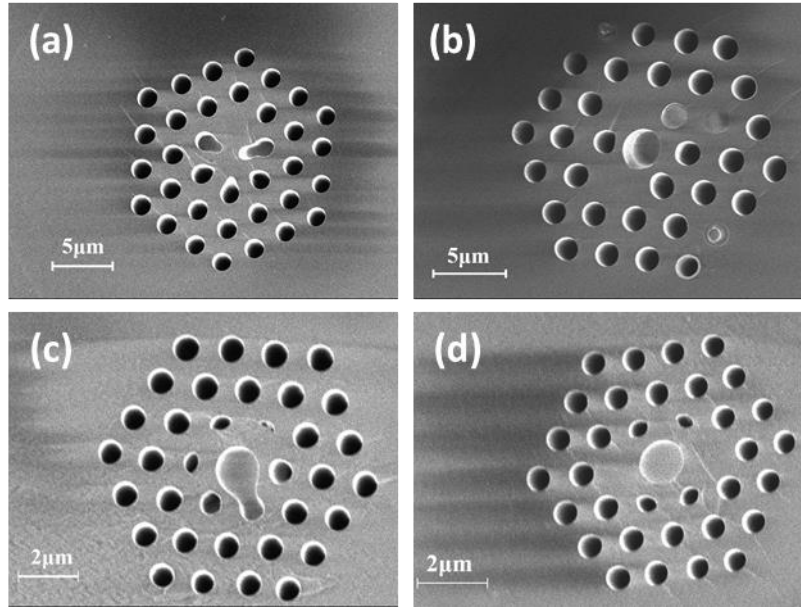


Figure 6.4. SEM images of T-PCF3 at various locations. (a) SEM image of a facet on output transition region of T-PCF3, close to the start point of fiber fuse; (b) SEM image of the facet from Fig 6.24(d); (c) and (d) SEM image of two facets inside the taper waist, separated by about 10 μm ; shallow bottoms can be seen by using the in-lens detector.

The cleaving was performed from fiber input until the output taper transition region. Voids were observed along the whole fiber until the transition region on output side. The un-tapered PCF after the transition region has the same transmission as an intact fiber. Thus, we can conclude that fiber fuse started around the taper transition region at output side. We imaged a facet at this region with a Zeiss Merlin SEM and observed clear footprint of fiber fuse [Fig 6.4(a)]. A facet from input un-tapered region was also imaged as shown in Fig 6.4(b), corresponding to the facet shown in Fig. 6.3(d). The SEM in-lens detector allows us to check the existence of the voids bottom. In Fig. 6.4(c) and (d), facets from the taper waist were recorded together with the voids' bottoms. Like fiber fuse in silica, voids in GeAsSe PCF are also isolated. In Fig. 6.4, it can be noticed that some air holes were filled by re-solidification of vaporized ChG [particularly Fig. 6.4(b) and (d)] while the fuse voids were well-confined within the core region. After the formation of voids, high temperature ChG managed to burn its way into the air holes then propagated a certain length and re-solidified along the holes during certain length of propagation.

Rather than examining the T-PCF3 with near or mid-infrared light, “opening” the fiber is most reliable way to check the voids' period and fuse impact on the air holes. Due to the small dimension of the taper waist, polishing can only be performed on the input un-tapered segment. A 6 mm segment of un-tapered region was glued onto a holder and the whole polishing setup was illustrated in Fig 6.5(a). This holder assembly

was mounted on a vertical linear translation stage. Polishing films have grain size from 6 to 0.02 μm . We monitored the polishing process in real-time. The polishing angle is indicated in Fig. 6.5(b).

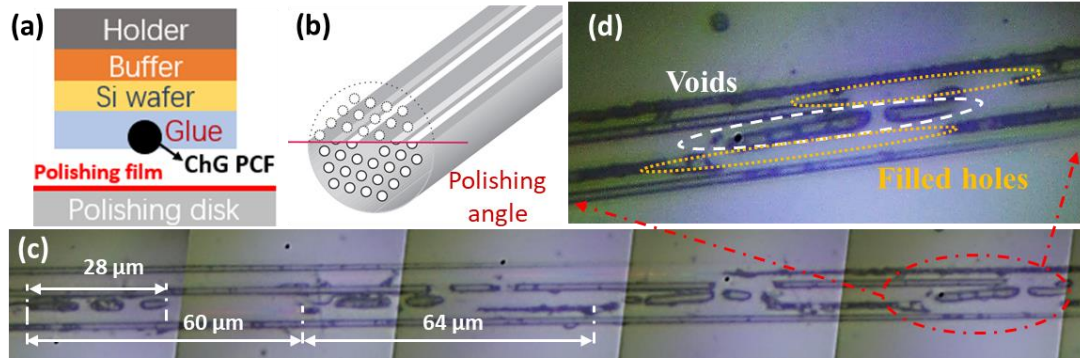


Figure 6.5. The setup for “opening” T-PCF3 and the images from fused region. (a) Sketch of the polishing assembly; (b) The polishing angle of the segment; (c) Composed image of the “opened” fiber. Note the clear periodicity of voids; (d) Enlarged image of voids’ top-view.

We imaged the top-view of the polished segment with a 100X long working distance objective. Figure 6.5(c) is composed of five successive images. Fiber core is placed in the middle of image and isolated voids from fiber fuse are well-confined to the core. The voids period/interval is around 60 μm . Each period contains three smaller voids, which has a total length of 28 μm . Zooming in Figure 6.5(d), one can also notice the filled air holes close to the voids. We would also like to emphasise that the images in Figure 6 came from the un-tapered region where light intensity is about 1 MW/cm^2 . Since the intensity in taper waist of T-PCF1 region is 6.5 MW/cm^2 , the voids size and period/interval can be different.

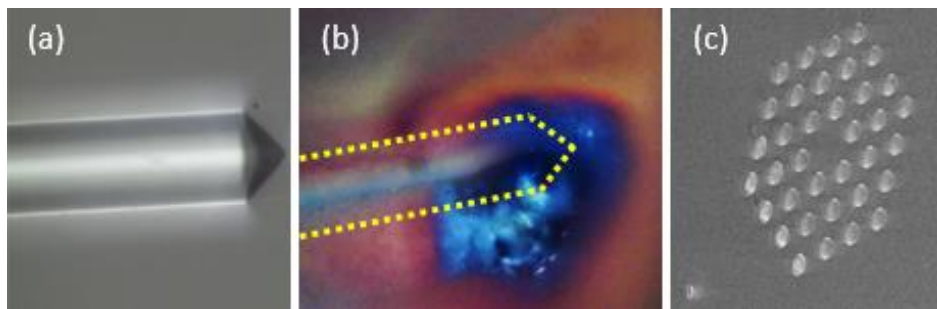


Figure 6.6. Top-view of the input side from T-PCF4. (a) Input lens fiber before fuse happened; (b) Input lensed fiber coated by ChG after fiber fuse; lensed fiber is out of focus to better image the deposited ChG; (c) SEM image of the input facet of T-PCF2, showing no trace of damage on this facet.

T-PCF4 has a waist length of 1.2 m and was fabricated from the same fiber spool as T-PCF3. Fiber fuse happened at a waist power intensity of 7.5 MW/cm^2 . As with taper 1, input lens fiber and ChG PCF input facet were inspected with microscope. In

Fig. 6.6(a) and (b), though the lens fiber was deposited with ChG, the ChG PCF input facet is intact under SEM [Fig. 6.6(c)]. Further investigation confirmed that we managed to stop fiber fuse before it traveled through the whole fiber. A 28-cm taper waist segment was saved. With the propagation length fixed, we can estimate a transmission speed of at least 0.5 m/s, which is in the same order of magnitude as the fuse propagation speed in silica fibers [167] and orders of magnitude higher than the reported thermal damage speed in AsS fiber [71].

Although this 28 cm piece showed the same propagation loss as the original GeAsSe T-PCF2 (0.5 dB/m), the large amount of deposited ChG on the input lensed fiber does raise concerns about its properties. As ChG vapor made its way to the input lensed fiber, it could have condensed and deposited on the walls of the air holes, hence effectively reducing the hole-period ratio – an effect that would also apply to silica PCF. However, to our knowledge, fiber fuse’s impact on properties of remained/survived PCF has yet to be reported.

6.3 Impact beyond fiber fused region

In Fig. 6.7(a), we show the experiment measured parametric conversion trace for 1980 nm pump. Clear dips appeared on the recorded spectrum, indicating good fiber uniformity and low loss. The CE feature matches perfectly with the simulation of a 0.56 hole-period ratio taper. Measurements with several different pump wavelengths [figure 6.7(b)] confirms the estimated hole-period ratio.

Same experiment was also performed before fiber fuse on taper 2 at 1950 nm. The calculated dispersion corresponded to a hole-period ratio of 0.58. In Fig. 6.7(b), we put measured data from another taper of same geometry and simulated dispersion for better comparison. The dispersion difference before and after fiber fuse is significant. To exclude temperature and birefringence influences, we performed two extra tests. Parametric conversion performed at 7 °C showed no change on retrieved dispersion. Rotation of input lens fiber showed hole-period change within 2%, in accordance with our previous work [66]. Therefore, we conclude that the ChG vapor travelled in air holes uniformly deposited on their wall, hence effectively shrinking air hole size.

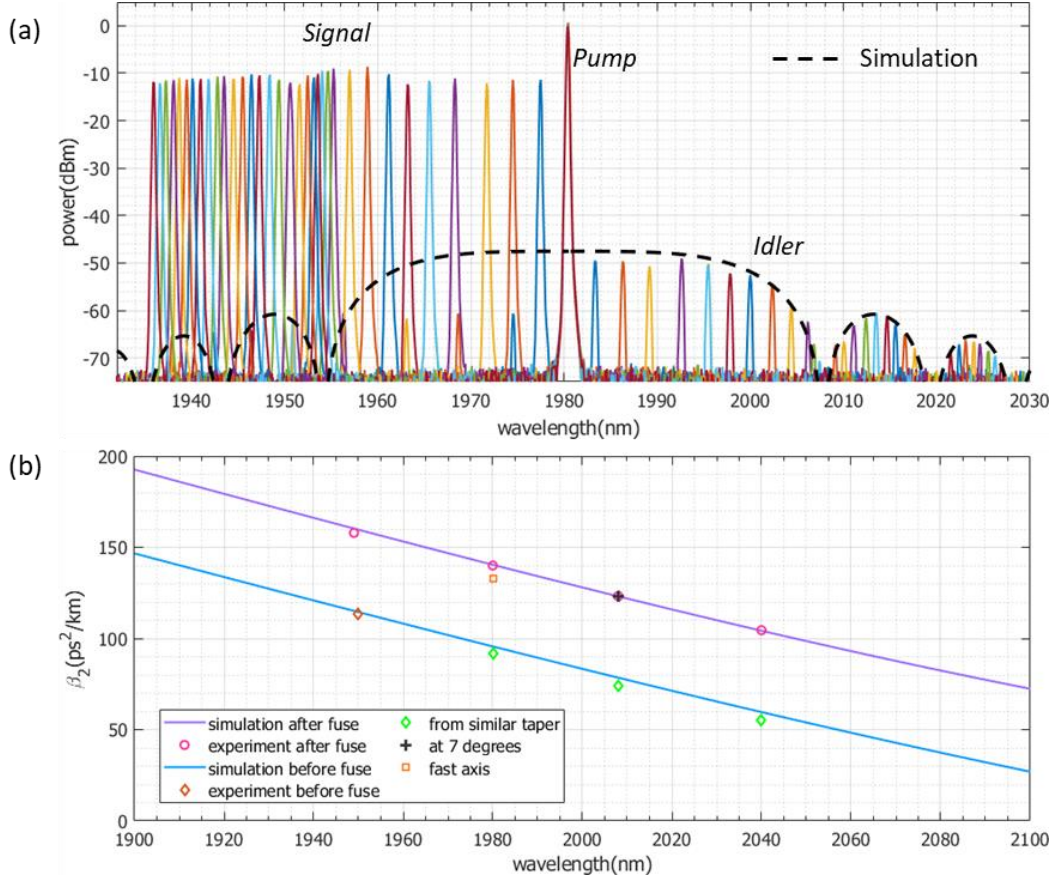


Figure 6.7. FWM characterization of the leftover part from T-PCF4. (a) Superimposed spectrum of signal sweep with theoretical fitting from Eq. (2), about 5 mW pump and 0.3 mW signal power coupled into fiber; (b) Comparison of dispersion before and after fuse.

Conclusion

In conclusion, we observed first fiber fuse in non-silica fibers and characterized its effect on the remaining ChG PCF. We also noticed one of the samples, T-PCF1, was tested under 11 MW/cm² with no damage. Thus, we believe a better coating process and improved fabrication can push the power handling of ChG PCF further.

Chapter 7

Linearly chirped supercontinuum generation

7.1 Introduction

When an optical pulse experiences strong spectrum broadening inside a nonlinear medium, people normally refer to this phenomenon as supercontinuum generation (SCG). SCG inside photonic crystal fibers (PCFs) has been exhaustively studied and has found applications in various areas [88, 179]. Silica PCFs have led to impressive performance for supercontinuum generation in the visible and near infrared bands. To reach longer wavelength, towards the mid-infrared (MIR) where many molecular bonds have fundamental vibration frequencies, novel fiber materials and geometries have been investigated over the last few years. Soft glasses are characterized by a low phonon energy, hence showing good transmission in longer wavelength. Fluoride [114], telluride [180] and chalcogenide glasses (ChG) [181-183] are the main candidates for MIR SCG in optical fibers. Among them, ChG has the largest nonlinearity and a suitable viscosity for producing low loss fibers [69], making it the ideal material for MIR fibers. In fact, the first SCG covering the complete molecular fingerprint region was demonstrated inside a ChG fiber in 2014 [183]. Later, researchers demonstrated multi-milliwatt SCG inside tapered ChG PCFs [161].

The spectrum broadening mechanism of SCG is highly dependent on the pump wavelength domain. The origin of pulse evolution for normal dispersion and anomalous dispersion pumping can be very distinct from each other. For anomalous dispersion pumping schemes, spectrum broadening is dominated by soliton dynamics and modulation instability. However, soliton dynamics are highly sensitive to the input laser

shot noise, leading to complex temporal profile, shot-to-shot fluctuation and degraded coherence [88, 184]. In the time domain, soliton fission breaks the SCG into multiple pulses, causing different arrival times. This problem could be greatly suppressed by pumping with sub-100fs pulses at proper wavelength and using short fiber length (less than a few cm), hence compression of the SCG to few-cycle pulses could be possible [185]. For single-pulsed, highly coherent, stable and re-compressible supercontinuum, researchers also revisited the use of all-normal dispersion (ANDi) fibers for SCG – the idea of ultrashort pulse generation by self-phase modulation (SPM) dating back to 1984 [186]. Indeed, numerical simulations demonstrated that SPM and optical wave breaking (OWB) dominate such ANDi SCG [91, 92]. Also, ANDi SCG typically has an ultra-flat top in frequency domain [92], supporting a shorter pulse duration.

The availability of highly nonlinear silica PCF allows for the study of ANDi SCG at moderate pump power and provides more freedom for dispersion engineering. A.M. Heidt, et al. demonstrated the single-pulse property of ANDi SCG theoretically and experimentally [187]. Since SPM and OWB induce linear chirp while preserving single-pulse property, compression of ANDi SCG pulse is feasible [90, 92]. In the same year, L. E. Hooper, et al. demonstrated ANDi SCG and experimentally compressed the SCG to 20 fs using a set of prisms from a 420 fs input pulse [188]. Later, A.M. Heidt., et al. compressed their ANDi SCG from 15 fs pump pulse down to 5 fs (sub-2 optical cycles) with chirped mirrors [189]. Simulations from this work also showed the possibility to achieve single cycle pulse, but a careful selection of the fiber and pump parameters must be carried out. Details about this selection will be discussed later particularly for ChG PCF SCG.

While both silica and silicate PCF ANDi SCG can reach $\sim 2.3\mu\text{m}$ [190, 191], pushing ANDi SCG further towards the MIR requires better transparency. As such, in recent years broad MIR ANDi SCG was demonstrated in ChG tapered step-index fibers [177], and ChG microstructured fibers [62, 192]. However, for applications like spectroscopy or pulse re-compression, SCG with improved flatness is advantageous. Particularly, efficient pulse re-compression requires not only a large 3-dB bandwidth, but also preferably linear group velocity dispersion (GVD). In addition, pumping with a fiber laser can lead to more compact and robust setups. To such end, a large nonlinear parameter is beneficial, so that efficient broadening can occur at moderate peak power provided directly from a fiber laser. A combination of ChG with a PCF structure, to not only increase nonlinearity but also correctly shape the dispersion, would satisfy such requirements and greatly benefit the SCG bandwidth, flatness and efficiency.

As mentioned, there are many MIR ANDi SCG demonstrations using multiple types of soft glasses, including ChG. Besides the limited 3 dB bandwidth obtained from previous studies, their numerical simulation and experimental results have room for further improvements [62, 177, 191]. This is either due to the incomplete characterization of free-space components dispersion or nonlinear fibers. Therefore, we believe there is a necessity to perform a more rigorous and complete study to prove that ChG PCF as a good candidate for ANDi SCG. The perfect matching between simulations and experimental data also serves as a proof that the process is completely deterministic. Besides, the use of a fiber laser instead of an OPO/OPA is an important step towards a more compact and robust all-fiber system.

In this chapter, we show the results from ANDi SCG on an un-tapered ChG PCF to utilize its linear and positive GVD. The chapter begins with a description of the experimental setup and pump laser characteristics. We then show the recorded SCG, impact of water absorption and spectrum stability of the ANDi SCG. Using NLSE, we show a good matching between theory and experiment. Calculations indicate a linearly chirped pulse at the output and a GDD compression allows for sub 20 fs pulse. Then, we design a tapered PCF for generation of an octave spanning SCG. At the end, we simulate the ANDi SCG span under various pump durations.

7.2 Experimental setup and fiber parameters

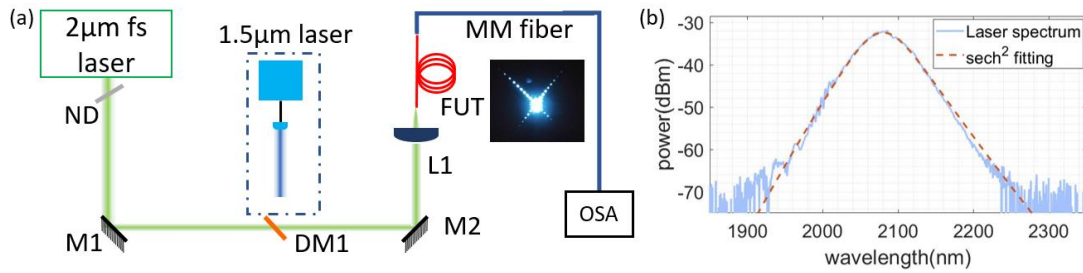


Figure 7.1. The experimental setup and pump laser spectrum. (a) Experimental setup. M1&M2: un-protected gold coated mirrors; DM: Dichroic mirror, high reflection for 1500~1750 nm and high transmission for 1850~2100nm; NA: neutral density filter; L1: aspherical lens; FUT: fiber under test; inset: far-field image once coupled into FUT core (b) 2080 nm pump spectrum and fitting using sech^2 function.

Fig.7.1 (a) sketches the experimental setup for supercontinuum generation. We used a commercial femtosecond laser utilizing Raman soliton self-frequency shift as the pump. This pump laser is thus tunable from 2050 to 2100 nm, with a repetition rate of 19.03 MHz. The collimated output beam has a diameter of 4 mm. For our experiment, 2070 and 2080 nm wavelengths are used, where pulse duration directly out of the laser is

measured to be approximately 79 fs for both wavelengths. Since the laser output is a 1st order soliton, we use a sech^2 function to simulate the input pulse, as demonstrated in Fig.7.1 (b). A reflective continuous variable neutral density (ND) filter positioned at the output of the laser enables smooth tuning of the pump power. The dichroic mirror (DM) reflects a low power 1.55 μm C-band continuous-wave laser to the same beam path as the 2 μm pump laser. The initial alignment is thus performed with the C-band laser to get a far field diffraction pattern on the infrared camera as seen in the inset of Fig. 7.1(a), while the pump laser is blocked after ND. Then we switch off the C-band laser and perform final adjustments with the 2 μm pump laser attenuated to 0 dBm. A 100 μm core-sized InF_3 multi-mode (MM) fiber collects the output from fiber-under-test (FUT). An MIR optical spectrum analyzer (OSA), Yokogawa AQ 6736 covering 1.5 μm to 3.4 μm , records the output spectrum.

Two single-mode PCFs with identical 4 μm core size but slightly different air-hole sizes were tested for SCG in this experiment. Six segments of these PCFs, further referred to as fiber under test (FUT) 1 to 6 were tested. All FUTs, except for FUT2, have a hole-pitch ratio of 0.58 [Fig.2 (a)]. For FUT2, the hole-pitch ratio is 0.49, as the segment comes from a different preform which has been previously drawn. Since the pumping wavelength is far from the zero dispersion wavelength (ZDW) as seen in Fig.2 (b) where the theoretical dispersion as a function of wavelength for the two geometries is plotted, the dispersion parameter for all FUTs are very close – around 360 ps^2/km . The dispersion of all FUTs is simulated using the commercial finite element method COMSOL software package. To confirm the simulation, dispersion of FUT1 was measured by a low-coherence interferometry method [154]. From Fig.7.2(b), we can conclude that the simulation matches well with the measured dispersion and FUT1 is ANDi until approximately 2.87 μm , owing to the strong material dispersion [green curve in Fig. 2(b)].

Table 7.1. Data of FUTs in this experiment

	ρ	$\Phi(\mu\text{m})$	α (dB/m)	γ ($\text{W}^{-1}\text{m}^{-1}$)	Production date	Storage
FUT1, 3 -6	0.58	4	0.6	1.7	2015.12	Dry air (<30% relative humidity)
FUT2	0.49	4	0.6	1.7	2014.12	Lab atmosphere

Since FUT2 has been stored in normal atmosphere condition for 3 years, we expect strong water absorption. On the contrary, all other FUTs were fabricated within 2 years from the same preform and stored in dry air with silica gels. The nonlinear parameter γ is approximately 1.7 (Wm)⁻¹ for all FUTs at 2080 nm, estimated based on our past

experiments [66, 67]. The input coupling loss is 7 ± 1 dB, where the uncertainty comes from the mounting angle and cleaving quality of the FUTs. In terms of the linear propagation loss, all FUTs show less than 0.7 dB/m at 2004 nm. We summarise the FUT data in table 7.1.

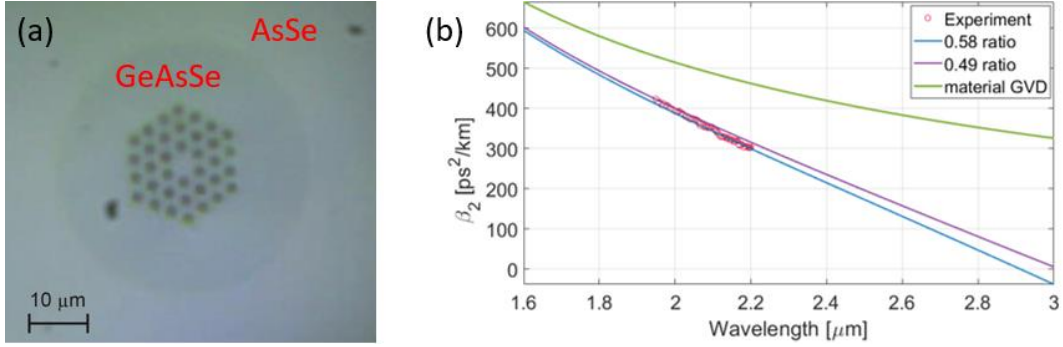


Figure 7.2. PCF facet and dispersion. (a) Manually cleaved fiber facet; (b) Simulated and experimental fiber GVD; the material GeAsSe has ZDW at about 7 μm

During our experiment, we increased average pump power gradually from 0 dBm to a maximum of 15 dBm in 1 dB steps, corresponding to a maximum coupled peak power of 2.9 kW. All data presented here were recorded under high sensitivity with chopper mode (“Hi/CHOP1”) of the OSA at 1 nm resolution. We used the GNLSE to study the SCG evolution with respect to pump power and propagation length. Due to the short fiber length and small propagation loss, the linear loss term is excluded in the simulation. In addition, as we pump far from strong two-photon-absorption (TPA) region [84], we also ignore the TPA term in the simulation. Due to the short pulse duration, we include the optical shock term in the same manner as [88]. Finally, we use COMSOL to simulate the frequency dependent effective area. This frequency dependent effective area leads to a frequency dependent nonlinear parameter, like the method in [92]. Instead of a constant nonlinear parameter, we used this array of nonlinear parameters in our GNLSE simulation. As ANDi SCG is a coherent and deterministic process, one should expect a good match between the theoretical prediction and experimental result.

7.3 Results and analysis

7.3.1 Preliminary tests at 2070nm with cm-long PCFs

For preliminary test of the ANDi SCG, we used FUT1 with 10 cm length to study the PCF performance and accuracy of our simulations. ANDi SCG pumped with femtosecond pulses typically has millimeter-scale effective length for spectrum broadening [177, 187, 188, 191]. We selected a relatively long length to ease the handling of the fiber and coupling, and to neglect the dispersion contribution from other free-space components. For all measurements in chapter 7.3, we fixed the pump wavelength at 2070 nm, with a possible maximum coupled peak power of 1.9 kW. We derived the coupled peak power through the coupled average power into the FUTs.

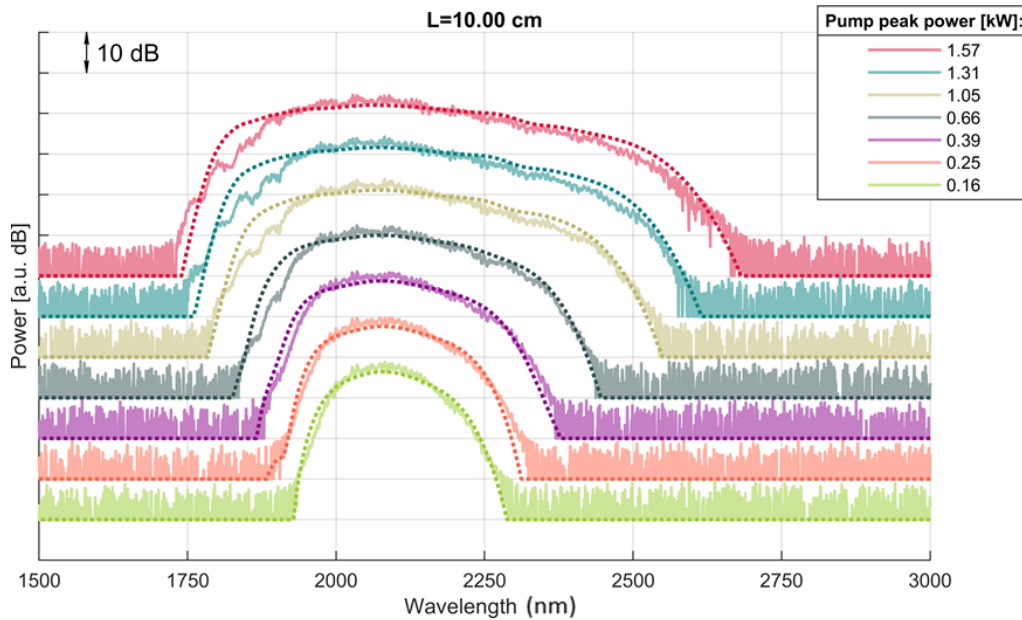


Figure 7.3. SCG at different peak powers for FUT 1 (solid line), and the corresponding simulations (dashed line). Lines at different peak power levels are shifted by 10 dB for better representability

The solid lines in Fig. 7.3 are experimentally recorded data at different pump powers. From now on, to better illustrate the spectrums, we shift each curve in the plot by 10 dB. At the maximum peak power of 1.9 kW, we measure a -20 dB bandwidth from 1.7 to 2.7 μm . We do not detect any water absorption dip, meaning a dry atmosphere is sufficient to properly store ChG fibers. Water in the air inside the OSA causes the absorption lines observed between 2500 nm to 2800 nm. As expected from previous research [91, 92], the ANDi SCG shows very flat top, leading to a large 3 dB bandwidth. Indeed, our 3 dB bandwidth covers from 1941 nm to 2301 nm (24 THz),

hence in theory can be compressed to few-cycle pulses. The dominant broadening mechanisms, SPM and OWB, are both elastic processes, resulting in a full conversion of pump power into the SCG. We measured 2.5 mW output average power, which is smaller than coupled average power owing to 20% loss from Fresnel reflection at the output facet. Further increase of average output power could be achieved by increasing the pump repetition rate, while keeping the peak power at a moderate value (a few kW).

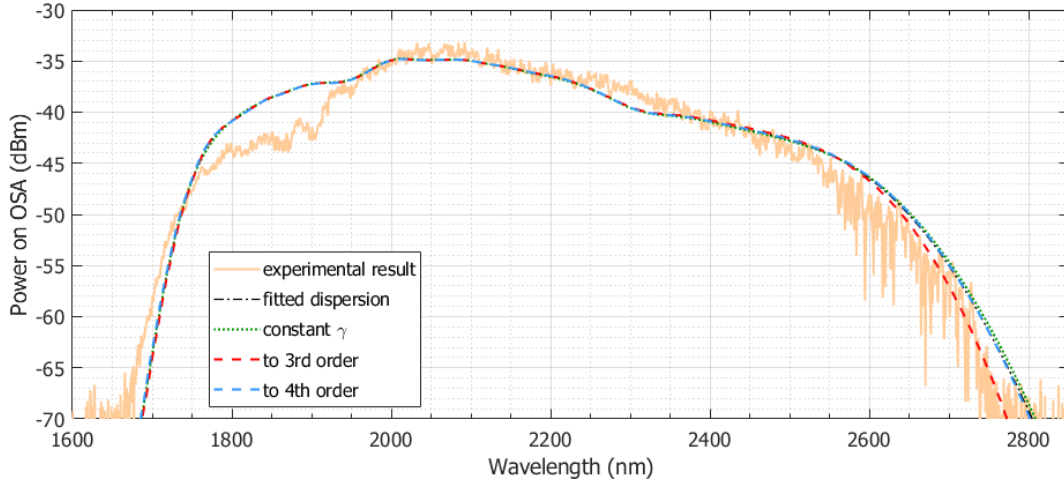


Figure 7.4. The experiment recorded SCG spectrum with simulations under multiple approximations.

We then take a closer look at the experimental result and simulation at the maximum pump peak power of 1.9 kW (Fig.7.4). Though the wavelength dependent effective area should lead to a different nonlinear parameter for the SCG band, we did not notice this impact from our simulation. A.M.Heidt has reported similar observation in his research [187]. For the newly generated frequency components, they require time to acquire the corresponding effective areas. In an ANDi SCG process, however, the pulse revolution is very rapid in both time and spectrum domain. As a result, we did not notice impact of wavelength dependence of nonlinear parameter. On the other hand, the simulation indicates that using up to 4th order of dispersion term already provides highly precise simulations. The small offset between simulation using either up to the 3rd or the 4th order dispersion terms indicates the wavelength where 4th order dispersion starts to be nontrivial.

For the theoretical study of our ANDi SCG, we have ignored the delay contribution from our dichroic mirror (DM) and chalcogenide lens, and the results are depicted by the dotted lines in Fig.7.3. As the length of FUT1, 10 cm, has a much stronger dispersion contribution than the DM and aspherical lens, the simplification is valid for this particular experiment. During the whole simulation process, we only adjust the

pump peak power according to the recorded average power to fit the experimental results. Generally, a SCG simulation are based on the mean of multiple runs [88]. ANDi SCG has perfect coherence and maximum phase stability [92, 188-190], so in this case only a single run of simulation is sufficient [189]. In section 7.3, we perform the study of pulse evolution during propagation with the dispersion contribution from optical components is also included.

7.3.2 Study of SCG stability and environment sensitivity

From the dispersion in Fig. 7.2(b), FUT2 is expected to produce slightly narrower SCG given the larger GVD of $368 \text{ ps}^2/\text{km}$ at 2070 nm pump. In addition, FUT2 was fabricated more than 3 years ago and stored in lab atmosphere without humidity control. Therefore, this fiber can serve as a good example to study water absorption impact on ANDi SCG under a normal atmospheric/environmental condition, which is critical for field applications. ANDi SCG in our FUTs have millimeter scale effective lengths, so a longer fiber length will not contribute to further broadening of the SCG. However, a longer fiber length can enhance the impact of water absorption and a 80-cm-long fiber was therefore tested in the same setup as depicted before. Compared to the experiments performed with FUT, the coupling loss only slightly varied ($<1 \text{ dB}$) while no difference in the linear transmission loss at 2070 nm were observed .

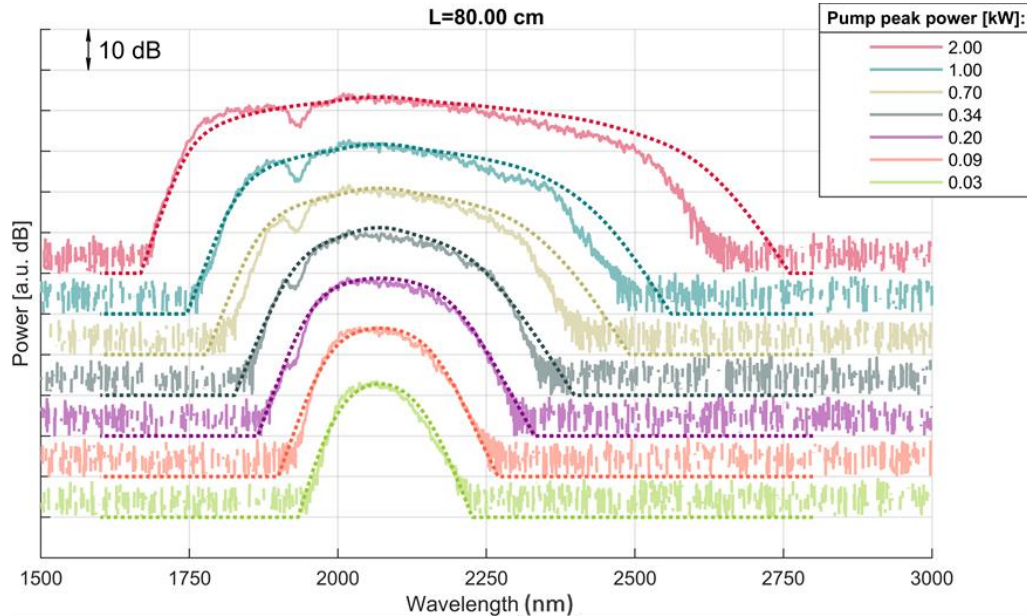


Figure 7.5. SCG at different peak powers for FUT2 (solid line), and the corresponding simulations (dashed line). Data shows clear trace of O-H bond absorption.

Fig. 7.5 shows the recorded SCG spectra (solid lines) together with simulation in the absence of water absorption (dashed lines) at different pump powers. Before the blue edge of SCG reaches 1950 nm band, simulation matches perfectly with experimental data. When we further increase the coupled peak power to 200 W, a clear dip appears at about 1935 nm, associated with the O-H bond vibration. Subtracted from the simulation, FUT2 has an absorption peak of 7 dB/m at around 1935 nm. Previous research shows more significant absorption peak should be expected centered at 2800 nm (3575 cm^{-1}), fundamental vibration frequency of O-H bond), which strongly hinders the expansion of our SCG expansion towards longer wavelength at higher pump power.

We believe the water absorption mainly comes from moisture inside atmosphere. The wet air travels through the PCF air holes and brings water to PCF core. One solution to avoid water absorption is to close the air holes or purge PCF with dry air. On the other hand, results from FUT1 shows no water absorption feature, meaning a dry atmosphere storage condition can well protect the fiber for at least two years. In addition, drying the sample inside a vacuum oven could remove the water from ChG [193], but may need more investigations.

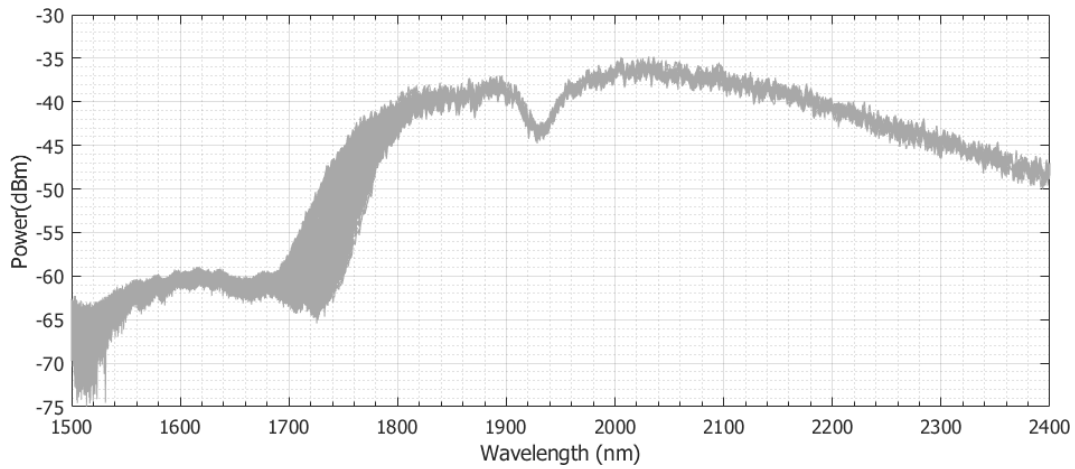


Figure 7.6. Superimposed SCG spectrum for FUT2. The figure consists of 700 traces taken in 40 minutes.

In addition to the environmental stability, it is important to demonstrate that the ANDi SCG is spectrally stable over time. We assess the long term ANDi SCG stability using the Yokogawa AQ 6375 OSA, which features a faster sweep speed and higher sensitivity than AQ 6376. However, the AQ 6375 has a wavelength coverage up to 2400 nm. During 40 minutes of monitoring time, the OSA recorded over 700 traces under normal sensitivity with a resolution of 2 nm. The shaded region of Fig. 7.6 shows the superimposed data of 700 traces, recorded on FUT2, confirming the good stability of the ANDi SCG. The spectral instability comes from coupling fluctuations. Since our

pump laser and FUT setup are on two separate optical tables, the unlocked mechanical vibration is the main contribution to this issue.

7.3.3 SCG evolution and pulse properties

For very short fiber lengths, optical components' contribution to dispersion becomes more significant and therefore can not be neglected in simulations. The main dispersion contribution comes from the dichroic mirror (fused silica) and aspherical lens (black diamond, BD-2). We used refractive index equation provided by Thorlabs [194, 195] to simulate their delay contributions. The dichroic mirror is 3 mm thick and the aspherical lens is 2 mm thick. Since the collimated pump laser beam waist (4 mm) is 3 orders of magnitude larger than the beam size in our PCF, the nonlinear parameter of these components is at least 6 orders of magnitude smaller than all the FUTs and can be set to zero in numerical study. GNLSE simulates the complete pulse propagation process from laser output to FUT.

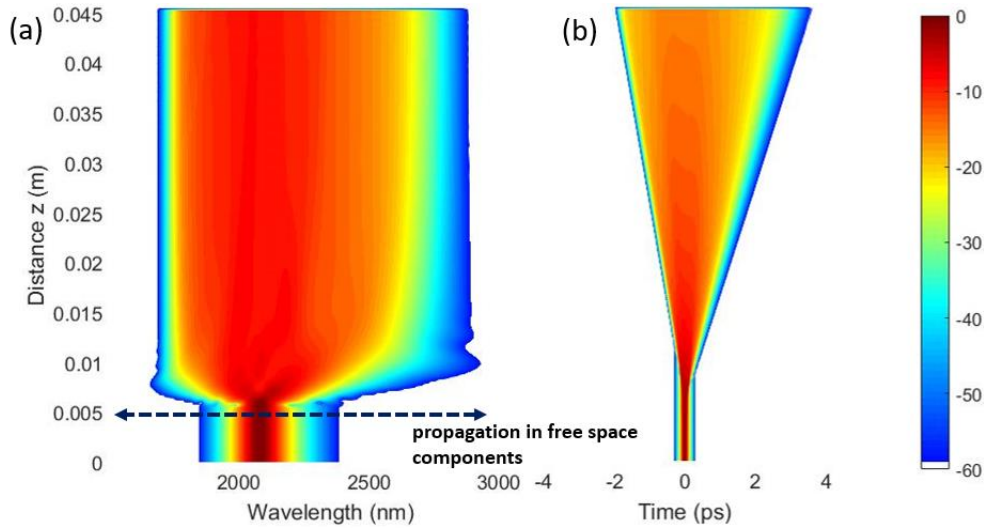


Figure 7.7. Simulated pulse evolution in wavelength (a) and time domain (b), at 2kW peak power. The intensity is normalized to 1 (0 dBm) and plotted in dB scale. Dispersion from lens and dichroic mirror is considered (first 5 mm of the simulation).

In Fig. 7.7, we simulated pulse evolution starting with 5 mm propagation inside the free space optics components (indicated before the black line). After the free space optical components, the pulse goes directly into the ChG PCF. The total simulated fiber length is 4 cm with the same properties as FUT1 and the coupled pump peak power is 2 kW. After entering the FUT, pulse evolution occurs mostly within the first 1 cm of propagation [Fig. 7.7(a)]. In the time domain, the SCG remains a single pulse during the whole propagation length. For a length smaller than 1cm, the pulse maintains a

width of less than 1 ps [Fig. 7.7(b)]. Due to the relatively large dispersion and short input pulse duration, further broadening in the spectral domain is inhibited by the strong pulse broadening in the time domain.

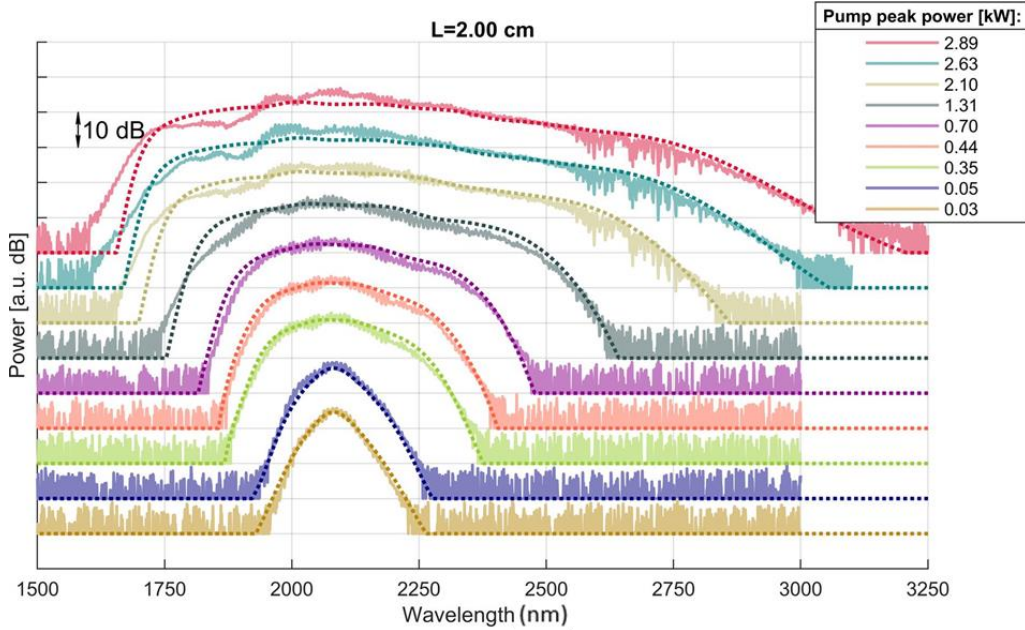


Figure 7.8. Experimental and simulated results of ANDi SCG at different power levels for FUT3. Fiber length is 2 cm. The maximum coupled peak power is 2.9 kW.

As a starting point for the experimental investigation, we tested a 2 cm segment (FUT3). Fig. 7.8 shows the SCG evolution with peak power from 30 to 2890 W. The maximum pump power expands the tail of SCG slightly beyond the ANDi region and the SCG spans close to one octave. At this point, the experimental data show a 3 dB bandwidth from 1925 to 2340 nm (27.6 THz), large enough to support a sub-2 optical cycle pulse. The -20 dB bandwidth is 75.5 THz (1670 to 2880 nm).

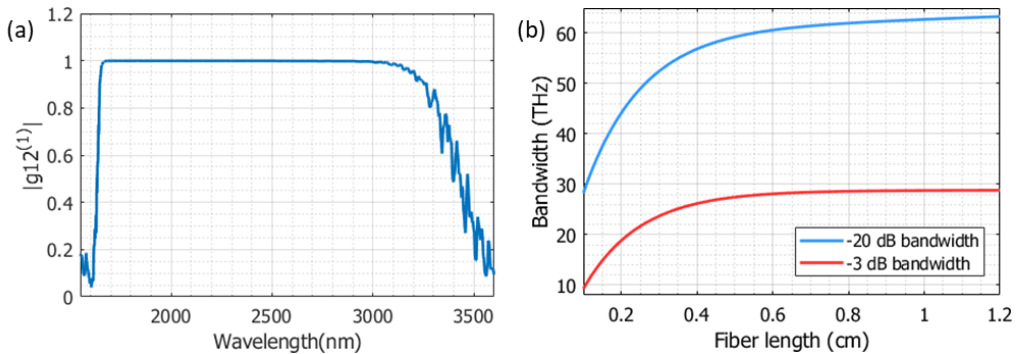


Figure 7.9. ANDi SCG coherence and 3 dB bandwidth evolution. (a) 1st-order coherence for a peak pump power of 2.89 kW on a 2 cm FUT, corresponding to the maximum power in Fig. 7.6. (b) Evolution of -20 dB bandwidth and 3 dB bandwidth during propagation. The peak power is 2 kW in this figure.

From our simulation, even at the highest pump power of 2.9 kW, the pulse remains to be single pulse and highly coherent, i.e. all the advantages of ANDi SCG remain valid. To prove this point, we simulate the first order coherence $g^{(1)}$ using the widely-accepted one photon per wavelength noise assumption [184]. Fig. 7.9(a) shows that the coherence of the whole SCG band is 1, even including part of the spectrum beyond ANDi region. We also plot the evolution of 3 dB bandwidth and -20 dB bandwidth as a function of fiber length in Fig. 7.9 (b). From this simulation, the optimal length for largest 3 dB bandwidth is 7 mm while -20 dB bandwidth only has minor increase beyond 10 mm of fiber length propagation.

We then tested FUT4 (3.4 mm), FUT5 (7.1 mm) and FUT6 (9.7 mm) and summarize the obtained SCG traces in Fig. 7.10. All these short FUTs were prepared by manual cleaving. For better illustration, we show three power levels (0.5, 1 and 2 kW) for each FUT. The inset of Fig. 8 is the picture of FUT4. At the maximum pump power, FUT4 has -20 dB bandwidth of 49 THz and 3 dB bandwidth of 16 THz. Experimental results from FUT4 confirm that we have correctly included the effect of free space optical components in our simulation. Clearly, FUT4 is not long enough for complete broadening of the SCG process, as expected from simulations.

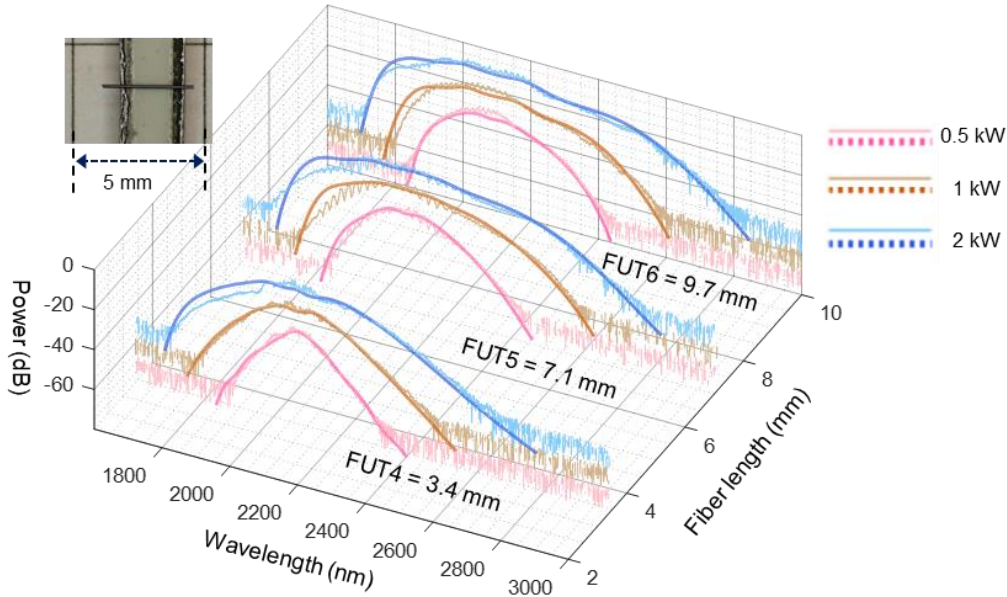


Figure 7.10. SCG at different pump powers for FUT4, FUT5 and FUT6. The simulations (dashed) is superimposed onto the experimental data (solid). Inset: FUT4 on a grid paper.

From Fig. 7.10, FUT6 is close to the optimal length for a complete broadening at 2 kW peak power. At 2 kW peak power, the ANDi SCG from FUT6 shows the same coverage as FUT3. The small difference comes from variations in coupling efficiency.

The maximum 3-dB bandwidth of FUT6 is 23.3 THz, within 4% difference compared with FUT3. In the time domain, simulations indicate 600 fs pulse duration. Notably from Fig.7 (b), the slope of 3 dB bandwidth expansion converges to zero with longer fiber, which is in accordance with the result in [189]. This is also seen by comparing the results for FUT5 and FUT6. Though the -20 dB bandwidth is slightly smaller than for FUT3, both FUT5 and FUT6 show approximately an identical 3-dB bandwidth of 23 THz at 2 kW peak power. However, the shorter length of FUT5 outputs a less dispersed pulse.

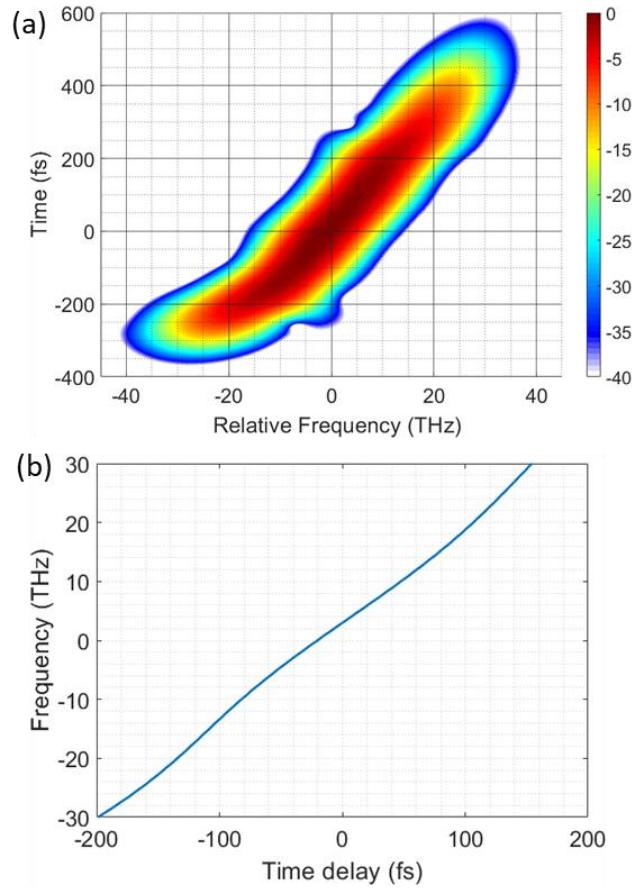


Figure 7.11. The simulated chirp properties of the ANDi SCG pulse. (a) Simulated spectrogram of FUT5 output pulse, amplitude is normalized to 0 dBm; (b) this pulse has a linear chirp. In both plots, the frequency is normalized to the pump

A linearly chirp pulse greatly simplifies the pulse recompression setup. Due to the linear dispersion from our FUTs, we expect linear chirp from the ANDi SCG pulse. Since FUT5 has the optimal length for compression, we retrieve the output pulse properties from simulation. Fig. 7.11(a) shows the simulated spectrogram of FUT5 (7.1 mm length) output at peak power of 2 kW. The spectrogram shows that FUT5 outputs a single pulse with simple phase distribution. Indeed, the output chirp is linear for the complete span of SCG, shown in Fig. 7.11(b). With a linear chirp, the FUT5 output

pulse can be easily compressed with chirped mirrors in 2 μm band. However, due to the difficulty to get chirped mirror at this band, current compression can use grating pair or prism pair constitutions.

7.4 Potential improvements

7.4.1 Simulation of linear pulse compression

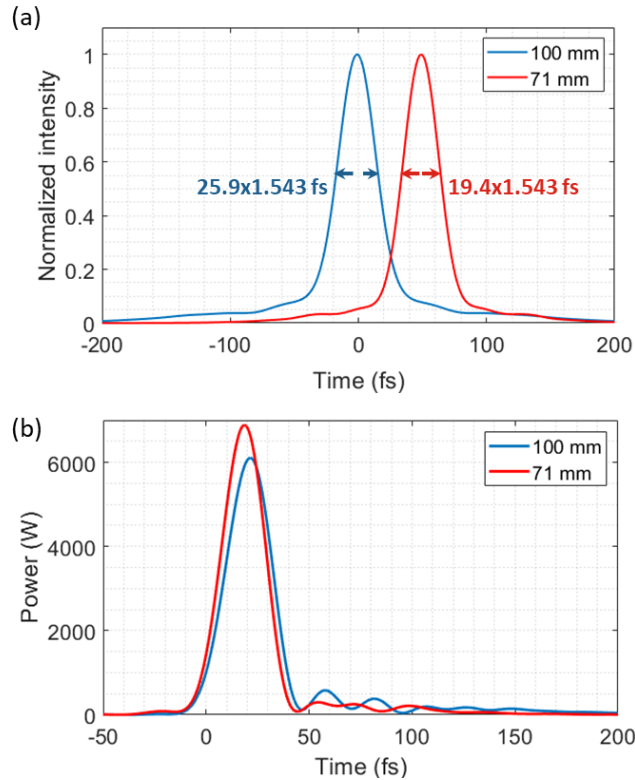


Figure 7.12. Simulation of compressed output power. (a) Simulation of compressed pulse autocorrelation from FUT5 (blue) and FUT6 (red); a -50 fs shift is applied for better illustration. (b) Field profile of FUT5 pulse (blue) and FUT6 pulse (red); higher peak power means better compression.

To start, we simulate the pulse duration by only compressing the group delay dispersion (or β_2 dispersion). The most straightforward method is compression through a pair of chirped mirrors. Here we compare the minimum achievable pulse duration after compression output from FUT5 and FUT6 by simulating of linear compression process, i.e. $\beta_{i,compressor} = 0, \text{ for } i > 2$. Given a similar 3 dB bandwidth, the output pulse from the shorter FUT is expected to have a smaller duration after linear compression. In this case, the third order dispersion contribution becomes the limiting factor of compressed pulse duration. We show, in Fig. 7.12(a), the autocorrelation after a complete compression of 2nd dispersion. FUT5 gives a 19.4 fs pulse for sech fitting (or

21 fs for Gaussian pulse), which is about 3 optical cycles. On the other hand, the pulse profile in linear region clearly shows tails due to third-order dispersion. A higher peak power also indicates better compression of pulse from FUT5 [Fig. 7.12(b)]. The longer compressed pulse from FUT6 is a result of higher third order dispersion due to the slightly longer fiber length (1 cm compared to 0.71 cm).

Due to the limited availability of MIR chirped mirror and existence of 3rd order dispersion, it is a better option to use one or two pairs of Brewster's angled grating to compress the second and third order dispersion of the output pulse. In terms of material, GaF₂, is a good candidate, due to good MIR transmission and relatively low price.

7.4.2 Reaching for octave spanning

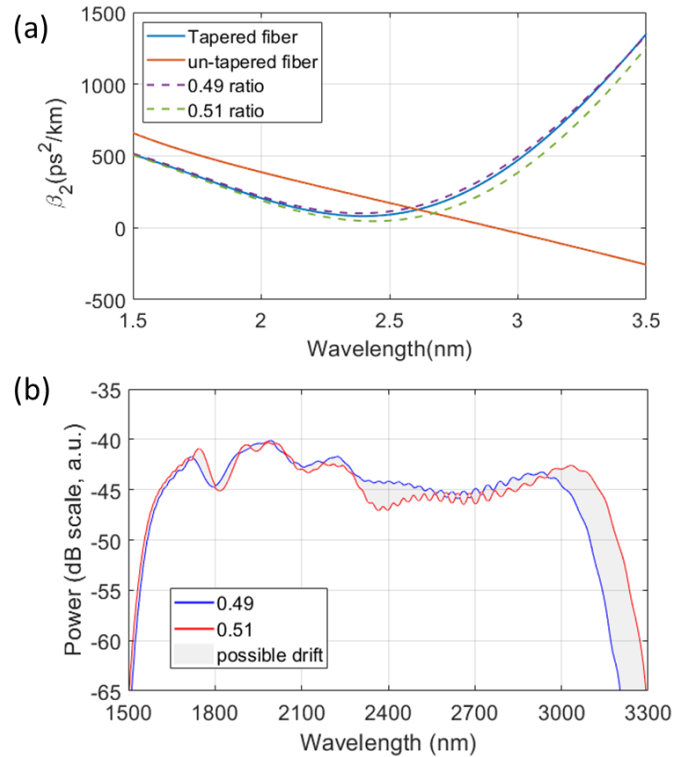


Figure 7.13. Simulation of dispersion and SCG of designed taper PCF. (a) Dispersion simulation of taper PCF with 1.8 μm core and 0.49-0.51 ratio compared to demonstrated fiber. (b) SCG simulation of 2 cm of proposed tapered PCF pumped with 1kW peak power. One needs to tune the input light polarization for maximum SCG coverage.

A broader MIR SCG in an ANDi fiber is desirable for a better coverage of the molecular resonant region. In addition, the fiber length must be as short as possible to avoid strong pulse broadening in time. For this purpose, a larger nonlinear coefficient γ and less dispersion is desirable. Naturally, tapering the current PCF would be an easy solution for both purposes. Commercially available GeAsSe PCF has an air-pitch ratio of ~ 0.5 .

Dispersion simulation was performed based on this ratio with a taper waist diameter $\sim 1.8\mu\text{m}$. The results are shown in Fig.7.13(a). We can see that, even considering possible variations of the ratio around 0.5, the tapered fiber is kept ANDi. Pumping such 2 cm taper at the same wavelength as our previous experiment, at 2070 nm, with 1 kW in peak, 2 cm taper, simulations yields SCG as shown in Fig 7.13(b). The 3 dB amplitude is expected to cover 1690~2640 nm range, leading to a bandwidth of 950 nm (or 64 THz). In addition, the simulation indicates an octave spanning SCG.

It should be noted that experimenting with such fiber requires more careful manipulation. Particularly, the taper transition region on input side should be chopped off to avoid extra pump pulse broadening. This design is optimized for broader SCG – pulse generated from such fiber will require prism pairs for a full chirp compression due to the larger and non-constant third order dispersion. Ideally, pumping with an OPO instead of the current laser allow for reaching a more optimized dispersion point, leading to better re-compression. It should be noticed that the generated SC is highly dependent on the higher order dispersion, which cannot be retrieved precisely from the simulation. Therefore, short input pulse duration, where higher order dispersion becomes more significant, makes the fiber design more challenging, resulting in more complexity in pulse re-compression stage.

7.4.3 Impact of pump pulse duration

As mentioned previously, the ANDi SCG from ChG PCF does not require a high peak power. This property, thus, gives us the opportunity to increase the pump laser repetition rate and pump pulse duration for higher average output power. The state-of-art Tm-doped mode-locked can easily output pulses with 200 fs duration around 100 MHz repetition rate [196]. Currently, the output average power of our ANDi SCG is only 2.5 mW – this power is now too low for further pulse free space alignment due to the limited sensitivity of thermal card. However, if we use a laser with similar properties as pump, we can then achieve an average output power of more than 30 mW. Such average power allows for easy free-space alignment for the $2\mu\text{m}$ light and better tolerance for insertion loss. The only concern is whether the 3 dB bandwidth will be similar when pumped with much longer pulses. To provide some initial idea about this concern, we performed simulations based on a broader input pump pulse.

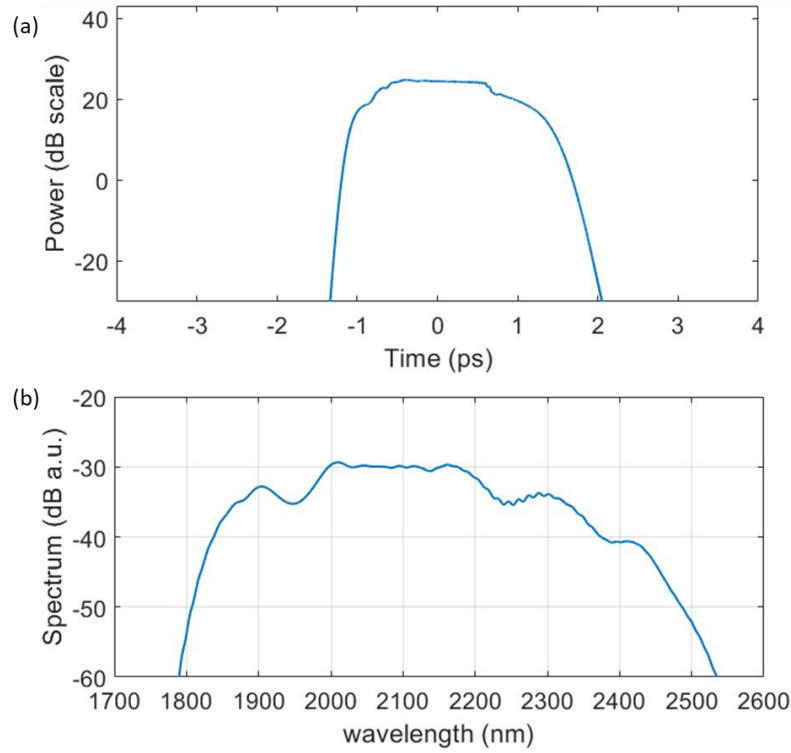


Figure 7.14. Simulation of ANDi SCG using 200fs pump pulse. (a) The pulse temporal broadening after propagating in a 2 cm piece of ChG PCF; (b) The corresponding SCG in spectral domain.

In Fig. 7.14(a) and (b), we show the simulation the ANDi SCG when a 200 fs sech pulse with 2 kW peak power is injected in a ChG PCF. The fiber has the same optical property as FUT1. The new ANDi SCG has a flatter spectrum and larger 3 dB bandwidth. In this case, we do have a smaller 20 dB bandwidth. However, for pulse recompression, the 3 dB bandwidth is the key factor. As shown in Fig. 7.14(b), the 3 dB bandwidth is more than 27.5 THz, comparable to case with 80 fs pump. Therefore, a homemade 200 fs mode-locked laser at 2 μm band can be a good alternative for the current commercial laser.

Conclusion

In conclusion, we studied ANDi SCG inside ChG PCF experimentally and theoretically. Pumping with a fiber laser at moderate peak power level, we experimentally show a -20 dB bandwidth from 1670 to 2880 nm and a 3 dB bandwidth of bandwidth from 1925 to 2340 nm (27.6 THz) using a 2 cm PCF segment. As expected for ANDi SCG, we manage to match our experimental data and theoretical data at all pump powers. Water absorption could pose a big obstacle to ANDi SCG inside ChG, but one can overcome this problem by properly storing the fibers. In addition, we demonstrated pulse evolution along our PCF and found the optimal fiber length for both maximum -20 dB

and 3 dB bandwidth. At last, we simulate the output pulse spectrogram. With a linearly chirped output pulse, one can compress the pulse with a relatively simple setup. Furthermore, recent experiment demonstrated broadband amplification of sub-2 cycle 2000 nm pulse using Kerr instability [197]. Such method could also amplify compressed pulse from ANDi SCG. We believe our study shows ChG PCF could be a good platform to generate few-cycle pulse at MIR.

Chapter 8

Conclusion and further developments

In this project, we have explored the development of coherent MIR light sources using ChG fiber platform. One of the goals was to develop CW pumped single path parametric converters for the MIR. We showed that ChG PCFs offer two degree of freedom for dispersion engineering, and the highest FOM and biggest transmission window in MIR. Using homemade fiber lasers, we performed FWM measurements in the 2 micron band to characterize and compare the optical properties and uniformity of AsSe PCF, GeAsSe PCF and AsS SCF. With the experimentally confirmed results and simulations, we designed tapered GeAsSe PCF under constraints provided from our industrial collaborator. Meanwhile, we improved the homemade fiber laser cavity and pushed the lasing wavelength towards 2.1 μm in order to fully access the targeted spectral region.

The measurement results from the fabricated tapered GeAsSe PCF indicated that the fiber did not exactly meet the design geometry requirements. In our lab, we indeed confirmed experimentally a hole-period ratio variation range and birefringence. Therefore, the ZDW of these tapered PCFs is close to the boundary of Tm/Ho-doped silica fiber lasers making it. It is highly challenging to get broadband or distant conversion using such T-PCFs. Therefore, we aim to improve the CE in CW pumped FWM using this set of T-PCFs. Using homemade 2 μm CW pump lasers, we managed to achieve more than 3 dB CE. In addition, we confirmed that ChG fibers has much higher damage threshold than previous beliefs, thanks to the improved fabrication technology.

During the experiment for amplified parametric conversion, we observed fast backward propagation damage in GeAsSe T-PCFs. The optical discharge blast fiber

core material from the input side and leaves discrete voids behind. Such damage is termed as “fiber fuse” and is a well-known damage phenomenon in silica fibers. Due to the low melting point of ChG fibers, it is widely accepted that fiber fuse is inherently not possible for ChG fibers. We proved that the development of fiber fuse is fast enough to reach an optical discharge before burning through the host fiber. Moreover, we proved fiber fuse in PCF structure is more detrimental than step index fibers. This is due to the propagation of fiber material vapor inside PCF air holes.

Apart from applications with CW lasers, we have also explored generation of coherent and re-compressible SCG using ChG PCFs. In this case, the strong material dispersion becomes beneficial – the linear GVD curve leads to a linear chirp and ease the requirement for compression. Using a 2 μm femtosecond laser, we managed to reach nearly 28 THz 3 dB bandwidth in a 2 cm ChG PCF segment. As should be expected from a deterministic process, we match our simulation perfectly with all our experiment results at all test power levels.

Based on our experiment result, we bring up some future aspects for development of coherent MIR sources based on ChG fibers. For GeAsSe ChG, the exact percentage of each component strongly impact the glass’ physical properties. Different combination ratio of GeAsSe components would lead to change of bandgap energy, hence change the immunity against photodarkening. For better power handling capability and higher immune to photodarkening, it would be necessary to further investigate and optimize the composition of chalcogenide fiber glass.

From the aspect of pump fiber laser, it is more attractive to pump ChG fibers using 3 μm fluoride glass fiber lasers. On one hand, ChG fibers have less loss in this wavelength compared with 2 μm and closer to reach ZDW of ChG fibers. On the other hand, with a more similar melting point, fusion splicing between ChG fibers and fluoride fibers is less challenging. The Er-doped ZBLAN fibers are commercially available and allows lasing up to 2.9 μm . Therefore, a homemade laser utilizing such laser can reach the ZDW of an un-tapered ChG PCF without great difficulty.

To summarize, we believe the future aspect of this project should be a combined force from both side: improved fabrication of ChG PCF and longer working wavelength of fiber lasers. Under such circumstance, a parametric all-fiber MIR source reaching beyond 5 μm could be feasible.

List of References

1. P. Ma, D.-Y. Choi, Y. Yu, X. Gai, Z. Yang, S. Debbarma, S. Madden, and B. Luther-Davies, "Low-loss chalcogenide waveguides for chemical sensing in the mid-infrared," *Opt. Express* **21**, 29927 (2013).
2. P. Ma, D.-Y. Choi, Y. Yu, Z. Yang, K. Vu, T. Nguyen, A. Mitchell, B. Luther-Davies, and S. Madden, "High Q factor chalcogenide ring resonators for cavity-enhanced MIR spectroscopic sensing," *Opt. Express* **23**, 19969 (2015).
3. E. Cadiou, D. Mammez, J.-B. Dherbecourt, G. Gorju, J. Pelon, J.-M. Melkonian, A. Godard, and M. Raybaut, "Atmospheric boundary layer CO₂ remote sensing with a direct detection LIDAR instrument based on a widely tunable optical parametric source," *Opt. Lett.* **42**, 4044 (2017).
4. D. Caffey, M. B. Radunsky, V. Cook, M. Weida, P. R. Buerki, S. Crivello, and T. Day, "Recent results from broadly tunable external cavity quantum cascade lasers," in *SPIE OPTO*, p. 11 (2011)
5. D.-W. Sun, *Infrared spectroscopy for food quality analysis and control*. Academic Press (2009).
6. G. Edwards, R. Logan, M. Copeland, L. Reinisch, J. Davidson, B. Johnson, R. Maciunas, M. Mendenhall, R. Ossoff, and J. Tribble, "Tissue ablation by a free-electron laser tuned to the amide II band," *Nature* **371**, 416 (1994).
7. R. Anderson, W. Farinelli, H. Laubach, D. Manstein, A. N. Yaroslavsky, J. Gubeli, K. Jordan, G. R. Neil, M. Shinn, and W. Chandler, "Selective photothermolysis of lipid-rich tissues: A free electron laser study," *Lasers Med. Sci.* **38**, 913-919 (2006).
8. Méndez, Alexis, and Ted F. Morse, eds. *Specialty optical fibers handbook*. Elsevier (2011)
9. Retrieved from: <https://www.mirphab.eu/>
10. G. Hancock, S. Horrocks, G. Ritchie, J. v. Helden, and R. Walker, "Time-resolved detection of the CF₃ photofragment using chirped QCL radiation," *J. Phys. Chem. A* **112**, 9751 (2008).
11. K. L. Vodopyanov, "Sensing with mid-infrared frequency combs: a novel modality for ultrasensitive detection of hazardous materials," in *SPIE Defense, Security, and Sensing*, p. 8. (2009)
12. K. C. Cossel, E. M. Waxman, F. R. Giorgetta, M. Cermak, I. R. Coddington, D. Hesselius, S. Ruben, W. C. Swann, G.-W. Truong, G. B. Rieker, and N. R. Newbury, "Open-path dual-comb spectroscopy to an airborne retroreflector," *Optica* **4**, 724 (2017).
13. S. Ishii, K. Mizutani, H. Iwai, T. Itabe, H. Fukuoka, T. Ishikawa, A. Sato, K. Asai, M. Yasui, and S. Ochiai, "2- μ m Coherent Lidar Technology Developed at NICT: Past, Current, and Future," in *Applications of Lasers for Sensing and Free Space Communications*, LT3D. 1.
14. S. W. Henderson, P. J. M. Suni, C. P. Hale, S. M. Hannon, J. R. Magee, D. L. Bruns, and E. H. Yuen, "Coherent laser radar at 2 μ m using solid-state lasers," *IEEE Trans. Geosci. Remote Sens* **31**, 4 (1993).
15. R. Frehlich, S. M. Hannon, and S. W. Henderson, "Performance of a 2- μ m Coherent Doppler Lidar for Wind Measurements," *J. Atmospheric Ocean. Technol.* **11**, 1517 (1994).
16. N. Sugimoto, N. Sims, K. Chan, and D. K. Killinger, "Eye-safe 2.1- μ m Ho lidar for measuring atmospheric density profiles," *Opt. Lett.* **15**, 302 (1990).

17. R. Martini, C. Bethea, F. Capasso, C. Gmachl, R. Paiella, E. Whittaker, H. Hwang, D. Sivco, J. Baillargeon, and A. Cho, "Free-space optical transmission of multimedia satellite data streams using mid-infrared quantum cascade lasers," *Electron. Lett* **38**, 181 (2002).
18. Data generated by: modtran.spectral.com/modtran_home
19. L. Shaw, B. Cole, P. Thielen, J. Sanghera, and I. Aggarwal, "Mid-wave IR and long-wave IR laser potential of rare-earth doped chalcogenide glass fiber," *IEEE J. Quantum Electron.* **37**, 1127 (2001).
20. Ł. Sójka, Z. Tang, H. Zhu, E. Bereś-Pawlik, D. Furniss, A. B. Seddon, T. M. Benson, and S. Sujecki, "Study of mid-infrared laser action in chalcogenide rare earth doped glass with Dy³⁺, Pr³⁺ and Tb³⁺," *Opt. Mater. Express* **2**, 1632 (2012).
21. K. Burneika, M. Ignatavicius, V. Kabelka, A. Piskarskas, and A. Stabinis, "Parametric light amplification and oscillation in KDP with mode-locked pump," *IEEE J. Quantum Electron.* **8**, 574 (1972).
22. R. L. Byer, "Optical parametric oscillators," *Quantum Electronics: A Treatise* **1** (1975).
23. C. McGowan, D. T. Reid, Z. E. Penman, M. Ebrahimzadeh, W. Sibbett, and D. H. Jundt, "Femtosecond optical parametric oscillator based on periodically poled lithium niobate," *J. Opt. Soc. Am. B* **15**, 694 (1998).
24. K. McEwan, and J. Terry, "A tandem periodically-poled lithium niobate (PPLN) optical parametric oscillator (OPO)," *Opt. Commun.* **182**, 423 (2000).
25. Z. Zhang, D. T. Reid, S. Chaitanya Kumar, M. Ebrahim-Zadeh, P. G. Schunemann, K. T. Zawilski, and C. R. Howle, "Femtosecond-laser pumped CdSiP₂ optical parametric oscillator producing 100 MHz pulses centered at 6.2 μm ," *Opt. Lett.* **38**, 5110 (2013).
26. L. Maidment, P. G. Schunemann, and D. T. Reid, "Molecular fingerprint-region spectroscopy from 5 to 12 μm using an orientation-patterned gallium phosphide optical parametric oscillator," *Opt. Lett.* **41**, 4261 (2016).
27. K. L. Vodopyanov, E. Sorokin, I. T. Sorokina, and P. G. Schunemann, "Mid-IR frequency comb source spanning 4.4–5.4 μm based on subharmonic GaAs optical parametric oscillator," *Opt. Lett.* **36**, 2275 (2011).
28. J. M. Dudley, D. T. Reid, M. Ebrahimzadeh, and W. Sibbett, "Characteristics of a noncritically phasematched Ti: sapphire pumped femtosecond optical parametric oscillator," *Opt. Commun.* **104**, 419 (1994).
29. G. Ycas, F. R. Giorgetta, E. Baumann, I. Coddington, D. Herman, S. A. Diddams, and N. R. Newbury, "High-coherence mid-infrared dual-comb spectroscopy spanning 2.6 to 5.2 μm ," *Nat. Photonics* **12**, 202 (2018).
30. H. Timmers, A. Kowligy, A. Lind, F. C. Cruz, N. Nader, M. Silfies, G. Ycas, T. K. Allison, P. G. Schunemann, S. B. Papp, and S. A. Diddams, "Molecular fingerprinting with bright, broadband infrared frequency combs," *Optica* **5**, 727 (2018).
31. J. Faist, F. Capasso, D. L. Sivco, C. Sirtori, A. L. Hutchinson, and A. Y. Cho, "Quantum Cascade Laser," *Science* **264**, 553 (1994).
32. R. Paiella, F. Capasso, C. Gmachl, D. L. Sivco, J. N. Baillargeon, A. L. Hutchinson, A. Y. Cho, and H. C. Liu, "Self-Mode-Locking of Quantum Cascade Lasers with Giant Ultrafast Optical Nonlinearities," *Science* **290**, 1739 (2000).

33. Y. Yao, A. J. Hoffman, and C. F. Gmachl, "Mid-infrared quantum cascade lasers," *Nat. Photonics* **6**, 432 (2012).
34. T. Sorokina, V. V. Dvovrin, N. Tolstik, and E. Sorokin, "Mid-IR ultrashort pulsed fiber-based lasers," *IEEE J. Sel. Top. Quantum Electron.* **20**, 99 (2014).
35. Y. Bonetti, and J. Faist, "Quantum cascade lasers: Entering the mid-infrared," *Nat Photon* **3**, 32 (2009).
36. C. E. Hamilton, R. J. Beach, S. B. Sutton, L. H. Furu, and W. F. Krupke, "1-W average power levels and tunability from a diode-pumped 2.94- μm Er:YAG oscillator," *Opt. Lett.* **19**, 1627 (1994).
37. Q. Y. Wang, S. Y. Zhang, and Y. Q. Jia, "Effect of the concentration of the Er³⁺ ion on the spectral intensity parameters of Er:YAG crystals," *J. Alloy. Compd.* **202**, 1 (1993).
38. T. Sorokina, E. Sorokin, S. Mirov, V. Fedorov, V. Badikov, V. Panyutin, A. Di Lieto, and M. Tonelli, "Continuous-wave tunable Cr²⁺:ZnS laser," *Appl. Phys. B* **74**, 607 (2002).
39. S. Mirov, V. Fedorov, I. Moskalev, D. Martyshkin, and C. Kim, "Progress in Cr²⁺ and Fe²⁺ doped mid-IR laser materials," *Laser Photonics Rev.* **4**, 21 (2010).
40. V. V. Fedorov, S. B. Mirov, A. Gallian, D. V. Badikov, M. P. Frolov, Y. V. Korostelin, V. I. Kozlovsky, A. I. Landman, Y. P. Podmar'kov, V. A. Akimov, and A. A. Voronov, "3.77-5.05- μm tunable solid-state lasers based on Fe/sup 2+/-doped ZnSe crystals operating at low and room temperatures," *IEEE J. Quantum Electron.* **42**, 907 (2006).
41. S. B. Mirov, V. V. Fedorov, D. V. Martyshkin, I. S. Moskalev, M. S. Mirov, and V. P. Gapontsev, "Progress in mid-IR Cr²⁺ and Fe²⁺ doped II-VI materials and lasers [Invited]," *Opt. Mater. Express* **1**, 898 (2011).
42. For example: www.ipgphotonics.com/en/products/lasers/mid-ir-hybrid-lasers
43. J. Li, Z. Sun, H. Luo, Z. Yan, K. Zhou, Y. Liu, and L. Zhang, "Wide wavelength selectable all-fiber thulium doped fiber laser between 1925 nm and 2200 nm," *Opt. Express* **22**, 5387 (2014).
44. B. M. Walsh, and N. P. Barnes "Comparison of Tm:ZBLAN and Tm:silica fiber lasers; Spectroscopy and tunable pulsed laser operation around 1.9 μm ," *Appl. Phys. B* **78**, 325 (2004).
45. S. Duval, M. Bernier, V. Fortin, J. Genest, M. Piché, and R. Vallée, "Femtosecond fiber lasers reach the mid-infrared," *Optica* **2**, 623 (2015).
46. M. R. Majewski, R. I. Woodward, J.-Y. Carreé, S. Poulain, M. Poulain, and S. D. Jackson, "Emission beyond 4 μm and mid-infrared lasing in a dysprosium-doped indium fluoride (InF₃) fiber," *Opt. Lett.* **43**, 1926 (2018).
47. F. Maes, V. Fortin, M. Bernier, and R. Vallée, "5.6 W monolithic fiber laser at 3.55 μm ," *Opt. Lett.* **42**, 2054 (2017).
48. F. Maes, V. Fortin, S. Poulain, M. Poulain, J.-Y. Carrée, M. Bernier, and R. Vallée, "Room-temperature fiber laser at 3.92 μm ," *Optica* **5**, 761 (2018).
49. J. S. Sanghera, L. B. Shaw, and I. D. Aggarwal, "Chalcogenide Glass-Fiber-Based Mid-IR Sources and Applications," *IEEE J. Sel. Top. Quantum Electron.* **15**, 114 (2009).
50. T. Schweizer, B. Samson, R. Moore, D. Hewak, and D. Payne, "Rare-earth doped chalcogenide glass fibre laser," *Electron. Lett.* **33**, 414 (1997).
51. J. Cui, X. Xiao, Y. Xu, X. Cui, M. Chen, J. Guo, M. Lu, B. Peng, and H. Guo, "Mid-infrared emissions of Dy³⁺ doped Ga-As-S chalcogenide glasses and fibers and their potential for a 4.2 μm fiber laser," *Opt. Mater. Express* **8**, 2089 (2018).

52. F. Starecki, N. Abdellaoui, A. Braud, J.-L. Doualan, C. Boussard-Plédel, B. Bureau, P. Camy, and V. Nazabal, "8 μm luminescence from a Tb^{3+} GaGeSbSe fiber," *Opt. Lett.* **43**, 1211 (2018).
53. F. Starecki, A. Braud, N. Abdellaoui, J.-L. Doualan, C. Boussard-Plédel, B. Bureau, P. Camy, and V. Nazabal, "7 to 8 μm emission from Sm^{3+} doped selenide fibers," *Opt. Express* **26**, 26462 (2018).
54. K. Vu, K. Yan, and S. Madden, "Internal Gain in Er-doped As₂S₃ Planar Waveguide Amplifiers," in *CELO Europe*. p. CJ_P_2 (2015)
55. L. Sojka, Z. Tang, D. Furniss, H. Sakr, Y. Fang, E. Beres-Pawlik, T. M. Benson, A. B. Seddon, and S. Sujecki, "Mid-infrared emission in Tb^{3+} -doped selenide glass fiber," *J. Opt. Soc. Am. B* **34**, A70 (2017).
56. M. Shen, D. Furniss, Z. Tang, E. Barny, L. Sojka, S. Sujecki, T. M. Benson, and A. B. Seddon, "Modeling of resonantly pumped mid-infrared Pr^{3+} -doped chalcogenide fiber amplifier with different pumping schemes," *Opt. Express* **26**, 23641 (2018).
57. N. Abdellaoui, F. Starecki, C. Boussard-Plédel, Y. Shpotyuk, J. L. Doualan, A. Braud, E. Baudet, P. Nemec, F. Cheviré, M. Dussauze, B. Bureau, P. Camy, and V. Nazabal, " Tb^{3+} doped $\text{Ga}_5\text{Ge}_{20}\text{Sb}_{10}\text{Se}_{65-x}\text{Te}_x$ ($x = 0-37.5$) chalcogenide glasses and fibers for MWIR and LWIR emissions," *Opt. Mater. Express* **8**, 2887 (2018).
58. R. Chahal, F. Starecki, J. L. Doualan, P. Němec, A. Trapananti, C. Prestipino, G. Tricot, C. Boussard-Plédel, K. Michel, A. Braud, P. Camy, J. L. Adam, B. Bureau, and V. Nazabal, " Nd^{3+} :Ga-Ge-Sb-S glasses and fibers for luminescence in mid-IR: synthesis, structural characterization and rare earth spectroscopy," *Opt. Mater. Express* **8**, 1650 (2018).
59. M. Li, Y. Xu, X. Jia, L. Yang, N. Long, Z. Liu, and S. Dai, "Mid-infrared emission properties of Pr^{3+} -doped Ge-Sb-Se-Ga-I chalcogenide glasses," *Opt. Mater. Express* **8**, 992 (2018).
60. K. Nagasaka, T. H. Tuan, H. P. T. Nguyen, M. Matsumoto, S. Cho, T. Suzuki, and Y. Ohishi, "Near-infrared to Mid-infrared wavelength conversion by chalcogenide suspended-core fiber," in *CLEO* p. JTu2A.126. (2018)
61. L. Li, N. Abdukerim, and M. Rochette, "Mid-infrared wavelength conversion from As₂Se₃ microwires," *Opt. Lett.* **42**, 639 (2017).
62. D. D. Hudson, S. Antipov, L. Li, I. Alamgir, T. Hu, M. E. Amraoui, Y. Messaddeq, M. Rochette, S. D. Jackson, and A. Fuerbach, "Toward all-fiber supercontinuum spanning the mid-infrared," *Optica* **4**, 1163 (2017).
63. N. Nader, J. Chiles, H. Timmers, E. J. Stanton, A. Kowligy, A. Lind, S. W. Nam, S. A. Diddams, and R. P. Mirin, "Coherent on-chip frequency combs spanning 1.5–7.5 μm for dual-comb spectroscopy," in *Advanced Photonics*, p. NpM4I.8. (2018)
64. W. S. Rodney, I. H. Malitson, and T. A. King, "Refractive index of arsenic trisulfide," *J. Opt. Soc. Am. A* **48**, 633 (1958).
65. F. Alishahi, A. Vedadi, M. A. Shoaie, C. S. Brès, and K. Mehrany, "Sensitive and Accurate Dispersion Map Extraction of HNLFs by Frequency Tuning of a Degenerate FWM," *J. Light. Technol.* **34**, 4197 (2016).
66. S. Xing, D. Grassani, S. Kharitonov, L. Brilland, C. Caillaud, J. Trolès, and C.-S. Brès, "Mid-infrared continuous-wave parametric amplification in chalcogenide microstructured fibers," *Optica* **4**, 643 (2017).

67. S. Xing, D. Grassani, S. Kharitonov, A. Billat, and C.-S. Brès, "Characterization and modeling of microstructured chalcogenide fibers for efficient mid-infrared wavelength conversion," *Opt. Express* **24**, 9741 (2016).
68. J. S. Sanghera, and I. D. Aggarwal, "Active and passive chalcogenide glass optical fibers for IR applications: a review," in *11th International Symposium on Non-oxide Glasses and New Optical Glasses*, pp. 6-16. (1999)
69. G. Tao, H. Ebendorff-Heidepriem, A. M. Stolyarov, S. Danto, J. V. Badding, Y. Fink, J. Ballato, and A. F. Abouraddy, "Infrared fibers," *Adv. Opt. Photon.* **7**, 379 (2015).
70. R. Thapa, R. R. Gattass, V. Nguyen, G. Chin, D. Gibson, W. Kim, L. B. Shaw, and J. S. Sanghera, "Low-loss, robust fusion splicing of silica to chalcogenide fiber for integrated mid-infrared laser technology development," *Opt. Lett.* **40**, 5074 (2015).
71. E. Dianov, I. Bufetov, A. Frolov, V. Mashinsky, V. Plotnichenko, M. Churbanov, and G. Snopatin, "Catastrophic destruction of fluoride and chalcogenide optical fibres," *Electron. Lett.* **38**, 783 (2002).
72. R. Kashyap, "The Fiber Fuse - from a curious effect to a critical issue: A 25th year retrospective," *Opt. Express* **21**, 6422 (2013).
73. G. Agrawal, *Nonlinear Fiber Optics*, (Academic Press, 2013)
74. R. W. Boyd, *Nonlinear Optics*, (Academic Press, 2008)
75. Mouawad, F. Amrani, B. Kibler, J. Picot-Clémente, C. Strutynski, J. Fatome, F. Désévéday, G. Gadret, J. C. Jules, O. Heintz, E. Lesniewska, and F. Smektala, "Impact of optical and structural aging in As₂S₃ microstructured optical fibers on mid-infrared supercontinuum generation," *Opt. Express* **22**, 23912 (2014).
76. S. Xing, S. Kharitonov, J. Hu, and C.-S. Brès, "Linearly chirped mid-infrared supercontinuum in all-normal-dispersion chalcogenide photonic crystal fibers," *Opt. Express* **26**, 19627 (2018).
77. L. Li, N. Abdukerim, and M. Rochette, "Chalcogenide optical microwires cladded with fluorine-based CYTOP," *Opt. Express* **24**, 18931 (2016).
78. L. Li, A. Al-Kadry, N. Abdukerim, and M. Rochette, "Design, fabrication and characterization of PC, COP and PMMA-cladded As₂Se₃ microwires," *Opt. Mater. Express* **6**, 912 (2016).
79. P. Toupin, L. Brilland, D. Méchin, J.-L. Adam, and J. Troles, "Optical Aging of Chalcogenide Microstructured Optical Fibers," *J. Light. Technol.* **32**, 2428 (2014).
80. B. Tatian, "Fitting refractive-index data with the Sellmeier dispersion formula," *Appl. Opt.* **23**, 4477 (1984).
81. H. G. Dantanarayana, N. Abdel-Moneim, Z. Tang, L. Sojka, S. Sujecki, D. Furniss, A. B. Seddon, I. Kubat, O. Bang, and T. M. Benson, "Refractive index dispersion of chalcogenide glasses for ultra-high numerical-aperture fiber for mid-infrared supercontinuum generation," *Opt. Mater. Express* **4**, 1444 (2014).
82. M. J. Weber, D. Milam, and W. L. Smith, "Nonlinear Refractive Index of Glasses and Crystals," p. 7. (SPIE1978)
83. Saliminia, A. Villeneuve, T. V. Galstyan, S. LaRochelle, and K. Richardson, "First- and second-order Bragg gratings in single-mode planar waveguides of chalcogenide glasses," *J. Light. Technol.* **17**, 837 (1999).

84. J. T. Gopinath, M. Soljačić, E. P. Ippen, V. N. Fuflyigin, W. A. King, and M. Shurgalin, "Third order nonlinearities in Ge-As-Se-based glasses for telecommunications applications," *J. Appl. Phys.* **96**, 6931 (2004).
85. G. Agrawal, *Nonlinear Fiber Optics*, (Academic Press, 2013)
86. M. E. Marhic, *Fiber optical parametric amplifiers, oscillators and related devices* (Cambridge university press, 2008).
87. M. E. Marhic, P. A. Andrekson, P. Petropoulos, S. Radic, C. Peucheret, and M. Jazayerifar, "Fiber optical parametric amplifiers in optical communication systems," *Laser Photonics Rev.* **9**, 50 (2015).
88. J. M. Dudley, G. Genty, and S. Coen, "Supercontinuum generation in photonic crystal fiber," *Rev. Mod. Phys.* **78**, 1135 (2006).
89. F. Shimizu, "Frequency Broadening in Liquids by a Short Light Pulse," *Phys. Rev. Lett.* **19**, 1097 (1967).
90. W. J. Tomlinson, R. H. Stolen, and A. M. Johnson, "Optical wave breaking of pulses in nonlinear optical fibers," *Opt. Lett.* **10**, 457 (1985).
91. C. Finot, B. Kibler, L. Provost, and S. Wabnitz, "Beneficial impact of wave-breaking for coherent continuum formation in normally dispersive nonlinear fibers," *J. Opt. Soc. Am. B* **25**, 1938 (2008).
92. M. Heidt, "Pulse preserving flat-top supercontinuum generation in all-normal dispersion photonic crystal fibers," *J. Opt. Soc. Am. B* **27**, 550 (2010).
93. J. P. Gordon, "Theory of the soliton self-frequency shift," *Opt. Lett.* **11**, 662 (1986).
94. B. Salem, R. Cherif, and M. Zghal, "Raman response of a highly nonlinear As₂Se₃-based chalcogenide photonic crystal fiber," in *PIERS Proceedings*, p. 1256. (2011)
95. Faure, W. Blanc, B. Dussardier, and G. Monnom, "Improvement of the Tm³⁺:3H₄ level lifetime in silica optical fibers by lowering the local phonon energy," *J. Non-Cryst. Solids* **353**, 2767 (2007).
96. N. Simakov, A. Hemming, W. A. Clarkson, J. Haub, and A. Carter, "A cladding-pumped, tunable holmium doped fiber laser," *Opt. Express* **21**, 28415 (2013).
97. S. D. Jackson, "The spectroscopic and energy transfer characteristics of the rare earth ions used for silicate glass fibre lasers operating in the shortwave infrared," *Laser Photonics Rev.* **3**, 466 (2009).
98. S. Xing, S. Kharitonov, J. Hu, D. Grassani, and C.-S. Brès, "Stable 2.1 μm near 100% polarized Ho-doped all-fiber laser based on a polarizer-free cavity scheme," in *ECOC*, pp. 1-3.(2017)
99. Marian, M. C. Stowe, J. R. Lawall, D. Felinto, and J. Ye, "United Time-Frequency Spectroscopy for Dynamics and Global Structure," *Science* **306**, 2063 (2004).
100. S. Feng, Q. Mao, L. Shang, and J. W. Y. Lit, "Reflectivity characteristics of the fiber loop mirror with a polarization controller," *Opt. Commun.* **277**, 322 (2007).
101. J. Wang, K. Zheng, J. Peng, L. Liu, J. Li, and S. Jian, "Theory and experiment of a fiber loop mirror filter of two-stage polarization-maintaining fibers and polarization controllers for multiwavelength fiber ring laser," *Opt. Express* **17**, 10573 (2009).
102. J.-P. Cariou, B. Augere, and M. Valla, "Laser source requirements for coherent lidars based on fiber technology," *Comptes Rendus Physique* **7**, 213 (2006).
103. N. Simakov, Z. Li, S.-U. Alam, P. C. Shardlow, J. M. O. daniel, D. Jain, J. K. Sahu, A. Hemming, A. Clarkson, and D. J. Richardson, "Holmium Doped Fiber Amplifier for Optical Communications at 2.05 - 2.13 μm ," in *OFC*, p. Tu2C.6. (2015)

- 104.R. M. Schotland, K. Sassen, and R. Stone, "Observations by lidar of linear depolarization ratios for hydrometeors," *J. Appl. Meteorol. Climatol.* **10**, 1011 (1971).
- 105.J. Biele, G. Beyerle, and G. Baumgarten, "Polarization lidar: Corrections of instrumental effects," *Opt. Express* **7**, 427 (2000).
- 106.S. D. Agger, and J. H. Povlsen, "Emission and absorption cross section of thulium doped silica fibers," *Opt. Express* **14**, 50 (2006).
- 107.S. Kharitonov, and C.-S. Brès, "Isolator-free unidirectional thulium-doped fiber laser," *Light Sci. Appl.* **4**, e340 (2015).
- 108.A. Sincore, J. Cook, F. Tan, A. El Halawany, A. Riggins, S. McDaniel, G. Cook, D. V. Martyshkin, V. V. Fedorov, S. B. Mirov, L. Shah, A. F. Abouraddy, M. C. Richardson, and K. L. Schepler, "High power single-mode delivery of mid-infrared sources through chalcogenide fiber," *Opt. Express* **26**, 7313 (2018).
- 109.A. Sincore, J. Cook, F. Tan, A. El Halawany, A. Riggins, L. Shah, A. Abouraddy, M. C. Richardson, and K. L. Schepler, "High Power 2053 nm Transmission through Single-mode Chalcogenide Fiber," in *Advanced Solid State Lasers*. p. ATu5A. 5. (2017)
- 110.H. Shi, X. Feng, F. Tan, P. Wang, and P. Wang, "Multi-watt mid-infrared supercontinuum generated from a dehydrated large-core tellurite glass fiber," *Opt. Mater. Express* **6**, 3967 (2016).
- 111.I. Savellii, O. Mouawad, J. Fatome, B. Kibler, F. Désévéday, G. Gadret, J. C. Jules, P. Y. Bony, H. Kawashima, W. Gao, T. Kohoutek, T. Suzuki, Y. Ohishi, and F. Smektala, "Mid-infrared 2000-nm bandwidth supercontinuum generation in suspended-core microstructured Sulfide and Tellurite optical fibers," *Opt. Express* **20**, 27083 (2012).
- 112.A. N. Ghosh, M. Klimczak, R. Buczynski, J. M. Dudley, and T. Sylvestre, "Supercontinuum generation in heavy-metal oxide glass based suspended-core photonic crystal fibers," *J. Opt. Soc. Am. B* **35**, 2311 (2018).
- 113.T. Cheng, L. Zhang, X. Xue, D. Deng, T. Suzuki, and Y. Ohishi, "Broadband cascaded four-wave mixing and supercontinuum generation in a tellurite microstructured optical fiber pumped at 2 μm ," *Opt. Express* **23**, 4125 (2015).
- 114.X. Jiang, N. Y. Joly, M. A. Finger, F. Babic, K. L. WongGordon, J. C. Travers, and J. RussellPhilip St, "Deep-ultraviolet to mid-infrared supercontinuum generated in solid-core ZBLAN photonic crystal fibre," *Nat Photon* **9**, 133 (2015).
- 115.M. Klimczak, G. Stepniewski, H. Bookey, A. Szolno, R. Stepien, D. Pysz, A. Kar, A. Waddie, M. R. Taghizadeh, and R. Buczynski, "Broadband infrared supercontinuum generation in hexagonal-lattice tellurite photonic crystal fiber with dispersion optimized for pumping near 1560 nm," *Opt. Lett.* **38**, 4679 (2013).
- 116.N. Healy, L. Lagonigro, J. R. Sparks, S. Boden, P. J. A. Sazio, J. V. Badding, and A. C. Peacock, "Polycrystalline silicon optical fibers with atomically smooth surfaces," *Opt. Lett.* **36**, 2480 (2011).
- 117.C.-C. Lai, C.-Y. Lo, D. H. Nguyen, J.-Z. Huang, W.-S. Tsai, and Y.-R. Ma, "Atomically smooth hybrid crystalline-core glass-clad fibers for low-loss broadband wave guiding," *Opt. Express* **24**, 20089 (2016).
- 118.J. R. Sparks, R. He, N. Healy, M. Krishnamurthi, A. C. Peacock, P. J. A. Sazio, V. Gopalan, and J. V. Badding, "Zinc Selenide Optical Fibers," *Adv. Mater.* **23**, 1647 (2011).

- 119.M. R. Abu Hassan, F. Yu, W. J. Wadsworth, and J. C. Knight, "Cavity-based mid-IR fiber gas laser pumped by a diode laser," *Optica* **3**, 218 (2016).
- 120.F. Désévéday, G. Renversez, J. Troles, P. Houizot, L. Brilland, I. Vasilief, Q. Coulombier, N. Traynor, F. Smektala, and J.-L. Adam, "Chalcogenide glass hollow core photonic crystal fibers," *Opt. Mater.* **32**, 1532 (2010).
- 121.B. Temelkuran, S. D. Hart, G. Benoit, J. D. Joannopoulos, and Y. Fink, "Wavelength-scalable hollow optical fibres with large photonic bandgaps for CO₂ laser transmission," *Nature* **420**, 650 (2002).
- 122.C. Tonglei, H. Kawashima, X. Xiaojie, D. Dinghuan, M. Matsumoto, T. Misumi, T. Suzuki, and Y. Ohishi, "Fabrication of a Chalcogenide-Tellurite Hybrid Microstructured Optical Fiber for Flattened and Broadband Supercontinuum Generation," *J. Light. Technol* **33**, 333 (2015).
- 123.J. Ballato, T. Hawkins, P. Foy, B. Yazgan-Kokuoz, R. Stolen, C. McMillen, N. K. Hon, B. Jalali, and R. Rice, "Glass-clad single-crystal germanium optical fiber," *Opt. Express* **17**, 8029 (2009).
- 124.D. Milam, and M. J. Weber, "Measurement of nonlinear refractive-index coefficients using time-resolved interferometry: Application to Opt. Mater. for high-power neodymium lasers," *J. Appl. Phys.* **47**, 2497 (1976).
- 125.C. Agger, C. Petersen, S. Dupont, H. Steffensen, J. K. Lyngsø, C. L. Thomsen, J. Thøgersen, S. R. Keiding, and O. Bang, "Supercontinuum generation in ZBLAN fibers—detailed comparison between measurement and simulation," *J. Opt. Soc. Am. B* **29**, 635 (2012).
- 126.J. S. Wang, E. M. Vogel, and E. Snitzer, "Tellurite glass: a new candidate for fiber devices," *Opt. Mater.* **3**, 187 (1994).
- 127.G. Whaley, "AMTIR-6 (As₂S₃). Amorphous Materials Inc."
- 128.M. R. E. Lamont, B. Luther-Davies, D.-Y. Choi, S. Madden, X. Gai, and B. J. Eggleton, "Net-gain from a parametric amplifier on a chalcogenide optical chip," *Opt. Express* **16**, 20374 (2008).
- 129.R. E. Slusher, G. Lenz, J. Hodelin, J. Sanghera, L. B. Shaw, and I. D. Aggarwal, "Large Raman gain and nonlinear phase shifts in high-purity As₂Se₃ chalcogenide fibers," *J. Opt. Soc. Am. B* **21**, 1146 (2004).
- 130.A. Kinoshita, "Characterization of glass transition in a-As₂Se₃ by heat of vaporization," *J. Non-Cryst. Solids* **42**, 447 (1980).
- 131.For commercial ZBLAN fiber transmission: www.fiberlabs-inc.com/technology/
- 132.C. Yao, Z. Jia, Z. Li, S. Jia, Z. Zhao, L. Zhang, Y. Feng, G. Qin, Y. Ohishi, and W. Qin, "High-power mid-infrared supercontinuum laser source using fluorotellurite fiber," *Optica* **5**, 1264 (2018).
- 133.J. Troles, Q. Coulombier, G. Canat, M. Duhant, W. Renard, P. Toupin, L. Calvez, G. Renversez, F. Smektala, M. El Amraoui, J. L. Adam, T. Chartier, D. Mechin, and L. Brilland, "Low loss microstructured chalcogenide fibers for large non-linear effects at 1995 nm," *Opt. Express* **18**, 26647 (2010).
- 134.B. J. Eggleton, B. Luther-Davies, and K. Richardson, "Chalcogenide photonics," *Nat. Photon* **5**, 141 (2011).
- 135.F. Yaman, Q. Lin, S. Radic, and G. P. Agrawal, "Impact of dispersion fluctuations on dual-pump fiber-optic parametric amplifiers," *IEEE Photonic Tech. L.* **16**, 1292 (2004).

- 136.R. Cherif, A. Ben Salem, M. Zghal, P. Besnard, T. Chartier, L. Brilland, and J. Troles, "Highly nonlinear As₂Se₃-based chalcogenide photonic crystal fiber for midinfrared supercontinuum generation," *Opt. Eng.*, **49**, 095002.
- 137.M. El-Amraoui, G. Gadret, J. C. Jules, J. Fatome, C. Fortier, F. Désévéday, I. Skripatchev, Y. Messaddeq, J. Troles, L. Brilland, W. Gao, T. Suzuki, Y. Ohishi, and F. Smektala, "Microstructured chalcogenide optical fibers from As₂S₃ glass: towards new IR broadband sources," *Opt. Express* **18**, 26655 (2010).
- 138.S. D. Le, D. M. Nguyen, M. Thual, L. Bramerie, M. Costa e Silva, K. Lenglé, M. Gay, T. Chartier, L. Brilland, D. Méchin, P. Toupin, and J. Troles, "Efficient four-wave mixing in an ultra-highly nonlinear suspended-core chalcogenide As₃₈Se₆₂ fiber," *Opt. Express* **19**, B653 (2011).
- 139.S. D. Le, M. Gay, L. Bramerie, M. Costa e Silva, K. Lenglé, T. Chartier, M. Thual, J.-C. Simon, L. Brilland, D. Méchin, P. Toupin, and J. Troles, "Wavelength conversion in a highly nonlinear chalcogenide microstructured fiber," *Opt. Lett.* **37**, 4576 (2012).
- 140.X. Feng, "Broadband infrared supercontinuum generation in hexagonal-lattice tellurite photonic crystal fiber with dispersion optimized for pumping near 1560 nm: comment," *Opt. Lett.* **39**, 2240 (2014).
- 141.DragicP, HawkinsT, FoyP, MorrisS, and BallatoJ, "Sapphire-derived all-glass optical fibres," *Nat. Photon* **6**, 627 (2012).
142. www.thorlabs.com/NewGroupPage9.cfm?ObjectGroup_ID=3982
- 143.C. Wei, R. Joseph Weiblen, C. R. Menyuk, and J. Hu, "Negative curvature fibers," *Adv. Opt. Photon.* **9**, 504 (2017).
- 144.M. Xu, F. Yu, M. R. A. Hassan, and J. C. Knight, "Continuous-Wave Mid-Infrared Gas Fiber Lasers," *IEEE J. Sel. Top. Quantum Electron.* **24**, 1 (2018).
- 145.A. V. Gladyshev, A. F. Kosolapov, M. M. Khudyakov, Y. P. Yatsenko, A. N. Kolyadin, A. A. e. Krylov, A. D. Pryamikov, A. S. Biriukov, M. E. e. Likhachev, and I. A. Bufetov, "4.4- μ m Raman laser based on hollow-core silica fibre," *Quantum Electronics* **47**, 491 (2017).
- 146.Y.-G. Jeong, R. Piccoli, D. Ferachou, V. Cardin, M. Chini, S. Hädrich, J. Limpert, R. Morandotti, F. L  gar  , B. E. Schmidt, and L. Razzari, "Direct compression of 170-fs 50-cycle pulses down to 1.5 cycles with 70% transmission," *Sci. Rep* **8**, 11794 (2018).
- 147.C. Gaida, M. Gebhardt, F. Stutzki, C. Jauregui, J. Limpert, and A. T  nnermann, "90 fs pulses with > 5 GW peak power from a high repetition rate Tm-doped fiber CPA system," in *Laser Congress*, p. AT3A.5. (2017)
- 148.M. Gebhardt, C. Gaida, F. Stutzki, C. Jauregui, J. Antonio-Lopez, A. Schulzgen, R. Amezcua-Correa, J. Limpert, and A. T  nnermann, "High average power nonlinear self-compression to few-cycle pulses at 2 μ m wavelength in antiresonant hollow-core fiber," in *Laser Congress*, p. AT3A.6. (2017)
- 149.J. S. Sanghera, L. B. Shaw, C. M. Florea, P. Pureza, V. Q. Nguyen, D. Gibson, F. Kung, and I. D. Aggarwal, "Non-linearity in chalcogenide glasses and fibers, and their applications," in *Conference on Lasers and Electro-Optics and Conference on Quantum Electronics and Laser Science*, pp. 1-2. (2008)
- 150.S. Shabahang, F. A. Tan, J. D. Perlstein, G. Tao, O. Alvarez, F. Chenard, A. Sincore, L. Shah, M. C. Richardson, K. L. Schepler, and A. F. Abouraddy, "Robust multimaterial chalcogenide fibers produced by a hybrid fiber-fabrication process," *Opt. Mater. Express* **7**, 2336 (2017).

151. E. C. Mägi, L. B. Fu, H. C. Nguyen, M. R. Lamont, D. I. Yeom, and B. J. Eggleton, "Enhanced Kerr nonlinearity in sub-wavelength diameter As₂Se₃ chalcogenide fiber tapers," *Opt. Express* **15**, 10324 (2007).
152. R. Ahmad, and M. Rochette, "High efficiency and ultra broadband optical parametric four-wave mixing in chalcogenide-PMMA hybrid microwires," *Opt. Express* **20**, 9572 (2012).
153. Data from: agcem.com/files/pdf/cytops/Cytop_IR_transmittance.pdf
154. S. Kharitonov, A. Billat, and C.-S. Brès, "Kerr nonlinearity and dispersion characterization of core-pumped thulium-doped fiber at 2 μ m," *Opt. Lett.* **41**, 3173 (2016).
155. A. Gershikov, E. Shumakher, A. Willinger, and G. Eisenstein, "Fiber parametric oscillator for the 2 μ m wavelength range based on narrowband optical parametric amplification," *Opt. Lett.* **35**, 3198 (2010).
156. X. Liu, R. M. Osgood, Y. A. Vlasov, and M. J. GreenWilliam, "Mid-infrared optical parametric amplifier using silicon nanophotonic waveguides," *Nat. Photon* **4**, 557 (2010).
157. N. Abdukerim, L. Li, and M. Rochette, "Chalcogenide-based optical parametric oscillator at 2 μ m," *Opt. Lett.* **41**, 4364 (2016).
158. G. Lenz, J. Zimmermann, T. Katsufuji, M. E. Lines, H. Y. Hwang, S. Spälter, R. E. Slusher, S. W. Cheong, J. S. Sanghera, and I. D. Aggarwal, "Large Kerr effect in bulk Se-based chalcogenide glasses," *Opt. Lett.* **25**, 254 (2000).
159. J. Fatome, C. Fortier, T. N. Nguyen, T. Chartier, F. Smektala, K. Messaad, B. Kibler, S. Pitois, G. Gadret, C. Finot, J. Troles, F. Desevedavy, P. Houizot, G. Renversez, L. Brilland, and N. Traynor, "Linear and Nonlinear Characterizations of Chalcogenide Photonic Crystal Fibers," *J. Light. Technol.* **27**, 1707 (2009).
160. W. J. Wadsworth, A. Witkowska, S. G. Leon-Saval, and T. A. Birks, "Hole inflation and tapering of stock photonic crystal fibres," *Opt. Express* **13**, 6541 (2005).
161. C. R. Petersen, R. D. Engelsholm, C. Markos, L. Brilland, C. Caillaud, J. Trolès, and O. Bang, "Increased mid-infrared supercontinuum bandwidth and average power by tapering large-mode-area chalcogenide photonic crystal fibers," *Opt. Express* **25**, 15336 (2017).
162. P. S. J. Russell, "Photonic-crystal fibers," *J. Light. Technol.* **24**, 4729 (2006).
163. J. D. Musgraves, S. Danto, and K. Richardson, "4 - Thermal properties of chalcogenide glasses," in *Chalcogenide Glasses* (Woodhead Publishing, 2014)
164. S. Kharitonov, S. Xing, and C.-S. Brès, "Broadband Dispersion Characterization of Chalcogenide Tapered Photonic Crystal Fiber," in *Laser Congress*, p. JM5A.10. (2017)
165. S. Xing, S. Kharitonov, J. Hu, and C.-S. Brès, "Fiber fuse in chalcogenide photonic crystal fibers," *Opt. Lett.* **43**, 1443 (2018).
166. R. Kashyap, "Spectacular demonstration of catastrophic failure in long length of optical fibre via self-propelled self-focusing," *Eighth National Quantum Electronics Conference*, (1987).
167. S.-i. Todoroki, "Fiber Fuse," (Springer, 2014).
168. D. P. Hand, and P. S. J. Russell, "Solitary thermal shock waves and optical damage in optical fibers: the fiber fuse," *Opt. Lett.* **13**, 767 (1988).
169. S.-i. Todoroki, "Origin of periodic void formation during fiber fuse," *Opt. Express* **13**, 6381 (2005).
170. R. M. Atkins, P. G. Simpkins, and A. D. Yablon, "Track of a fiber fuse: a Rayleigh instability in optical waveguides," *Opt. Lett.* **28**, 974 (2003).

- 171.S. Jiang, L. Ma, X. Fan, S. Wang, and Z. He, "Observation of fiber fuse propagation speed with high temporal resolution using heterodyne detection and time-frequency analysis," *Opt. Lett.* **42**, 3355 (2017).
- 172.N. Hanzawa, K. Kurokawa, K. Tsujikawa, T. Matsui, K. Nakajima, S. Tomita, and M. Tsubokawa, "Suppression of Fiber Fuse Propagation in Hole Assisted Fiber and Photonic Crystal Fiber," *J. Light. Technol.* **28**, 2115 (2010).
- 173.W. Ha, Y. Jeong, and K. Oh, "Fiber fuse effect in hollow optical fibers," *Opt. Lett.* **36**, 1536 (2011).
- 174.K. S. Abedin, M. Nakazawa, and T. Miyazaki, "Backreflected radiation due to a propagating fiber fuse," *Opt. Express* **17**, 6525 (2009).
- 175.Y. Mizuno, N. Hayashi, H. Tanaka, K. Nakamura, and S.-i. Todoroki, "Observation of polymer optical fiber fuse," *Appl. Phys. Lett.* **104**, 043302 (2014).
- 176.E. Dianov, I. Bufetov, A. Frolov, V. Plotnichenko, V. Mashinsky, M. Churbanov, and G. Snopatin, "Catastrophic destruction of optical fibres of various composition caused by laser radiation," *Quantum Electron.* **32**, 476 (2002).
- 177.L. Liu, T. Cheng, K. Nagasaka, H. Tong, G. Qin, T. Suzuki, and Y. Ohishi, "Coherent mid-infrared supercontinuum generation in all-solid chalcogenide microstructured fibers with all-normal dispersion," *Opt. Lett.* **41**, 392 (2016).
- 178.C.-S. Brès, S. Zlatanovic, A. O. J. Wiberg, and S. Radic, "Continuous-wave four-wave mixing in cm-long Chalcogenide microstructured fiber," *Opt. Express* **19**, B621 (2011).
- 179.J. M. Dudley, and J. R. Taylor, "Ten years of nonlinear optics in photonic crystal fibre," *Nat. Photon* **3**, 85 (2009).
- 180.Z. Zheming, W. Bo, W. Xunsi, P. Zhanghao, L. Zijun, Z. Peiqing, S. Xiang, N. Qiuhua, D. Shixun, and W. Rongping, "Mid-infrared supercontinuum covering 2.0–16 μm in a low-loss telluride single-mode fiber," *Laser Photonics Rev.* **11**, 1700005 (2017).
- 181.T. Cheng, K. Nagasaka, T. H. Tuan, X. Xue, M. Matsumoto, H. Tezuka, T. Suzuki, and Y. Ohishi, "Mid-infrared supercontinuum generation spanning 2.0 to 15.1 μm in a chalcogenide step-index fiber," *Opt. Lett.* **41**, 2117 (2016).
- 182.Z. Zhao, X. Wang, S. Dai, Z. Pan, S. Liu, L. Sun, P. Zhang, Z. Liu, Q. Nie, X. Shen, and R. Wang, "1.5–14 μm midinfrared supercontinuum generation in a low-loss Te-based chalcogenide step-index fiber," *Opt. Lett.* **41**, 5222 (2016).
- 183.C. R. Petersen, U. Møller, I. Kubat, B. Zhou, S. Dupont, J. Ramsay, T. Benson, S. Sujecki, N. Abdel-Moneim, Z. Tang, D. Furniss, A. Seddon, and O. Bang, "Mid-infrared supercontinuum covering the 1.4–13.3 μm molecular fingerprint region using ultra-high NA chalcogenide step-index fibre," *Nat. Photon* **8**, 830 (2014).
- 184.J. M. Dudley, and S. Coen, "Coherence properties of supercontinuum spectra generated in photonic crystal and tapered optical fibers," *Opt. Lett.* **27**, 1180 (2002).
- 185.J. M. Dudley, and S. Coen, "Fundamental limits to few-cycle pulse generation from compression of supercontinuum spectra generated in photonic crystal fiber," *Opt. Express* **12**, 2423 (2004).
- 186.W. J. Tomlinson, R. H. Stolen, and C. V. Shank, "Compression of optical pulses chirped by self-phase modulation in fibers," *J. Opt. Soc. Am. B* **1**, 139 (1984).

187. A. M. Heidt, A. Hartung, G. W. Bosman, P. Krok, E. G. Rohwer, H. Schwoerer, and H. Bartelt, "Coherent octave spanning near-infrared and visible supercontinuum generation in all-normal dispersion photonic crystal fibers," *Opt. Express* **19**, 3775 (2011).
188. L. E. Hooper, P. J. Mosley, A. C. Muir, W. J. Wadsworth, and J. C. Knight, "Coherent supercontinuum generation in photonic crystal fiber with all-normal group velocity dispersion," *Opt. Express* **19**, 4902 (2011).
189. A. M. Heidt, J. Rothhardt, A. Hartung, H. Bartelt, E. G. Rohwer, J. Limpert, and A. Tünnermann, "High quality sub-two cycle pulses from compression of supercontinuum generated in all-normal dispersion photonic crystal fiber," *Opt. Express* **19**, 13873 (2011).
190. M. Klimczak, B. Siwicki, P. Skibiński, D. Pysz, R. Stępień, A. Heidt, C. Radzewicz, and R. Buczyński, "Coherent supercontinuum generation up to 2.3 μm in all-solid soft-glass photonic crystal fibers with flat all-normal dispersion," *Opt. Express* **22**, 18824 (2014).
191. K. Tarnowski, T. Martynkien, P. Mergo, K. Poturaj, G. Soboń, and W. Urbańczyk, "Coherent supercontinuum generation up to 2.2 μm in an all-normal dispersion microstructured silica fiber," *Opt. Express* **24**, 30523 (2016).
192. A. Al-Kadry, L. Li, M. E. Amraoui, T. North, Y. Messaddeq, and M. Rochette, "Broadband supercontinuum generation in all-normal dispersion chalcogenide microwires," *Opt. Lett.* **40**, 4687 (2015).
193. L. Li, "Chalcogenide Microwires Cladded with Hydrogen-and Fluorine-based Polymers and Their Applications," (McGill University Libraries, 2017).
194. Refractive index of black diamond: thorlabs.com/newgrouppage9.cfm?objectgroup_id=4791
195. Refractive index of fused silica: thorlabs.com/newgrouppage9.cfm?objectgroup_id=6973
196. R. Liao, Y. Song, W. Liu, H. Shi, L. Chai, and M. Hu, "Dual-comb spectroscopy with a single free-running thulium-doped fiber laser," *Opt. Express* **26**, 11046 (2018).
197. G. Vampa, T. J. Hammond, M. Nesrallah, A. Y. Naumov, P. B. Corkum, and T. Brabec, "Light amplification by seeded Kerr instability," *Science* **359**, 673 (2018).

Sida Xing

Email: si.xing@epfl.ch

phone: +41-78-9658594

Address: ELD 014, PHOSL, EPFL
CH-1015, Lausanne, Switzerland

EDUCATION

Mar. 2015 - Present	Doctoral School of Photonics , Doctoral Assistant École Polytechnique Fédérale de Lausanne, Switzerland
Sept. 2013 - May. 2015	Department of Electrical Engineering , Master McGill University, Canada
Sept. 2009 - May. 2013	Department of Electrical Engineering , Bachelor McGill University, Canada
Sept. 2008 - May. 2009	School of Astronautics , Bachelor (Transferred to McGill University in 2009) Harbin Institute of Technology, China

RESEARCH EXPERIENCE

March. 2015 - Present	Coherent mid-infrared source with soft-glass fibers Supervisor: Prof. Camille-Sophie Brès EPFL, Switzerland <ul style="list-style-type: none"> ◇ Characterized soft glass fiber platforms with various materials and geometries ◇ Implemented novel Tm- or Ho-doped fiber laser cavities based on experimental needs ◇ Simulated real and designed fiber properties using finite element method software ◇ Achieved first continuous-wave (CW) parametric amplification in mid-infrared (MIR) ◇ First observation and study of fiber fuse in non-silica glass fibers ◇ Investigated linearly chirped all-normal-dispersion supercontinuum inside chalcogenide glass (ChG) fibers experimentally and numerically
Sept. 2013 - Feb. 2015	Thermal poling of chalcogenide fiber Supervisor: Prof. Martin Rochette McGill University, Canada <ul style="list-style-type: none"> ◇ Thoroughly studied state-of-art mid-infrared optical sources and applications ◇ Conducted thermal and optical poling on As₂S₃-As₂Se₃ ChG hybrid fiber and microwires ◇ Designed vacuum system and high voltage insulation (15kV max) for the experiment ◇ Collaborated with professors from different research areas during the project ◇ Intensive practices on ChG fiber handling, polishing and coupling ◇ Researched possible periodical poling approaches for improved conversion efficiency

TEACHING EXPERIENCE

Feb. 2018 - Present	EE 440 - Photonic Systems and Technology, EPFL
Feb. 2017 - Jun. 2017	EE 440 - Photonic Systems and Technology, EPFL
Feb. 2016 - Jun. 2016	EE 440 - Photonic Systems and Technology, EPFL
Sept. 2014 - Dec. 2014	ECSE 352 - Electromagnetic Waves, McGill University

JOURNAL PUBLICATIONS

- [1] Sida Xing, Davide Grassani, Svyatoslav Kharitonov, Adrien Billat, and Camille-Sophie Brès, “*Characterization and modeling of microstructured chalcogenide fibers for efficient mid-infrared wavelength conversion*,” *Opt. Express* **24**(9), 9741-9750 (2016).
- [2] Sida Xing, Davide Grassani, Svyatoslav Kharitonov, Laurent Brilland, Céline Caillaud, Johann Trolès, and Camille-Sophie Brès, “*Mid-infrared continuous-wave parametric amplification in chalcogenide microstructured fibers*,” *Optica* **4**(6), 643-648 (2017).
- [3] Sida Xing, Svyatoslav Kharitonov, Jianqi Hu, and Camille-Sophie Brès, “*Fiber fuse in Chalcogenide photonic crystal fiber*,” *Opt. Lett.*, **43**(7), 1443-1446 (2018).
- [4] Sida Xing, Svyatoslav Kharitonov, Jianqi Hu, and Camille-Sophie Brès, “*Linearly chirped mid-infrared supercontinuum from all-normal-dispersion chalcogenide photonic crystal fibers*,” *Opt. Express* **26**(15), 19627-19636 (2018)

CONFERENCE PROCEEDINGS

- [1] Sida Xing, Davide Grassani, Svyatoslav Kharitonov, Adrien Billat, and Camille-Sophie Brès, “*Small core Chalcogenide photonic crystal fiber for mid-infrared wavelength conversion: experiment and design*,” in Conference on Lasers and Electro-Optics (Optical Society of America, 2016), STh1O.6.
- [2] Sida Xing, Svyatoslav Kharitonov, Thibault North, Davide Grassani, and Camille-Sophie Brès, “*Generation of high-brightness spectrally flat supercontinuum in 1900-2450 nm range inside a small core thulium-doped fiber amplifier*,” in Lasers Congress (Optical Society of America, 2016), AM5A.8.
- [3] Sida Xing, Davide Grassani, Svyatoslav Kharitonov, and Camille-Sophie Brès, “*All-fibered chalcogenide based continuous-wave parametric amplification in the mid-infrared*,” in Conference on Lasers and Electro-Optics (Optical Society of America, 2017), STh1K-4.
- [4] Sida Xing, Davide Grassani, and Camille-Sophie Brès, “*Narrow linewidth polarizer-free 2.1 μ m Ho-doped fiber laser with 45dB polarization extinction ratio*,” in The European Conference on Lasers and Electro-Optics (2017).
- [5] Sida Xing, Svyatoslav Kharitonov, Jianqi Hu, Davide Grassani and Camille-Sophie Brès, “*Stable 2.1 μ m near 100% polarized Ho-doped all-fiber laser based on a polarizer-free cavity scheme*,” in The European Conference on Optical Communication (ECOC) 2017, M.2.B.3.
- [6] Camille-Sophie Brès, Sida Xing and Davide Grassani “*Low Power Amplified Mid IR Parametric Conversion in Tapered Chalcogenide Photonic Crystal Fibres*,” in The European Conference on Optical Communication (ECOC) 2017, M.2.B.1., **invited**
- [7] Sida Xing, Svyatoslav Kharitonov, Jianqi Hu, Davide Grassani and Camille-Sophie Brès, “*MIR supercontinuum in all-normal dispersion Chalcogenide photonic crystal fibers pumped with 2 μ m femtosecond laser*,” in Lasers Congress (Optical Society of America, 2017), ATu5A.3.
- [8] Camille-Sophie Brès and Sida Xing “*MIR Supercontinuum in All-normal Dispersion Chalcogenide Photonic Crystal Fibers*,” in Advanced Photonics Congress (Optical Society of America, 2018), SoTh3H.5, **invited**.
- [9] Camille-Sophie Brès and Sida Xing “*High performance Chalcogenide photonic crystal fibers pumped in the short-wave infrared*,” in Frontiers in Optics / Laser Science, (Optical Society of America, 2018), FW6B.1., **invited**.

- [10] Sida Xing, Svyatoslav Kharitonov, Jianqi Hu, and Camille-Sophie Brès, “*Study of fiber fuse induced damage in chalcogenide photonic crystal fibers*,” in Lasers Congress(Optical Society of America, 2018), ATh1A.4.

